UNIVERSITY OF CALIFORNIA

Santa Barbara

Microsphere Traction Force Microscopy

A dissertation submitted in partial satisfaction of the

requirements for the degree Doctor of Philosophy

in Mechanical Engineering

by

Buğra Kaytanlı

Committee in charge:

Professor Megan T. Valentine, Chair

Professor Omar Saleh

Professor Otger Campàs

Professor Matthew Begley

June 2017

The dissertation of Buğra Kaytanlı is approved.

_____
Omar Saleh

_____
Otger Campàs

_____
Matthew Begley

_____
Megan T. Valentine, Committee Chair

June 2017

Microsphere Traction Force Microscopy

VITA OF BUGRA KAYTANLI
June 2017

EDUCATION

Bachelor of Science in Physics and Mechanical Engineering, Boğazici University, Istanbul, June 2010

Doctor of Philosophy in Mechanical Engineering, University of California, Santa Barbara, June 2017 (expected)

PROFESSIONAL EMPLOYMENT

2010-17: Research and Teaching Assistant, Department of Mechanical Engineering, University of California, Santa Barbara

PUBLICATIONS

"Direct correlation between creep compliance and deformation in entangled and sparsely crosslinked microtubule networks," *Soft Matter,* 8, (2012), 1776-1784.

"Evolute-based Hough transform method for characterization of ellipsoids," *Journal of Microscopy,* 249(3), (2013), 159-164.

"Microsphere Traction Force Microscopy: Quantifying Inter-cellular Tractions," (*in prep. to be submitted*)

AWARDS

UCSB Crossroads Fellow: Materials, Mechanics and Medicine. 2014-2015

FIELDS OF STUDY

Major Field: Cellular Biophysics

Studies in Developing Microspherical Traction Force Microscopy Methods and Measuring Reconstituted Microtubule Network Mechanics with Professor Megan T. Valentine

ABSTRACT

Microsphere Traction Force Microscopy

by

Buğra Kaytanlı

This work is a culmination of our efforts in understanding cellular mechanics at the scale of single cells and small tissues. We developed methods to quantify cell-generated traction forces using cell-sized, synthetic, functionalized hydrogel microspheres. Cell-sized solid microspheres can provide information regarding cell-generated normal and shear forces while allowing natural cell-cell interactions and facilitating a convex cell-hydrogel interface. Therefore, they are a better mimic than the current methods for understanding the natural cell-cell interactions in a physiologically relevant geometry. In the analysis of the microsphere deformations, we use a boundary spectral method based on spherical harmonics decomposition of the traction field on the spherical gel surface. Using the techniques developed here, we measure the boundary traction profiles that mammalian cells exert on the synthetic microspherical hydrogel bodies. In this report, we briefly review the state of the art in cellular force quantification methods and discuss the contributions of our work to the field and its strengths as well as its limitations.

TABLE OF CONTENTS

LIST OF FIGURES

I. Introduction

Cells mechanically interact with their external microenvironment throughout their lifetime through the constant application of traction forces to their surroundings. These forces are coupled to the internal signaling events via adhesion sites on the cell surface and have been shown to regulate broad cellular processes including cell morphology, differentiation, behavior, and internal transcription levels [1][2][3]. As our understanding of the critical importance of the interplay between mechanics and biology grows, so does the need for quantitative measurement tools to study these cell-generated traction forces. A comprehensive review of the recent advances and current force measurement techniques is given in [4]. Briefly, most traction force microscopy (TFM) methods rely heavily on the use of flat substrates that promote cell adhesion to the surface [5]. Common substrates to measure cell-generated forces in the planar (2D) geometry include relatively soft hydrogels (~ 1kPa) that are seeded with embedded particles to track the internal material displacements or microfabricated micropillars that can be bent by cells that have adhered to the tips of the pillar array [6][7]. Even though these methods successfully capture the nano-Newton forces that are generated by the cells, the contact geometry of cellular attachments with planar hydrogel surfaces and flat micropillars is not representative of natural cell-cell or cell-ECM interactions. The first big leap in moving toward fully 3D force measurements came in 2010 when Legant *et.al*. encapsulated single cells in functionalized, elastic hydrogels and characterized the forces on the cell-hydrogel boundary by using finite element modeling (FEM) of the material displacements inside the hydrogel domain [8]. Using approaches from

solid mechanics, this technique allows measurement of the nominal values (with respect to load free conditions, i.e. zero kPa datum) of the full traction field along the cell periphery, including normal and shear force distributions. However, this method has been limited to use in single-cell systems where one cell is embedded in a synthetic hydrogel matrix and isolated from otherwise natural interactions with its neighboring cells. In 2014 Campàs e*t. al*. showed that injectable, functionalized oil droplets can be used to characterize the anisotropic deviations in normal tractions around a mean hydrostatic pressure on the droplet boundary while allowing an ensemble of surrounding cells to maintain natural cell-cell contacts while interacting with the oil droplets [9]. This is technique is quite versatile in that it allows delivery of micro-droplets of a wide range of sizes into the intercellular spaces via microinjection. Also, since the functionalized micro-droplets return to their spherical state upon removal of cellular loading, they don't require information about their "rest" configuration; therefore, enzymatic treatment of the cellular/tissue system is not required to measure cellular forces. However, since liquid droplets are effectively incompressible on the scale of tissue-generated stresses, they cannot capture the nominal values of the normal boundary traction forces. The droplet's resistance to deformation arises from the surface tension on the emulsion boundary due to the dissimilarity of the internal oil phase and surrounding aqueous phase (containing cells and media); therefore, shear information is not captured by the deformations of the interface. More recently, a similar approach that uses free, deformable bodies to measure stresses in cellular systems has been proposed by Dolega et. al. where the authors used compressible hydrogel microspheres to measure the

transmission of hydrostatic stresses inside cell-aggregates in response to externally applied osmotic pressures by quantifying the volumetric changes in the elastic microspheres [10].

These prior techniques have provided useful information on how forces are generated in single cells or small groups of cells and how the stresses are transmitted at cellular length scales. However, a method that can quantify the nominal values of normal and shear tractions while maintaining intra-cellular interactions is still lacking. Here we present the development of a force measurement method that uses cell-sized hydrogel microspheres (with diameters of 5-50 μm) as force sensors, thereby providing a more natural interaction geometry where cells can apply both shear and normal tractions. In practice, we use poly(ethylene-glycol) diacrylate (PEGDA)-based hydrogel microspheres that are diffusely labeled with rhodamine-acrylate and are functionalized with RGD peptides that promote cell attachment. In the sections below we show that we have developed methods to quantify the *nominal values* of the normal component of the total traction forces that cells apply on the microspheres by using surface tracking of the diffusely labeled microspheres, as illustrated in Figure 1. In Chapter VI, we further discuss the experimental and computational methods to determine shear component of the cellular tractions by using fluorescent particles or additionally generated internal surfaces as reporters of internal material deformations and present our current progress and preliminary work on material tracer-based Microspherical Traction Force Microscopy methods.

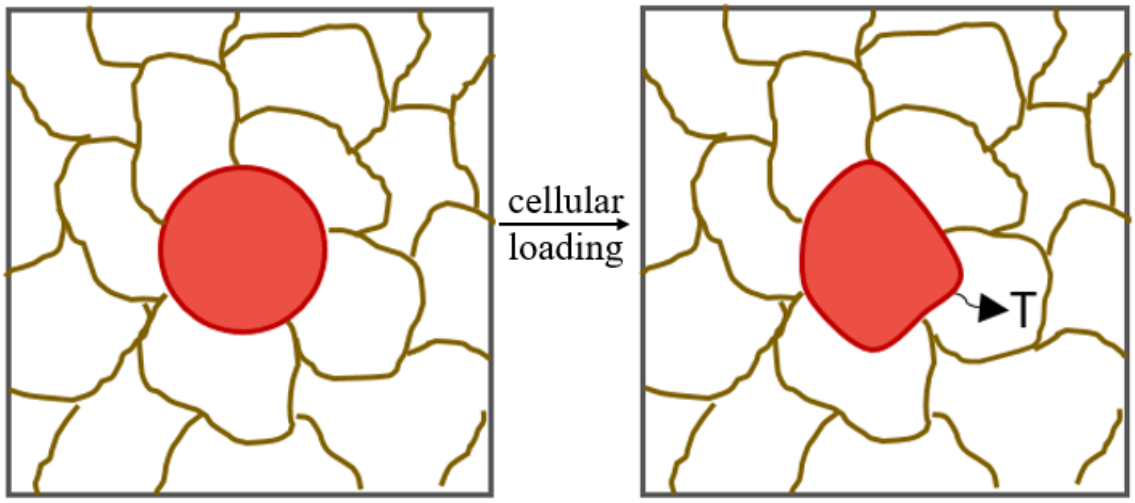

Figure 1. Schematic description of Microsphere Traction Force Microscopy (MTFM) geometry. The labeled and functionalized PEGDA microsphere is shown in red and cell boundaries are depicted in golden brown. The initially undeformed spherical hydrogels deform and change shape upon being subjected to cellular traction forces, *T*.

II. Mathematical Methods for MTFM

An elastic body under boundary loading undergoes deformations throughout the bulk of the material. Here, our aim is to be able to uniquely define the force field $\vec{F}(\varphi, \theta)$ that is defined on the surface of the spherical body, that generates a given deformation field, $\vec{u}(r, \varphi, \theta)$, inside the bulk of the body, where and r is the radial coordinate, φ and θ are the polar and azimuthal angles, respectively. In particular, we aim to solve for the boundary loading profile $\vec{F}$ by using the material deformations, $\vec{u}$, that are tracked by discrete fluorescent markers distributed in the microsphere. In the context of cellular traction force microscopy, solving for the boundary loading profile enables determining the traction profile that the cells apply on the spherical body to generate the observed deformations inside the hydrogel. In the following sections, we discuss the mathematical methods we employed to solve the problem mentioned here.

1. Spherical Harmonics Expansion of Force Field in 3D

The traction force field $\vec{T}(\varphi, \theta)$ that is defined on the surface of the spherical body is a 3-vector field and r is the radius, with independent components in all three directions, denoted by $\vec{T}_x$, $\vec{T}_y$ and $\vec{T}_z$.

$$\vec{T}(\varphi, \theta) = \vec{T}_x(\varphi, \theta) + \vec{T}_y(\varphi, \theta) + \vec{T}_z(\varphi, \theta) \quad (1)$$

Each component of the force field can be rewritten as a scalar and a unit vector field, $T_i(\varphi, \theta)$ and $\vec{e}_i(\varphi, \theta)$ respectively, such that:

$$\vec{T}(\varphi,\theta) = T_x(\varphi,\theta)\vec{e}_x + T_y(\varphi,\theta)\vec{e}_y + T_z(\varphi,\theta)\vec{e}_z \tag{2}$$

Therefore, each component of the force field is represented by:

$$\vec{T}_i(\varphi,\theta) = T_i(\varphi,\theta)\ \vec{e}_i(\varphi,\theta) \tag{3}$$

The three scalar fields T_x, T_y and T_z are sufficient to fully describe an arbitrary field $\vec{T}$. Furthermore, each scalar field T_i can be expanded as follows:

$$\vec{T}_i = T_i\vec{e}_i = \left(\sum_{n,m} a_{nm}^i Y_n^m\right)\vec{e}_i \tag{4}$$

where Y_n^m denotes the spherical harmonic of order m and degree n.

$$Y_n^m(\varphi,\theta) = \begin{cases} \sqrt{\dfrac{2n+1}{2\pi}\dfrac{(n-m)!}{(n+m)!}}P_n^m(\cos\varphi)\cos(m\theta), & m > 0 \\ \sqrt{\dfrac{2n+1}{4\pi}\dfrac{(n-m)!}{(n+m)!}}P_n^m(\cos\varphi), & m = 0 \\ \sqrt{\dfrac{2n+1}{2\pi}\dfrac{(n-|m|)!}{(n+|m|)!}}P_n^{|m|}(\cos\varphi)\sin(|m|\theta), & m < 0 \end{cases} \tag{5}$$

where P_n^m are the associated un-normalized Legendre polynomials.

Spherical harmonics, for which a graphical representation is given in Figure 2, provide an orthonormal basis for expressing arbitrary functions on a spherical surface, which is analogous to the use of 2D Fourier Series in a planar geometry. Moreover, with the addition of six constraints to account for the six degrees of freedom in three-dimensions, spherical harmonics naturally provide a self-balanced force field on the free spherical body, since the individual harmonics greater than degree zero have zero mean.

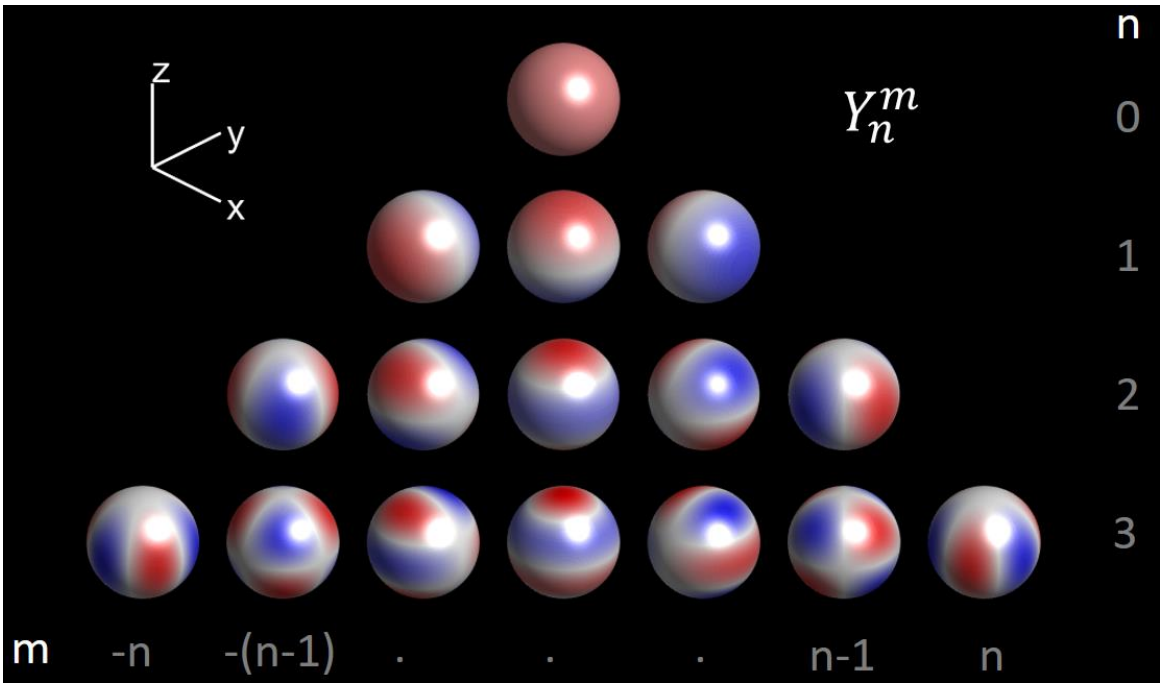

Figure 2. Scalar force amplitudes expressed in terms of spherical harmonics, Y_n^m. Red: positive, blue: negative scalars, normalized to the largest number displayed.

The laws of elasticity consider only deformations with respect to the center of mass of the free body. Therefore, rigid body translations and rotations, which are determined by the $n = 0$ and $n = 1$ terms respectively, must be specifically addressed. As shown in Figure 3, when evaluated in the *x*, *y* and *z* directions, $\vec{T}_i = Y_0^0 \vec{e}_i$ yield a positive net force (along the *x*-*y*-*z* axes) that would cause rigid body translations of the free body rather than deformations around the center of mass. Thus, these are excluded from the series expansion. The rigid body rotations are prevented by imposing constraints on the coefficients associated with the first-degree harmonics, Y_1^m, as illustrated in Figure 4.

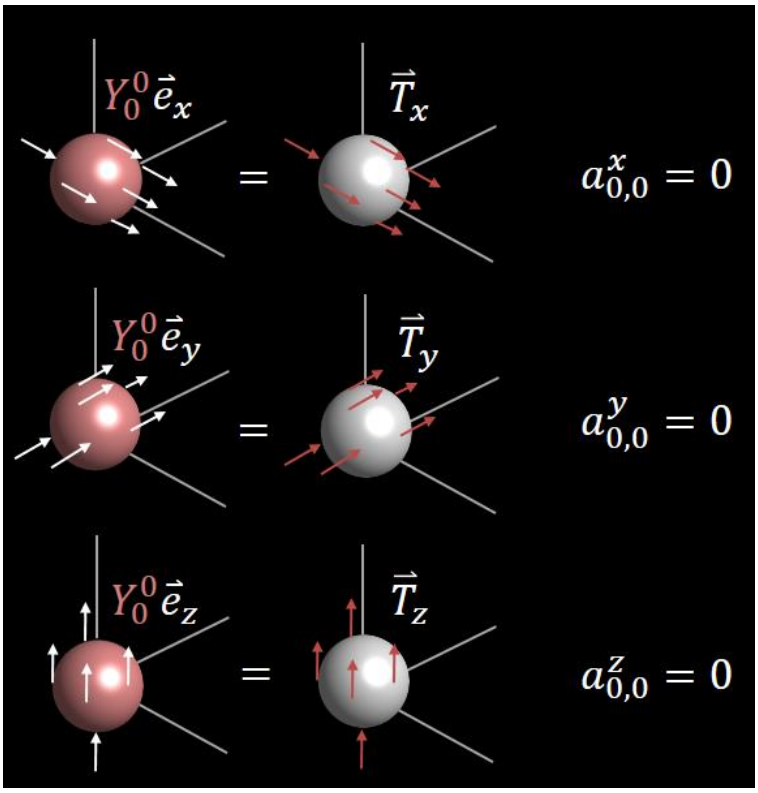

Figure 3. Zeroth degree harmonics, Y_0^0, are associated with rigid body translations in all three directions. These are excluded from the series expansion by setting the associated coefficients to zero, as described.

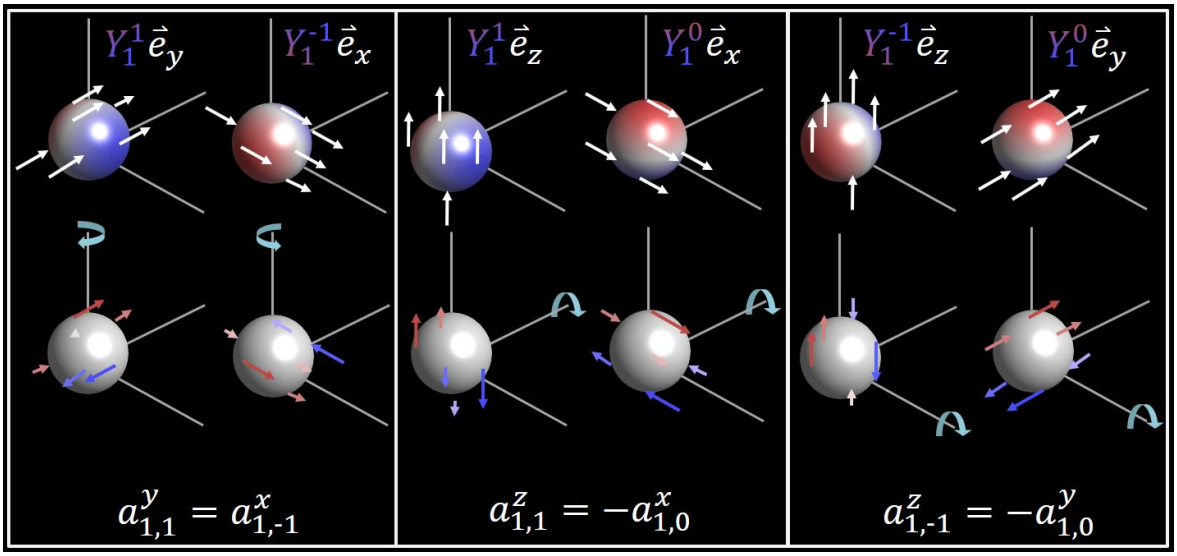

Figure 4. Rigid body rotations are prevented by imposing constraints on the coefficients of first-degree harmonics, as described.

Since the functions T_i are represented as a truncated series of spherical harmonics, the maximum degree of the expansion, n_{max}, sets a bound for the spatial resolution of the reconstructed force field. Also, we assume that the cells are in full contact with the outside boundary of the microspheres and the cell-generated tractions are continuously differentiable with no jump-discontinuities in the force field; therefore, the possible issue of Gibbs phenomenon for spherical harmonics reconstructions is not considered here.

2. Displacement Field Inside Spherical Body

For a free sphere loaded with surface spherical harmonics, the associated deformations inside the bulk of the material are studied in [11] and more explicitly presented in [12]. From [11-12], the solution to the displacement field is:

(6)

$$
\begin{aligned}
2G\vec{u} = {} & \vec{\Pi}_1 - \frac{\nu}{1+\nu}\vec{R}\nabla\cdot\vec{\Pi}_1 \\
& + \sum_{n=2}^{\infty}\left\{\frac{1}{n}\overrightarrow{\Pi_n} + \frac{\vec{R}\times\nabla\times\vec{\Pi}_n}{n(n-1)} + \frac{[(1-4\nu)n-2(1-\nu)]\vec{R}\nabla\cdot\vec{\Pi}_n}{n[n^2-(1-2\nu)n+1-\nu]}\right. \\
& + \frac{(2\nu n+1-\nu)R^2\nabla\nabla\cdot\vec{\Pi}_n}{n(n-1)[n^2-(1-2\nu)n+1-\nu]} \\
& \left. + \frac{(R^2-R_0^2)\nabla\nabla\cdot\vec{\Pi}_n}{n(n-1)[n^2-(1-2\nu)n+1-\nu]}\right\}
\end{aligned}
$$

where,

$$\vec{\Pi}_n = \left(\frac{R}{R_0}\right)^n R_0\vec{Y}_n \tag{7}$$

and,

$$\vec{Y}_n = \sum_{i=x,y,z} T_i\vec{e}_i = \sum_m (a_{nm}^x Y_n^m\,\vec{e}_x + a_{nm}^y Y_n^m\vec{e}_y + a_{nm}^z Y_n^m\vec{e}_z) \tag{8}$$

Where $\vec{R}$ is the position vector measured from the center of the sphere, R is the magnitude of $\vec{R}$, R_0 is the radius of the sphere, G is the shear modulus, ν is the Poisson's ratio and $\vec{\Pi}$ is the solid spherical harmonic as defined in (7).

The solution to the displacement field can be implemented as the closed-form solution given in [12], otherwise equation (6) can be numerically computed at each material point using Mathematica [13]. Here, we used the closed-form solution to the elasticity problem as given in [12]. By using the analytical solution, we compute the associated deformations for each mode of loading and construct a basis for deformations in terms of the spherical harmonics force basis. Figure 5 illustrates the basis construction process.

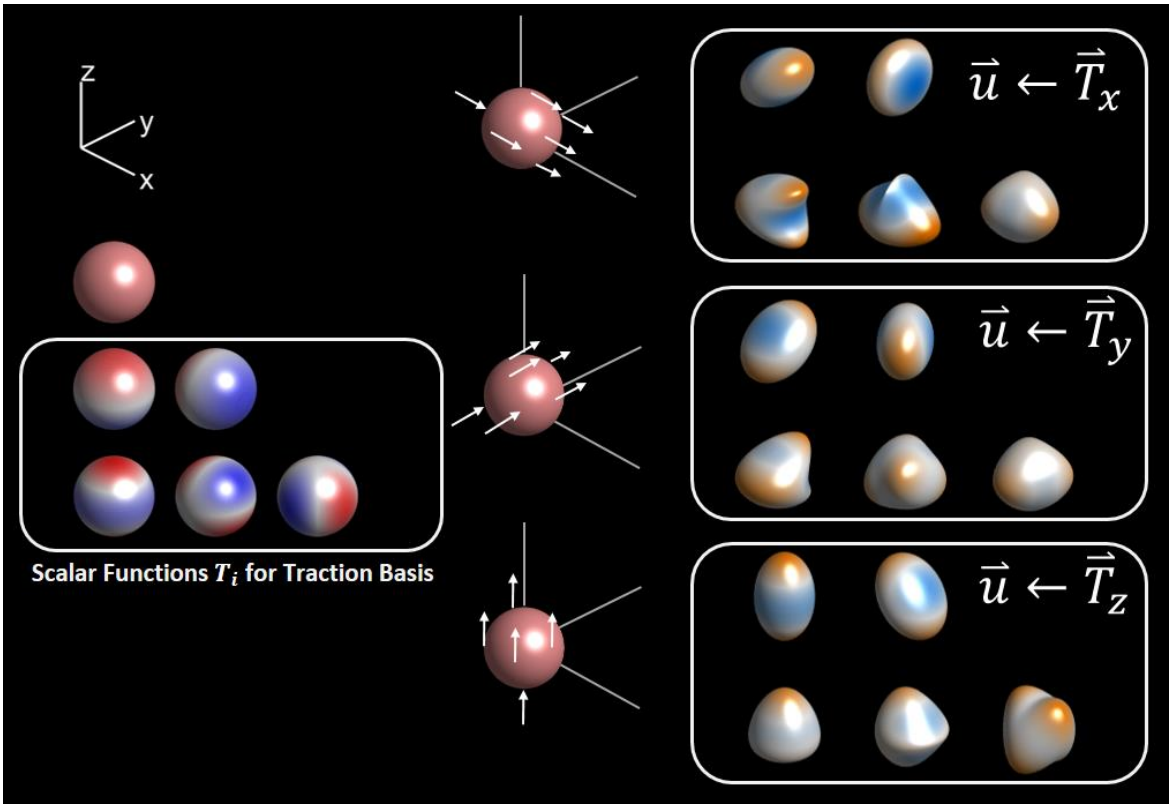

Figure 5. Force basis is evaluated in *x*, *y* and *z* and the displacement basis is constructed at select material points. For simplicity, the left-hand sides ($m < 0$) of the force and deformation bases are omitted from the graphical representation.

Once the deformation basis is constructed, we can determine how much each deformation mode contributes to the measured arbitrary deformation field inside the body. More precisely, we express the deformation field as a linear combination of deformation modes, $\vec{u}^i_{nm}$, such that:

$$\vec{u}_{measured} = \sum_{i,n,m} a^i_{nm} \vec{u}^i_{nm} \tag{9}$$

Graphically, the statement in (9) is equivalent to the deformations shown in Figure 6 below:

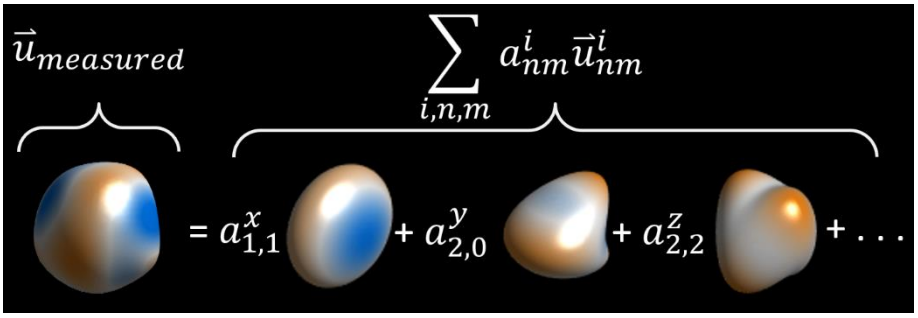

Figure 6. Arbitrary deformations are expressed as a linear combination of the modal deformations. Blue = inward deformation from spherical (effective compression). Orange = outward deformation from spherical (effective stretch).

To carry out numerical computations with the displacement fields given in [12], the spherical surface is discretized and meshed as shown in Figure 7.

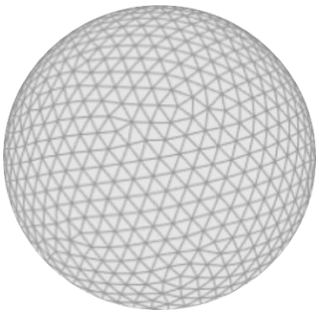

Figure 7. Spherical surface mesh with 1000 nodes.

Once the material points are discretized, the displacement vector associated with each node is computed and the concatenated displacement vector u_{nm}^{i} is defined as:

$$u_{nm}^{i} = \begin{bmatrix} u_{nm}^{i}(x) \\ u_{nm}^{i}(y) \\ u_{nm}^{i}(z) \end{bmatrix} \tag{10}$$

where $u_{nm}^{i}(x), u_{nm}^{i}(y)$ and $u_{nm}^{i}(z)$ are N-by-1 coumn vectors denoting the displacements of N nodes in x, y and z, respectively, and u_{nm} is the concatenated $3N$-by-1 vector of x-y-z deformations under the spherical harmonic loading $Y_n^m \vec{e}_i$. Figure 8 illustrates the material deformations inside the discretized body as a response to $Y_1^1 \vec{e}_x$.

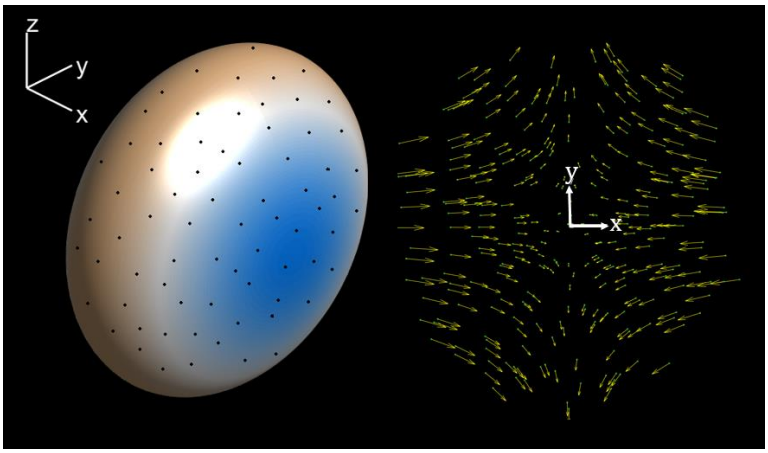

Figure 8. Surface rendering and internal material displacements in the deformed body under $Y_1^1 \vec{e}_x$ loading.

If we evaluate all deformations u_{nm}^i, (9) now can be written as a linear system such that:

$$u_{me} = \sum_{i,n,m} a_{nm}^i u_{nm}^i \tag{11}$$

$$u_{me} = Ua \tag{12}$$

where $u_{me}$is the measured pointwise displacements and U is the displacement basis matrix given as:

$$U = \begin{bmatrix} u_{1,-1}^x & \cdots & u_{1,-1}^y & \cdots & u_{1,-1}^z & \cdots \end{bmatrix} \tag{13}$$

Figure 9 illustrates the displacement basis matrix for 100 distributed nodes on the gel boundary (300 displacements total) and 45 loading modes (15 per dimension, corresponding to an expansion up to n_{max}=3); therefore, U is a 300-by-45 matrix.

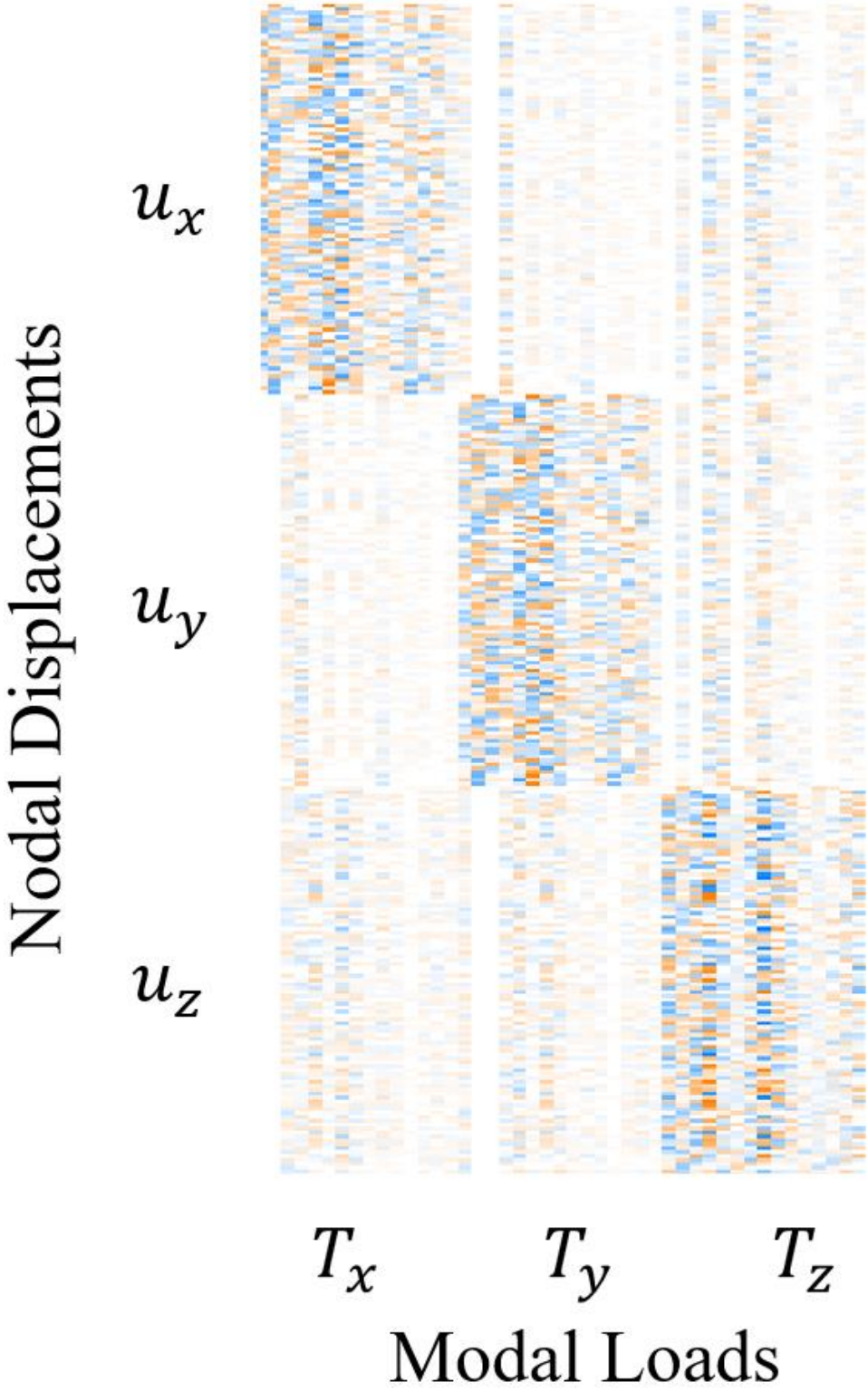
Nodal Displacements
u_x
u_y
u_z
T_x
T_y
T_z
Modal Loads

Figure 9. Displacement basis, *U*, evaluated on the sphere surface. The colors represent the direction and of loading: Blue = inward deformation from spherical (effective compression); Orange = outward deformation from spherical (effective stretch); while white indicates no displacement. Darker shades of the colors correspond to larger magnitude displacements. *U* is close to block diagonal, in which the largest deformations occur along the direction of loading and the displacements on orthogonal dimiensions are due to material couplings through the Poisson's ratio of the material, taken as 0.45 here.

Clearly the deformations are maximal at the boundary and decay to zero at the center of mass. The radial decay rate of the deformations varies with $\sim r^n$, with *n* denoting the degree of the harmonic loading. This means that the internal points provide more information about the lower degree harmonics whereas the surface equally weights all degrees of loading. This property of the deformation field is extremely useful, and will be discussed in chapter IV.

Solving the Linear System of Equations

Given that the deformation basis matrix, U, is non-invertible, one could pose the problem as a minimization and solve the linear system of equations by:

$$\min\{||Ua - u_{me}||_2^2\} \tag{14}$$

However, the measured displacement vector, u_{me}, contains experimental measurement noise from imaging and bead tracking. Therefore, instead of (14), we employ the 0^{th} order Tikhonov regularization, which ensures that the computed solution, a, will not be dominated by the inherent measurement noise, and solve for the following optimization problem:

$$\min\{\left|\left|Ua - u_{me}\right|\right|_2^2 + \lambda\left|\left|a\right|\right|_2^2\} \quad (15)$$

The problem is solved by singular value decomposition and the *L*-curve criterion [14] for choosing the optimum value for the regularization parameter, λ, using the MATLAB routines by P.C. Hansen [15].

III. Computational Methods for Surface-based MTFM

In this work, we investigated two different approaches on performing MTFM; surface tracking- and particle tracking-based methods. In this chapter, we present the surface tracking-based MTFM methods and discuss their advantages and limitations in the context of experimental measurements in cellular systems. Possible improvements on the surface methods and our preliminary work on particle tracking-based methods are presented in the Chapter VI.

A. Surface Reconstruction

Fluorescent confocal microscopy image stacks are collected using a Leica SP8 confocal microscope equipped with a 40X water-immersion objective (N.A.=1.1). Subsequently, the image stacks are deconvolved using Huygens software to increase the definition and the signal to noise ratio of the fluorescence signal in the images. Following deconvolution, we use a commercial software, Imaris, for 3D rendering of the microsphere surfaces that are labeled with acrylated rhodamine-B dye which conjugates to the hydrogel backbone, as shown in Figure 10. During the reconstruction, the image stacks are locally thresholded using manual tuning of the parameters. Upon surface rendering in Imaris, the surface meshes are downsampled and smoothed using Taubin smoothing [16] to prevent shrinkage, using MeshLab. Although this method uses commercially available software and is thus relatively user friendly, it does require manual tuning of the local thresholding parameters, which may introduce variations in reconstruction of the gel boundary surface. In order to minimize

these effects, for a given data set on the same microspherical body, we normalize the pixel intensity distributions of the images and use the same settings for all time points.

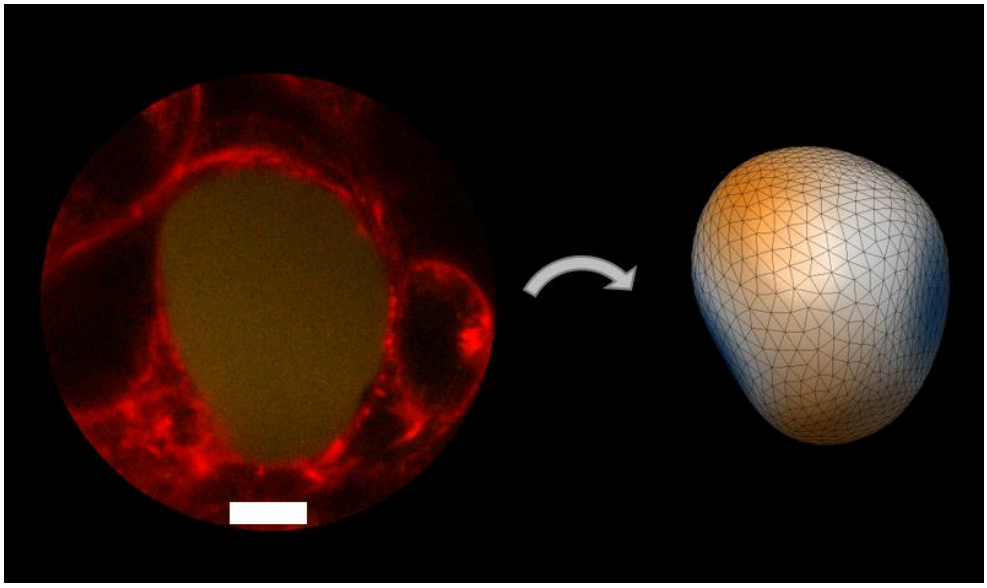

Figure 10. A representative image of a deformed hydrogel microsphere under cellular loading. The image on the left is a confocal microscope *x-y* scan of the deformed body (yellow) that has established surface attachments with the surrounding 3T3 mouse fibroblasts which are labeled with SiR actin (red). 3D rendering of the deformed hydrgel surface is shown on the right. The colors on the rendered surface indicate the total displacements on the boundary, orange = outward from the undeformed spherical surface normal, blue = inward displacements to the spherical hydrogel boundary. Scale bar is 5μm.

In the time-lapse experiments, image stacks of the volume of interest are recorded over time while the free microsphere hydrogel body experiences rigid body motions as well as deformations around its center of mass. Since the analysis of elastic loading depends on the

deformations only, it is crucial to precisely and accurately locate the microsphere center of mass at each time point. This can be achieved using the surface rendering of the body under the assumption that the density of the gel remains constant despite the observed deformations. For our PEGDA-based hydrogels, the Poisson's ratio is ~0.45 (see the materials characterization section in Chapter IV for full details), and this assumption of constant density across the body is reasonable. Once the rendered surface is constructed, it can be used to calculate the body's mass center.

B. Surface Tracking for MTFM

1. Shortest Distance Mapping for Estimating the Displacement Field

Surface shape-based formulation of the displacement tracking has experimental advantages over point tracking methods in terms of robustness to intercellular scattering, depth dependent signal to noise degradation and aniostropically distorted point spread functions observed inside thick (>100μm) tissues. This formulation is very robust to tissue dependent imaging artefacts since the geometrical information is collected from a two-dimensional surface rather than point emitters, as in the case of particle-tracking MTFM methods. However, due to the experimental challenges in preparing mechanically controlled and well-characterized, multi-colored, multi-surface microspheres, and partly due to the computational challenges that require use of FEM methods, we have implemented an elastic shape matching algorithm for single-colored solid microspheres (Figure 11), using our spherical harmonics based approach.

In the case of single-colored microspheres, if an entirely *boundary-based* shape matching is employed, because of the homogenous labeling of the deforming body on the interior, the information about the in-plane deformations on the deformed body are lost; therefore, the minimization problem that is posed in equation (15) as:

$$\mathbf{min}\{\left|\left|\boldsymbol{Ua}-\boldsymbol{u_{me}}\right|\right|_{\mathbf{2}}^{\mathbf{2}}+\boldsymbol{\lambda}\left|\left|\boldsymbol{a}\right|\right|_{\mathbf{2}}^{\mathbf{2}}\} \tag{16}$$

where u_m is the measured *pointwise displacements* inside the body, transforms to the more general problem:

$$\mathbf{min}\{\left|\left|\boldsymbol{Ua}-\boldsymbol{u}^{*}\right|\right|_{\mathbf{2}}^{\mathbf{2}}+\boldsymbol{\lambda}\left|\left|\boldsymbol{a}\right|\right|_{\mathbf{2}}^{\mathbf{2}}\mid(\boldsymbol{X}+\boldsymbol{u}^{*})\in\boldsymbol{S}\} \tag{17}$$

where X is the spatial coordinates of the material points on the undeformed boundary, $u^*$is the displacements associated with the correspoding material points, and S is the surface that the deformed body coordinates $(X + u^*)$ exist on, which is given by the boundary surface of the deformed body. Therefore, rather than having a unique deformation field input, the problem posed in (17) relaxes the condition of meeting a point-wise defined specific displacement field, u_{me}, and replaces it by a weaker constraint which asserts that the displacement field, u^*, lies in a subspace of all admissible displacement fields which satisfies the condition $(X + u^*) \in S$, where S is the boundary surface of the deformed body.

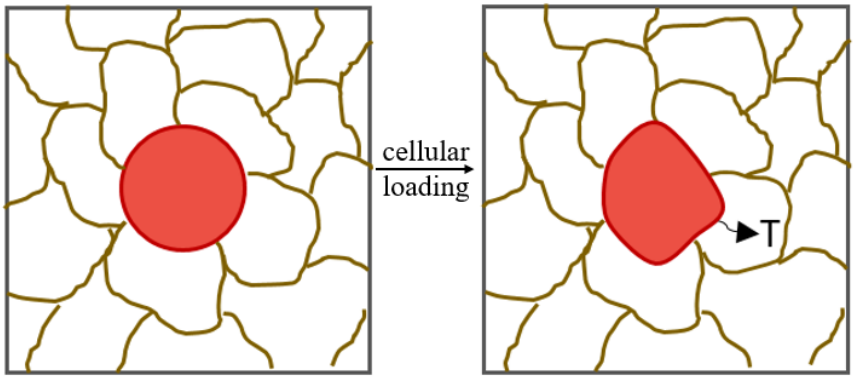

Figure 11. Illustration of single-colored hydrogel and cell geometry. Single-colored microsphere surface is used in predicting the minimal loading that generates the observed deformation.

The lack of a measured, unique displacement field, therefore, calls for *predicting* the displacement field at each iteration in the minimization process. In order to achieve this, we implemented an iterative shortest distance mapping algorithm. As illustrated in Figure 12, at each iteration we first predict the final destination of the points, X, that are located on the undeformed boundary by using a shortest distance mapping from those points to the destination surface, S, (i.e. the surface of the deformed body). Upon mapping, we define the displacement field, u_i, as the difference between the destination points and the source points for the given iteration number, i. Although for early iterations being physically non-realistic, u_i provides an estimate of the displacement field at each iteration and we solve for (17) where $u^*$is set equal to u_i such that:

$$\mathbf{min}\{\left|\left|\boldsymbol{Ua}-\boldsymbol{u_i}\right|\right|_{\mathbf{2}}^{\mathbf{2}}+\boldsymbol{\lambda}\left|\left|\boldsymbol{a_i}\right|\right|_{\mathbf{2}}^{\mathbf{2}} \mid (\boldsymbol{X}+\boldsymbol{u_i})\in \boldsymbol{S}\} \tag{18}$$

where the condition $(X + u_i) \in S$ is naturally satisfied.

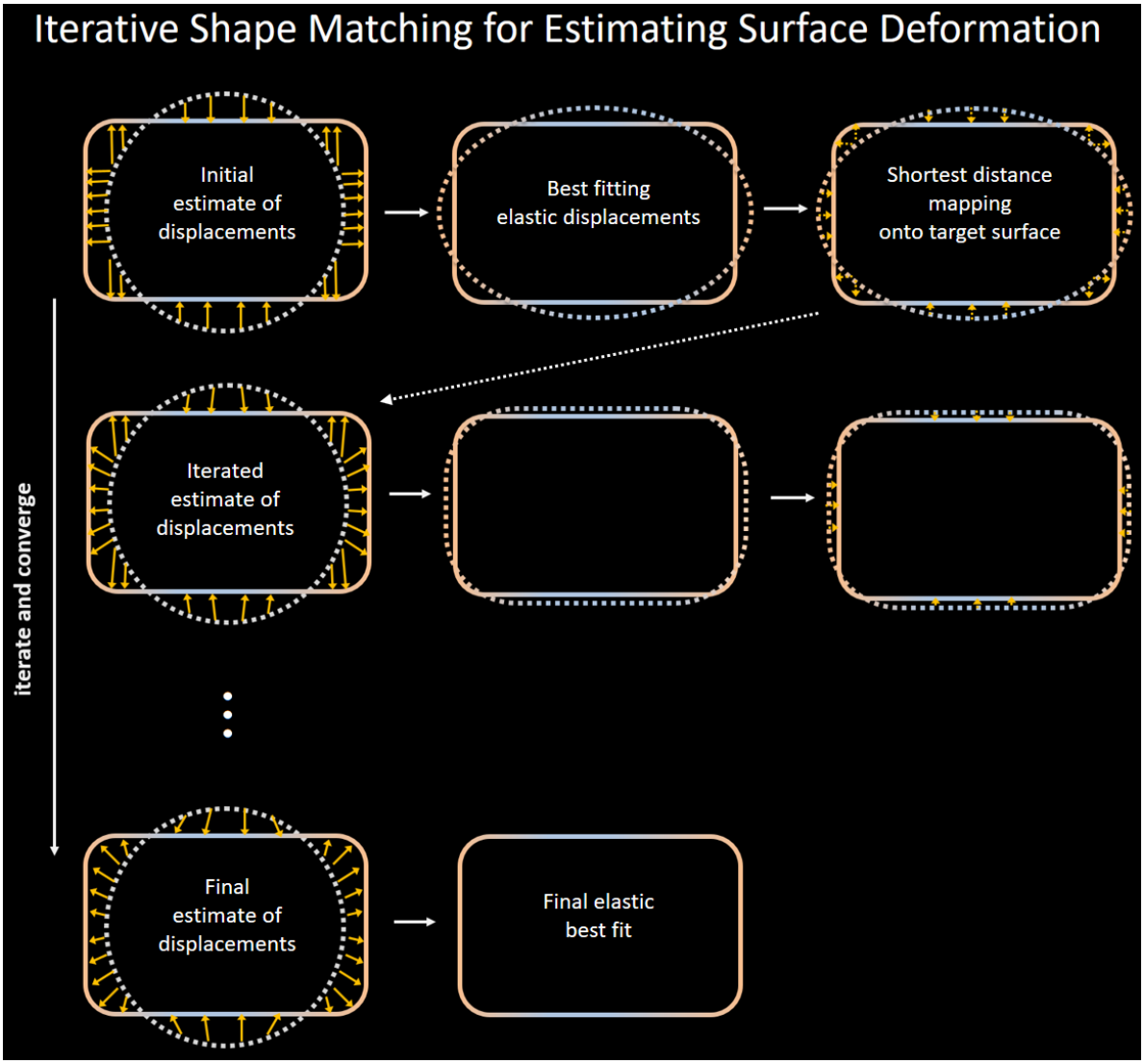

Figure 12. Summary of iterative shape matching algorithm. At each iteration, the source points are projected onto the destination surface by shortest distance mapping. At each iteration, the minimization problem posed in (18) is solved by providing the computed displacements as the observed deformation field. The best fitting elastic displacement field, Ua_i, is then used as source points for shortest distance mapping onto the target surface. At

the final iteration, the shortest-distance estimate of the displacement field converges to a kinematically admissible field and the solution, a_i, converges to the solution to the corresponding equation.

The minimization problem posed in (18) is solved at every iteration by providing the resulting displacements, u_i, as the observed deformation field. For a given, u_i, the computed elastic displacement field, Ua_i, is used as source points which are mapped onto the target surface. At the final iteration, the shortest-distance estimate of the displacement field converges to a kinematically admissible field and the solution, a_i, converges to the solution to the corresponding equation with the given kinematically admissible displacement field provided as its input.

2. Local Interpolation of Target Surface Mesh

Shortest distance mapping of the points on the microsphere onto the deformed boundary requires defining a closed surface which represents the rendered surface. It is rather intuitive to define this surface as the closed polygon, *i.e.* the rendered triangular surface mesh, of the deformed boundary. However, computing the shortest distance from a point to a closed polygonal surface is computationally expensive as the closest point could fall on a vertex, edge or a face – which necessitates going over all these elements. Another downside of working with polygonal surfaces is that, the error in the distances of the mapped points is linearly proportional to the element size.

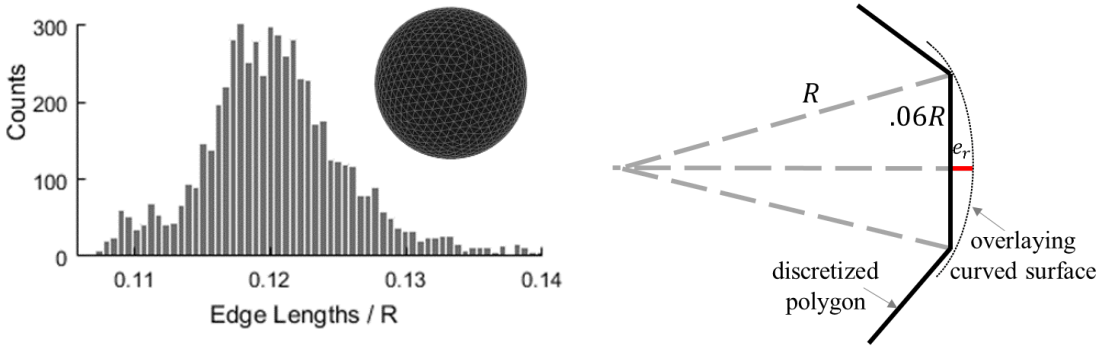

Figure 13. Left: Distribution of edge lengths. Mean = ~12% of the microsphere radius, for the 1000-node surface mesh shown in the inset. Right: Geometric estimation of the error associated with the polygonal discretization of the overlaying curved surface for a 1000-node surface mesh on the spherical body.

For a typical mesh size of 1000 vertices, the mean edge length is ~12% of the microsphere radius. Therefore, by observing the right panel in Figure 13, a rough estimate of the error that is associated with the polygonal discretization is calculated as:

$$\frac{\boldsymbol{e_r}}{\boldsymbol{R}} \approx \left(\mathbf{1} - \sqrt{\mathbf{1} - \mathbf{.06^2}}\right) \approx \mathbf{2}\% \tag{19}$$

Assuming the observed displacements are between10-20%, the discretization due to meshing would create 10-20% error in the displacements measured on the surface.

Therefore, to achieve computational efficiency and accuracy in mapping the undeformed surface points onto the deformed surface, as illustrated in Figure 14, we approximate the overlaying curve with local spheres that are fit to the first neighborhood of each vertex in the least squares sense using MATLAB routines developed by A. Jenning and explained in detail in [17]. In addition, since the spheres which have 4 free parameters are locally fit to

~7 points, they act as local low-pass filters and help reduce measurement and reconstruction errors by smoothing the geometry locally.

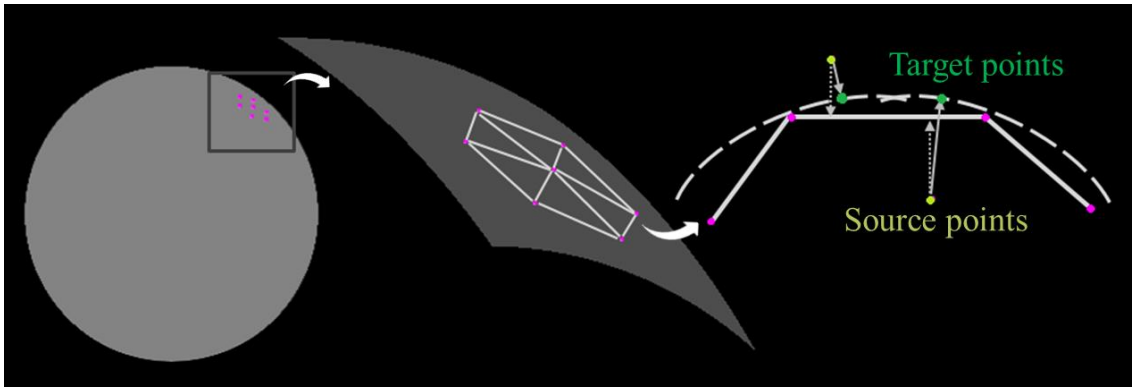

Figure 14. Local sphere fitting to the first order neighborhood of each vertex. The source points land on the spheres that are locally fit to the polygonal vertices, increasing the efficiency and the acuracy of the shortest distance mapping.

Upon approximating the overlaying curve with local spheres, the information (center and radius) for each sphere associated with a given vertex is stored in the memory. Therefore, during the iterative search for the shortest distance, each source point is matched to the closest polygonal vertex (shown in pink) using standard MATLAB routines. Once the closest-vertex match is made, the shortest distance from the source point to the target sphere is calculated algebraically. This approach increases the temporal efficiency of the search&map method by two orders and the numerical accuracy by an order of magnitude when compared to basic polygonal search&map algorithms; thus, enables efficient iterative computation of the surface displacements in reasonable time.

C. Traction Field Reconstruction Formulation[1]

Upon iteratively solving for the convergent values of a kinematically admissible displacement field u and the corresponding linear contribution vector a, from the displacement formulation as discussed above, we use the same modal coefficients to reconstruct the traction field applied on the undeformed body as illustrated in Figure 15, using:

$$\vec{T}_i = T_i \vec{e}_i = \sum_{n,m} a_{nm}^i Y_n^m \, \vec{e}_i \tag{20}$$

where the tractions, $\vec{T}_i$, in all three directions are expressed in terms of a unit vector field, $\vec{e}_i$, and orthonormal spherical harmonics Y_n^m, as scalar fields that act on the unit vector field to change its magnitue at every point *o* the spherical body. Each mode (*n,m*) in the spherical harmonic expansion contributes to the final deformation field in the *i*'th direction by a amount, a_{nm}^i, that is determined from solving the optimization problem in (17). As illustrated in Figure 15. Upon determining all a_{nm}^i from the deformations, a linear superposition of the correspoding loading modes is used to construct the total force field that is applied on the undeformed body to yield the observed material deformations.

[1] I would like to thank Prof. Bob McMeeking for all his guidance and help with the methods explained below.

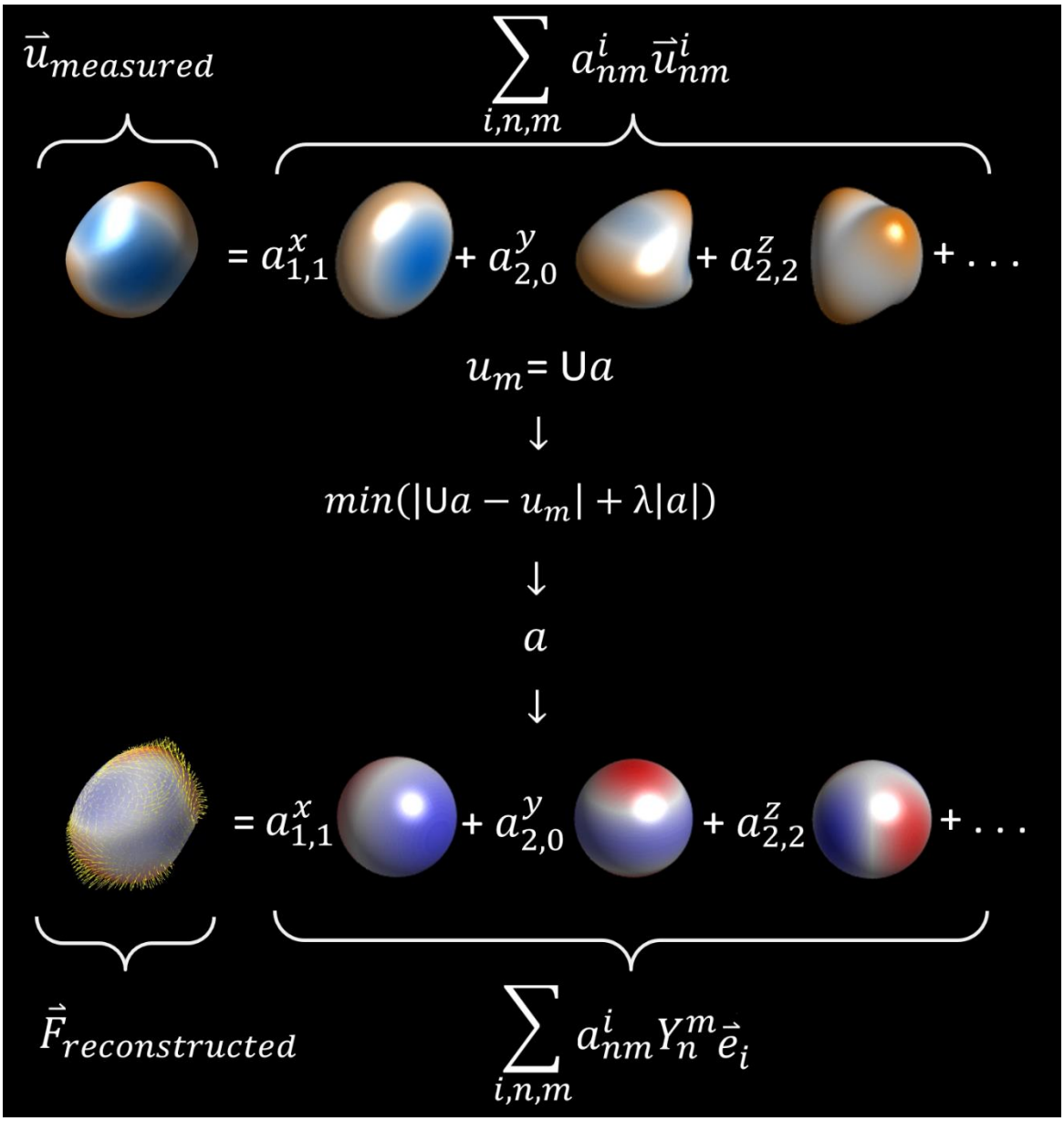

Figure 15. Force field reconstruction by summing the calculated individual contributions from the modal deformations. The modal contribution vector, a, is calculated from the displacements and used in reconstructing the force field from corresponding modal loads.

We note that it is crucially important that the calculated traction field as a result of (18) gives the loading profile, T^0, that is applied on the undeformed body. Fortunately, the use of spherical harmonics expansion to express traction distribution on the undeformed spherical body gives a self-balanced loading field. However, under any given loading, the elastic body deforms and changes its geometry, thus the area that the traction is acting on. Therefore, the tractions that are applied on the undeformed body, T^0, need to be scaled with the local change in the area in order to guarantee the force balance on the *deformed* boundary. Figure 16 illustrates this concept on an area element, dA, that deforms under the action of T^0.The force balance is established when:

$$T^0 dA = T' da \tag{21}$$

where dA and da are the areas before and after deformation, respectively.

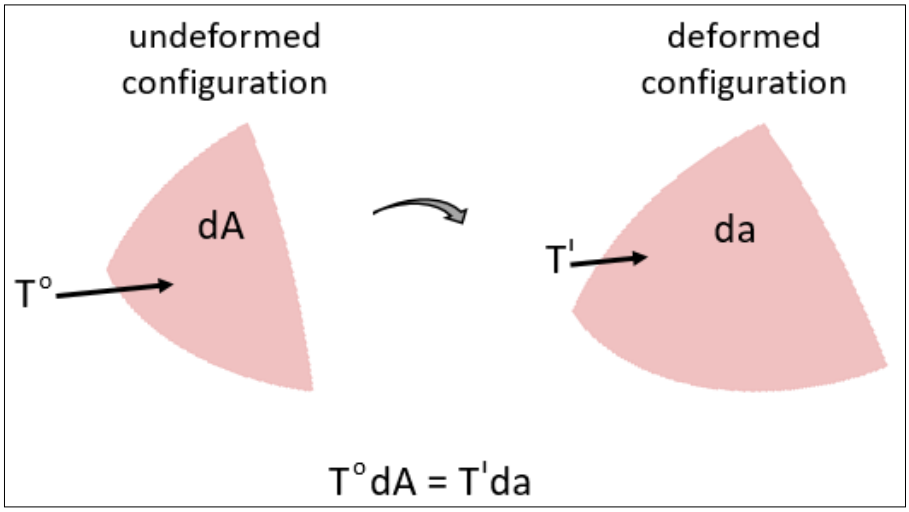

Figure 16. Schematic showing how the tractions calculated on the deformed body must be scaled by the local area change (that is a result of the deformation) in order to establish force balance in the deformed configuration.

Rewriting (19), we obtain:

$$T' = \frac{dA}{da} T^0 \tag{22}$$

Therefore, calculating the traction field on the deformed geometry, T' , calls for calculating the quantity *dA/da*, which we accomplish using the well-known Nanson's Formula:

$$da\,\vec{n} = J(F^T)^{-1} dA\,\vec{N} \tag{23}$$

Rearranging (21) yields:

$$\frac{dA}{da} = \frac{1}{J\,\vec{n}^T\,(F^T)^{-1}\vec{N}} = \frac{\vec{N}^T F^T \vec{n}}{J} \tag{24}$$

where, F is the deformation gradient and J is the determinant of F, and $\vec{N}$ and $\vec{n}$ are the surface normals of the undeformed and the deformed body, respectively.

Since we have the closed-form expression of deformation field everywhere on the body, we can calculate the deformation gradient F by numerically differentiating the displacement field inside the hydrogel domain to get:

$$F_{ij} = \frac{\partial x_i}{\partial X_j} = \delta_{ij} + \frac{\partial u_i}{\partial X_j} \tag{25}$$

where δ_{ij} is Kronecker delta, u is the displacement field, X and x are the material coordinates before and after the deformation, respectively. Figure 17 illustrates the how the traction scaling factor *dA/da* varies locally for a sample deformation field.

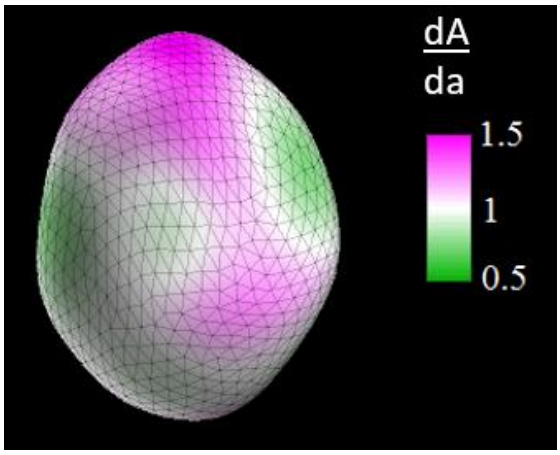

Figure 17. Dimensionless traction scaling factor, *dA/da* is calculated from the deformation gradient and surface normals of the undeformed and deformed configurations. It is used to locally scale the applied tractions and ensure force balance in the deformed configuration.

Figure 18 compares the local changes in the deformation field before and after applying the scaling factor. Although the effects are local and appear minor under heat map display, the transformation gives force balance on the body and ensures accurate traction calculation.

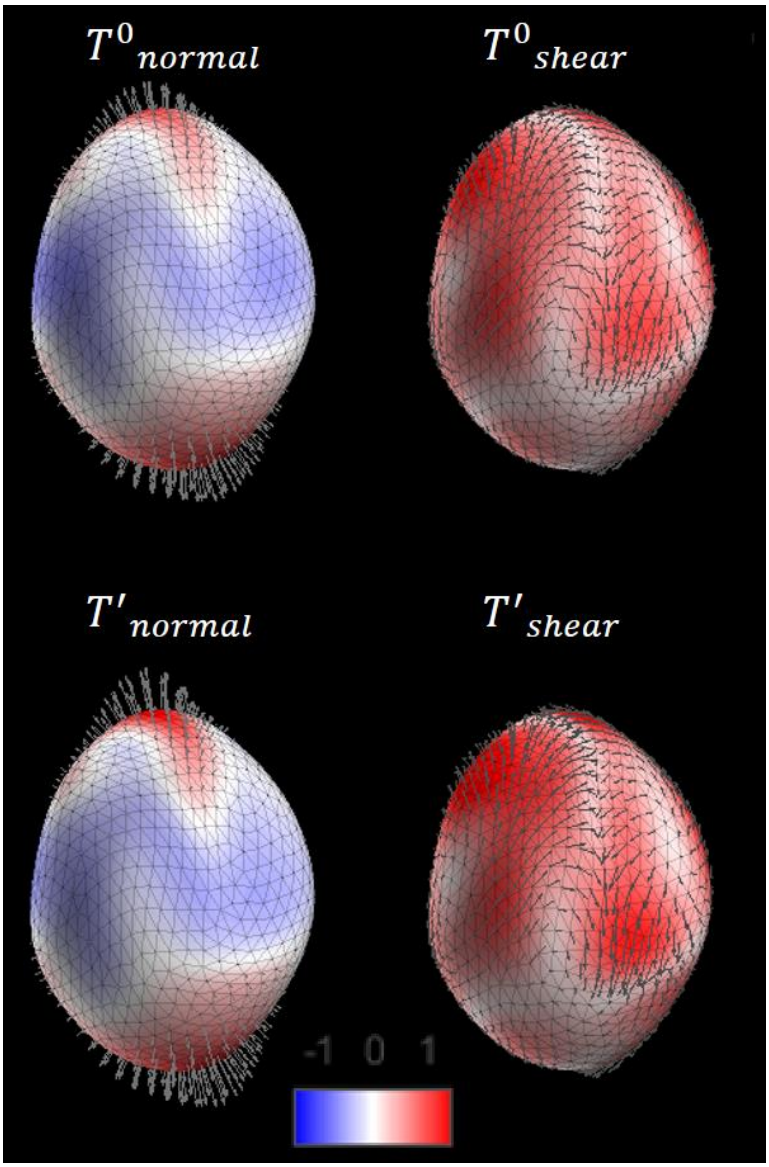

Figure 18. Normal and shear components of the traction fields with and without accounting for the local deformations on the boundary of the body. Heat map intensity is normalized to the maximal absolute intensity of the traction fields displayed.

D. Comparison of Simulated and Recovered Tractions in Surface-based MTFM

Given the nature of the shortest distance displacement mapping between the rest and deformed configurations, it is expected that our method, as implemented on a single boundary, would predict a predominantly normal loading profile and would severely underestimate the shear component of the total traction field. This is the case since the shortest distance mapping from the spherical boundary to the deformed boundary favors displacements that are almost normal to the deformed boundary, with very small to no in-plane displacements. To test this rather qualitative and intuitive prediction, we have implemented the surface based algorithm as described above and compared the simulated and *predicted* recovered tractions from single-boundary shape matching. Figure 19 shows that, as the truncation degree is increased in the spherical harmonics decomposition, the degree of freedom of the overall fit increases, which drives the solution to predict mostly normal forces, with shear components that are close to the noise levels (~10%). This confirms the naïve prediction that without point-wise deformation tracking, the single-domain microspheres could predict the minimum loading that generates the observed overall *shape* which corresponds to a loading profile that is mostly dominated by normal loading.

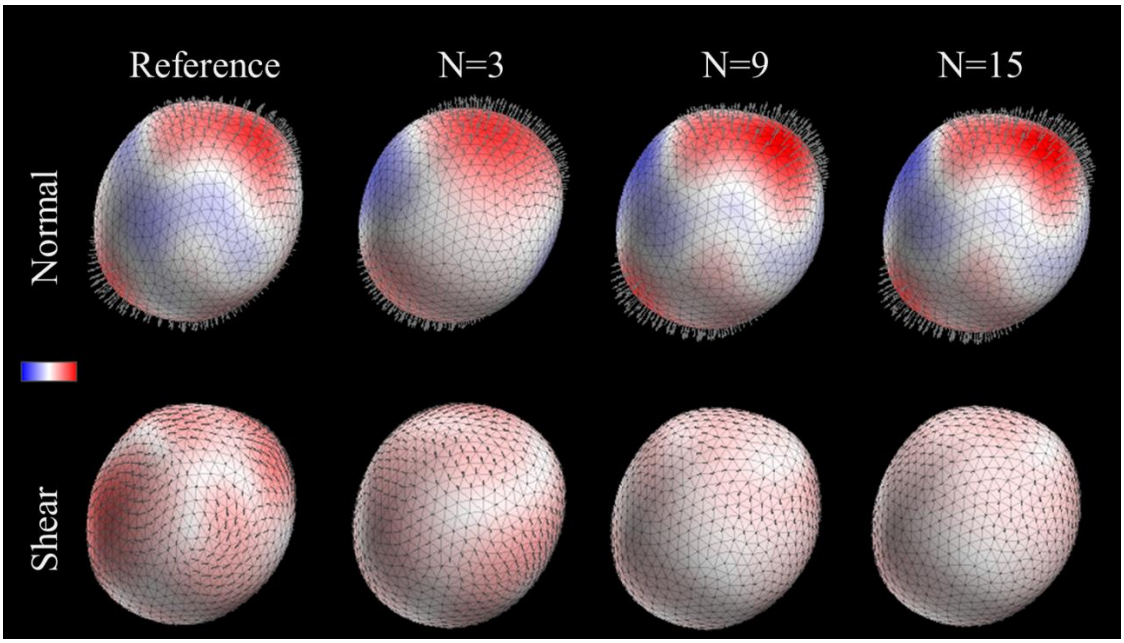

Figure 19. Single-colored microsphere force estimation by surface matching. As the truncation number *N* increases, normal loading profile converges and shear profile decays. Color bar is normalized to the highest magnitude of traction displayed.

IV. Development and Characterization of Microspheres for MTFM

To experimentally measure the traction forces exerted by cells, we employ the use of cell-sized solid hydrogel microspheres as force sensors. In selecting our components to synthesize these microspheres, we require a material that maintains low cytotoxicity, is elastic on the order of cell-exerted forces, and can be functionalized to promote cell-attachments. To satisfy these requirements, we chose the synthetic polymer, polyethylene glycol diacrylate (PEGDA), as the main component of our microspheres. PEGDA consists of the water-soluble and flexible polymer-linker, polyethylene glycol (PEG), flanked by two reactive acrylate groups. Its neutral charge, hydrophilicity, and resistance to protein adsorption have made it an attractive biocompatible option for *in vivo* and *in vitro* experiments [18]–[21]. Polymerization of the acrylate groups results in a covalently cross-linked solid PEG network. Changing the molecular weight of the PEG-linker or the weight fraction of monomers in solution allows for controlled and reproducible tuning of the elastic modulus [22]–[24]. Furthermore, exploiting the acrylate crosslinking permits the addition of other functional motifs into the cross-linked network, such as fluorescent probes to image microspheres or bioactive peptides to promote cell-attachments [25]–[27]. Specifically, we incorporated the polymerizable fluorescent monomer, rhodamine-B acrylate, to visualize the bulk and boundaries of the otherwise transparent microspheres via fluorescence microscopy. Furthermore, the inclusion of the integrin-binding peptide, Arg-Gly-Asp (RGD) coupled to a PEG-acrylate (PEGA) linker, promoted cell-adhesion to the surface of the microspheres.

In order to characterize the mechanics of the microspheres, we performed mechanical testing both on macroscopic samples and the microspheres and saw good agreement when

comparing the mechanical properties measured through macroscopic and microscopic methods. Assuming that hydrogels are linearly elastic, isotropic and homogenous materials, two independent material properties are necessary and sufficient to fully characterize their mechanical behavior. To this end, we chose to determine the shear modulus, G', and Poisson's ratio, ν, as these material properties can be directly measured using macroscopic mechanical testing of the hydrogels. To test the shear modulus of the hydrogels, we performed parallel-plate shear rheometry and for the Poisson's ratio measurements we built a soft gel stretcher and performed image processing on the axially stretched samples to characterize the amount of lateral shrinkage with respect to the applied axial stretch. Furthermore, as a comparison between the macroscopic materials and microspheres, we independently measured the bulk modulus of the microspheres by osmotic compression. We compared the Poisson's ratio values that we directly measured by the microscopic axial stretching tests, ν_M, and the value, $\nu_{\mu-M}$, calculated from the microscopic hydrostatic compression tests, K_μ, and macroscopic measurements of shear modulus as:

$$\nu_{\mu-M} = \frac{3K_\mu - 2G'}{3K_\mu + G'} \tag{26}$$

1. Microsphere Synthesis

To synthesize hydrogel microspheres, we exploited the high surface-tension between oil and water phases to form perfect spheres. A "pregel-in-oil" microscale emulsion containing droplets of an aqueous gel precursor phase was stabilized in a continuous oil phase by the addition of non-ionic surfactants [28], [29]. In detail, 3.9 mg/mL of Span 80 (Sigma; 85548)

and 1.1 mg/mL Tween 20 (Sigma; P1379) were dispersed into food-grade sunflower oil (Trader Joe's) and stirred for 10 minutes to create the oil-surfactant solution.

50 μL of the gel precursor was prepared by mixing 5% (v/v) PEGDA monomer (M_n=700 g/mol; Sigma; 455008); 1.1 mM lithium phenyl(2,4,6-trimethylbenzoyl) phosphinate (Tokyo Chemical Industry; 85073-19-4) photoinitiator [30], to enable crosslinking via UV excitation; 0.01% (w/v) rhodamine-B acrylate (Polysciences Inc.; 25404-100); and approximately 1 mM of RGD-PEGA.

The gel precursor solution was then added drop-wise to a vial containing 2 mL of continuously-vortexing surfactant-enriched oil. The shear forces created by vortexing the oil-phase cause the aqueous solution of gel precursor to break into poly-disperse micro-droplets, where the final range of sizes can be tuned by modulating the oil-water surface tension by adjusting surfactant concentrations. The vial was then filled to the brim with oil-surfactant solution, sealed, and sonicated using a benchtop bath sonicator for 10 minutes.

Immediately following sonication, the vial containing the oil and suspended gel precursor droplets was exposed to UV light to photopolymerize the gel precursor into solid spheres. In practice, the vial was placed between two handheld UV flashlights emitting light at 365nm, 3W and 5W for 10 minutes. During exposure, the vial was continuously rotated to allow uniform illumination throughout the bulk of the solution and was placed inside a chamber coated by aluminum foil to prevent light loss. Photopolymerization of the microscale emulsion resulted in the formation of covalently-crosslinked microspheres with diameters ranging between 5-50 μm, functionalized for cell-adhesion with RGD, and labeled with rhodamine-B, as shown in Figure 21. Microspheres were subsequently rinsed several

times with deionized water under centrifugation to remove oil and unreacted materials and stored for up to 2 days in cell culture media until used.

2. RGD conjugation to NHS-PEGA

RGD-PEGA was synthesized by allowing cyclo(Arg-Gly-Asp-D-Phe-Lys) (Peptides International; PCI-3661-PI) to react with acrylate-PEG-NHS (Sigma; JKA5023) at a 1:1 molar ratio in 50 mM sodium bicarbonate buffer at pH 8.4 at room temperature for two hours through an amine-ester reaction. Free (unreacted) RGD peptide was removed by dialysis with a Pur-A-Lyzer Midi Dialysis Kit with molecular weight cutoff of 1 kDa (Sigma; PURD10005-1KT) against 2 liters of deionized water that was replaced every 30 minutes for four hours. The subsequent solution was aliquotted to contain approximately 60 µg of conjugated RGD, lyophilized overnight, and stored at -20°C. Just before preparation of the hydrogel microspheres, the RGD-PEGA was added to the aqueous gel precursor solution to give a final RGD concentration of 1 mM.

3. Microsphere Attachment to Glass for Bulk Modulus Measurements

Bulk modulus of PEGDA microspheres was measured by first attaching microspheres to glass coverslips and imaging before and after mechanical loading. To achieve this attachment, glass coverslips were functionalized with (trimethoxysilyl)propyl methacrylate (TMSM) (>98%; Sigma; M6514) to link reactive methacrylate groups to a hydroxylated glass substrate via silanization. Glass coverslips (#1.5, Corning; 2975244) were degreased in a 1:1 solution of hydrochloric acid and methanol for at least 30 minutes and then thoroughly

rinsed with deionized water. Coverslips were then treated with concentrated sulfuric acid solution (>99%; Sigma; 339741) for at least 30 minutes to hydroxylate the glass surface, followed by thorough rinsing with deionized water. After drying with nitrogen gas, coverslips were placed in an organosilane solution containing 0.5% (v/v) TMSM and 0.3% acetic acid (v/v) in ethanol and allowed to react for at least 5 minutes. Finally, excess organosilane solution was removed by rinsing with ethanol. Functionalized coverslips were stored in airtight containers for up to 2 days. To attach microspheres to glass surfaces, dilute microsphere solutions (~10k/mL) were pipetted onto functionalized glass and cross-linked to via acrylate polymerization to surface-methacrylate groups upon 1.5 minutes of exposure to UV light. 1.5 minutes of UV-exposure was determined to be the minimum time required to maintain microsphere attachment to the glass coverslip surface during solution-exchange.

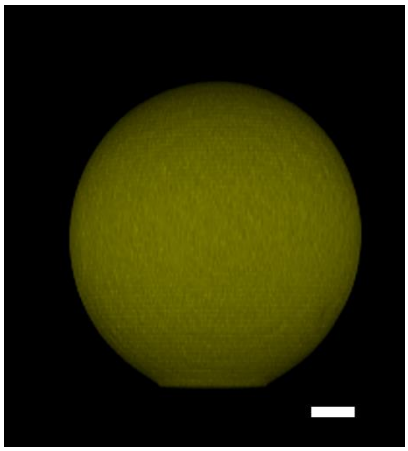

Figure 20. Side-view of microsphere attached to functionalized glass coverslips. Microspheres were covalently crosslinked to methacrylate linked to the substrate surface. The attachment area (as seen at the bottom of the image) is optimized to create a strong

enough bond to ensure that the microspheres do not float away during solution exchange, but that the flattened area does not substantially impact sphericity. Scale bar = 20μm.

4. Microsphere Bulk Modulus Measurements

The bulk modulus of the hydrogel microspheres was determined by measuring the change in volume under isotropic stress as described in [10][31][32]. The exclusion pore size of synthesized PEGDA microspheres was estimated to be less than 20 nm by fluorescence recovery after photobleaching (FRAP) measurements, which showed that fluorescent polystyrene particles with diameters of 20 nm do not diffuse through the hydrogel on the time scale of 1 hour as shown in Figure 21 [33][34]. An osmotic stress was externally applied by addition of a solution containing fluorescein-labeled, high molecular-weight (HMW) dextran (M_w=500 kD) (Sigma; FD500), which has a hydrodynamic radius of ~16 nm (and thus effective diameter of ~ 30 nm) [35]. Imaging of the fluorescent HMW dextran confirmed that no dextran penetrated microspheres.

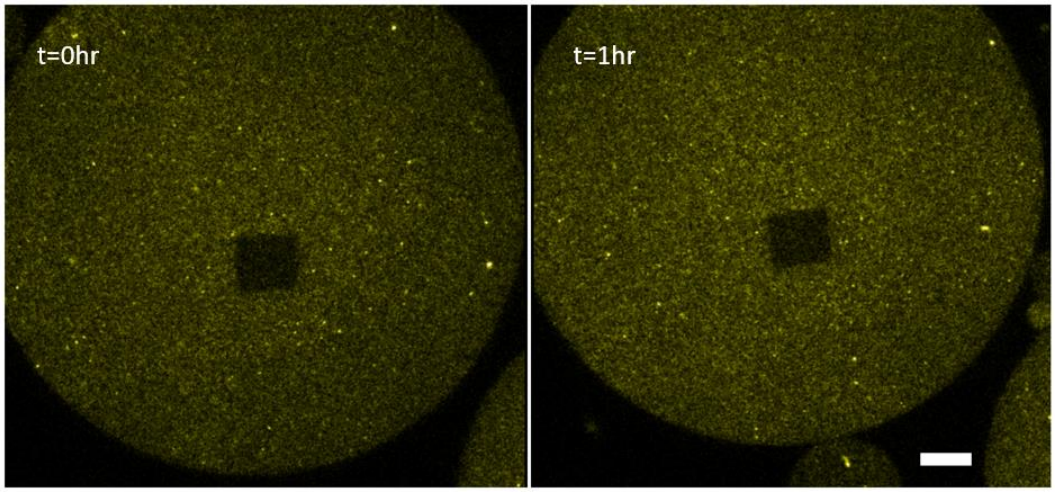

Figure 21. FRAP experiments in PEGDA microspheres fluorescent nanoparticles with 20-nm diameter. No fluorescence recovery is observed within one hour time window. Scale bar = 10μm.

Figure 22 shows the calculated osmotic stress as a function of the concentration of dextran as previously described in [32]. This externally-applied osmotic stress results in the mechanical compression of the microspheres. By imaging before and after solution exchange, we measured the total volume change in the microspheres of polydisperse sizes. The osmotic stress is applied by pipetting the Dextran solution directly on the coverglass, and since the microspheres are attached on the glass surface, they stay in the field of view before and after the solution exchange. Imaging was performed using a Leica SP8 confocal microscope and volume-change was calculated in ImageJ by measuring the change in microsphere radius from maximum-intensity projections. Measurements were collected for multiple sample-preps. The bulk modulus, K_μ, was calculated to be 10.35 ± 1.0 kPa from the

linear regime of the resultant compression stress-strain curve, as shown in Figure 22 below and it is similar to the bulk modulus measurements in previously reported microspherical hydrogel systems, which are ~15kPa [10].

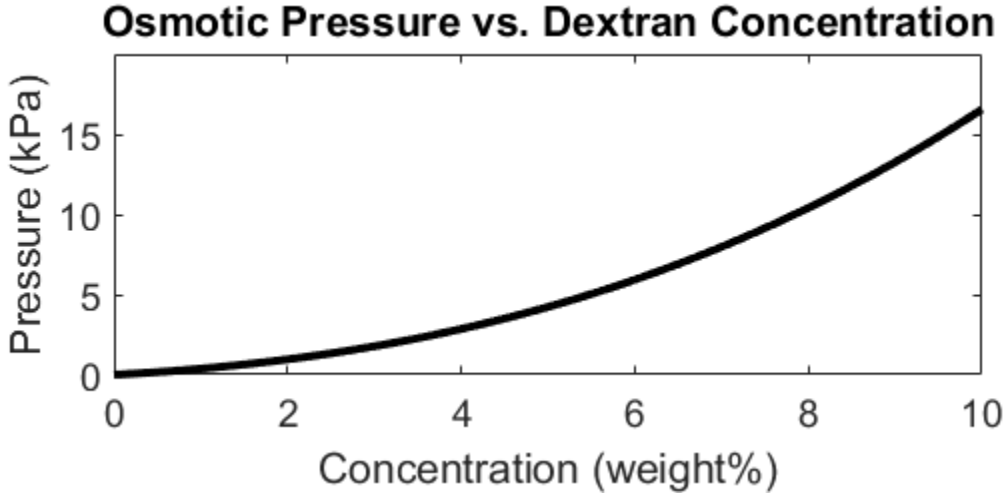

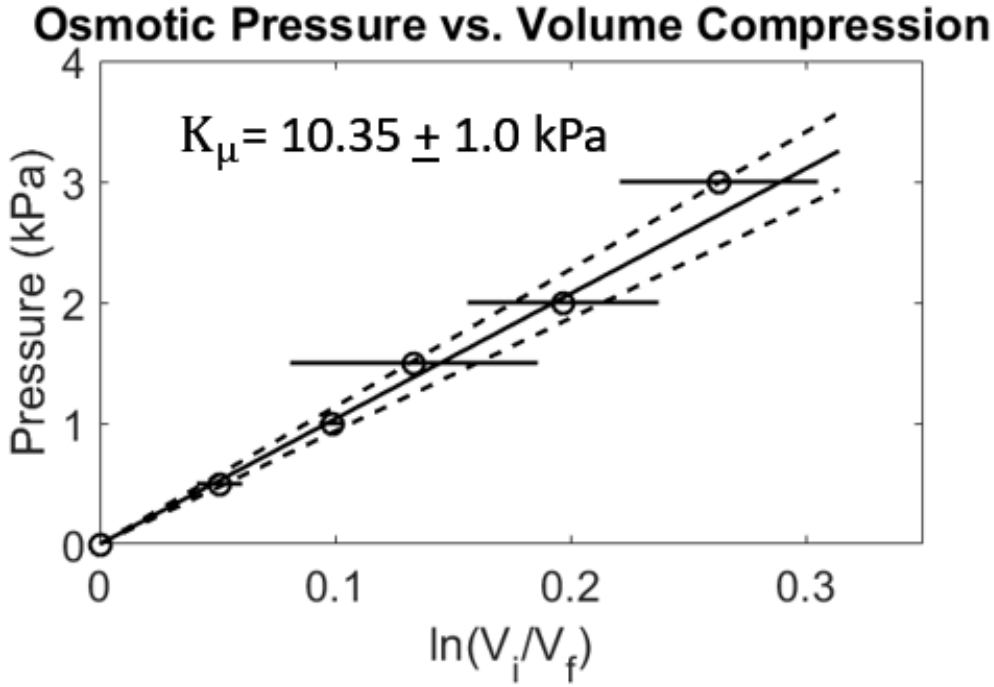

Figure 22. Microscopic bulk modulus, K_μ, is directly calculated on the microspheres from the volumetric strain and hydrostatic pressure caused by osmotic changes. Error bars are the standard deviation around the mean of a 4-7 samples measured at a given pressure.

5. Shear Rheometry and Poisson's Ratio Measurements on Bulk Samples

Bulk rheometry measurements of 5% (v/v) PEGDA hydrogels were performed on ARES-LS1 (TA Instruments) in a parallel plate geometry with a 7-mm gap. To prevent slippage at the tool-hydrogel interface, tool surfaces were coated with 400 grit sandpaper on tool and then superglue was applied gently on the top sandpaper surface just prior to compression of the hydrogel. Bulk gels were cast into metal rings and gelled in an aluminum chamber, under a benchtop UV source (Spectroline XX-15A), at a distance ~3cm away from the UV lamp. Even though we haven't seen any noticeable changes in the sample stiffnesses after 30 minutes, the samples are exposed for a total of 1 hour to ensure the photopolymerization reaction is completed. The rheological properties of the macroscopic gels were determined using oscillatory shear-loading at frequencies ranging from 0.1-10 Hz, at a fixed shear strain of 0.25%, which we confirmed was within the linear elastic range of the material (data not shown). The measured moduli show effectively no frequency dependence and the storage (elastic) modulus G' dominates the response, as expected [8]. As shown in Figure 25, we measured the mean value of G' to be approximately 0.97 ± 0.04 kPa whereas the loss moduli were lower by at least an order of magnitude over the measured frequencies and for three measurements done on one sample.

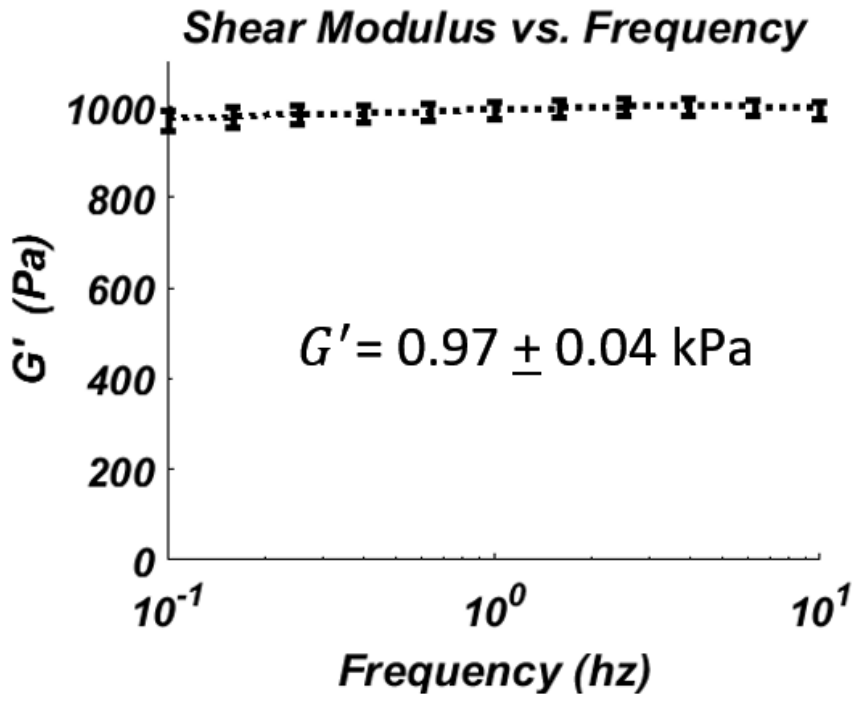

Figure 23. Storage (elastic) modulus, G', of macroscopic 5% PEGDA hydrogels was determined using shear rheometry to be 0.97± 0.04kPa by taking the value at the lowest frequency tested. This is because the timescales of the forces that cells apply are on the order of hours, and DC value of the shear modulus is physically the most relevant for the timescales involved in our system. Error bars are the standard deviation of three measurement points around their mean.

The material Poisson's ratio was independently measured using a custom benchtop gel stretching device. Poisson's ratio is defined as:

$$\nu = -\frac{\varepsilon_{lateral}}{\varepsilon_{axial}} = -\frac{(l^2_{lateral} - l^1_{lateral})/l^1_{lateral}}{(l^2_{axial} - l^1_{axial})/l^1_{axial}} = \quad (27)$$

where ε_{axial} and $\varepsilon_{lateral}$ are axial and lateral strains, and l^1_{axial} and l^2_{axial} are the distance between markers (steel shots) that are aligned in the axial (horizontal) direction, before and after the stretching, respectively. Similarly, $l^1_{lateral}$ and $l^2_{latreal}$ are the distances between the top and bottom borders of the gel as measured orthogonal to the axial direction, halfway between each steel shot at every frame.

Gel pre-cursor was cast into dog-bone-shaped PDMS molds and photocured. During attachment to the side walls of the gel stretcher with superglue, care was given to the alignment of the sample and the pulling axis of the stretcher. This was done by first bringing the flat side surface of the in contact with the fixed prong of the device (prong on the left), and slowly bringing the slider prong closer to the sample until chemical attachment is established between the hydrogel and the prong surfaces, ensuring that no noticeable compressive forces are applied on the gel that might cause off axis alignment and/or buckling of the hydrogel sample. The mounted samples are shown in Figure 24 below. Prior to curing, two pellets of steel shot were embedded on bottom of surface of the dish the gels were cast in and the displacement in their center of mass was detected using a standard MATLAB routine, *activecontour()*. We recorded the longitudinal displacement at the point that is halfway between the two steel shots in each frame recorded. This enables monitoring the gauge length for the same material points throughout the duration of the experiment. The RGB images were converted to greyscale and, at each frame, the crossing of the lateral axis and the gel boundary is detected by identifying the point of steepest descent to the pixel accuracy. By using (27) and relating the axial stretch and lateral shrinkage between loaded and unloaded states, we quantified the strains and their ratio, defined as ν.

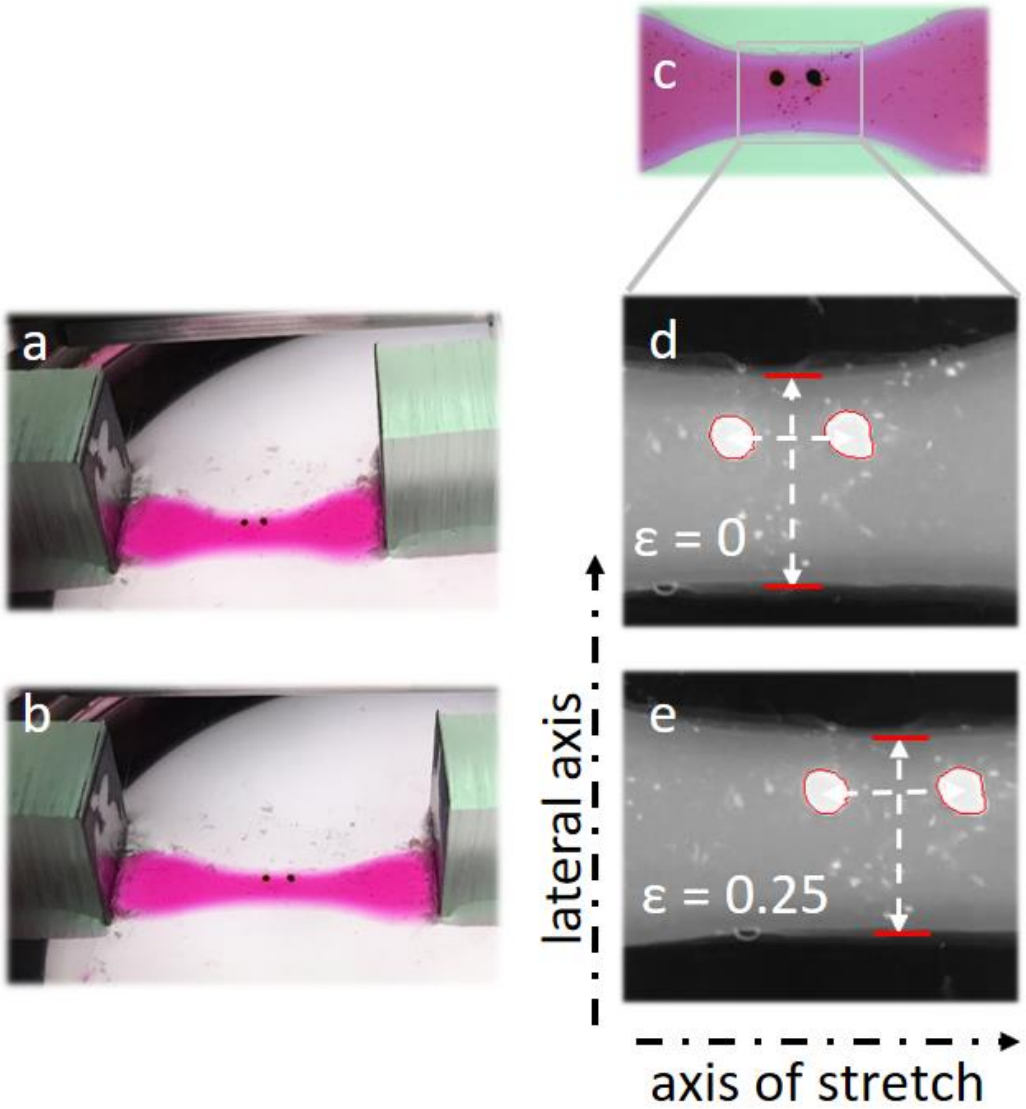

Figure 24. Hydrogels were cast into dog-bone shaped samples to enable tensile stretching in order to determine the Poisson's ratio of the material, which appears pink due to the rhodamine labeling of the gel. a) Hydrogel prior to stretching. b) Hydrogel sample under axial stretch. c) Top view of hydrogel and material tracers using an RGB camera. d-e) Grayscale images for image processing under axial stretch. The detected outlines of material tracers and gel boundaries are labeled with red.

In order to estimate the uncertainty in the calculation of the Poisson's ratio, we expressed the uncertainties associated with the strain measurements as:

$$\delta\varepsilon_j = \sqrt{\left(\frac{\delta l_j}{l_j^1}\right)^2 + \left(\frac{l_j^2 \delta l_j}{{l_j^1}^2}\right)^2} \tag{28}$$

where *j* denotes the direction as lateral or axial, l_j^1 and l_j^2 are lengths in the *j*'th direction, measured in pixels, and δl_j are the uncertainties associated with the axial and lateral directions. The stretch markers are detected by using active contours in MATLAB and the centroid of the segmented markers are assumed to have subpixel resolution and δl_{axial} is taken as $\pm$ 0.5 pixels, whereas locating the gel boundary in the lateral direction has pixel resolution, so $\delta l_{lateral}$ is taken as $\pm$ 1 pixels. The errors are propagated to the strain measurements as shown in (28), and the Poisson's ratio is calculated from the slope of the line that if fitted to the $\varepsilon_{lateral}$ vs. ε_{axial} curve. The fit is carried out by using the MATLAB routine *linfitxy()* by J.Browaeys, (University of Paris, Diderot), which uses both *x*- and *y*-error bars for calculating the best fitting parameters and computes the error bounds on the fit parameters using a Monte Carlo simulation, where each data point is Gaussian-distributed in *x* and *y*, with a standard deviation that is specified by the error bar. In our fit, we force the curve to go through (0,0), and report the 95% confidence bounds on the fitted value of the Poisson's ratio, ν.

As shown in Figure 27, the Poisson's ratio for the PEGDA hydrogels was determined from the ratio of lateral and axial strain to be ν=0.45 $\pm$ 0.035 As a consistency check, we compare the calculated values of Poisson's ratio using the microscopically measured bulk

modulus, K_μ, and the macroscopically measured shear modulus, G', using the following equation:

$$\nu_{\mu-M} = \frac{3K_\mu - 2G'}{3K_\mu + G'} = 0.455 \pm 0.005 \tag{29}$$

The error bar in the above expression is calculated by propagating the uncertainties in the measurements of shear modulus, $\boldsymbol{\delta G'}$, and the microscopic bulk modulus, δK_μ, by following the formalism that is presented in (28), and using the equation (29). Looking at the macroscopically measured Poisson's ratio, $\nu_M = 0.45 + 0.035$, and the calculated value, $\nu_{\mu-M} = 0.455 \pm 0.005$, we see that the mean values of these two measurements of the Poisson's ratio compare well with each other. This might help provide an independent confirmation that the rheological and mechanical properties of the PEGDA-based hydrogels be are invariant over the length scales (> 5μm) considered here. In the future, more careful measurements of the macroscopically measured Poisson's ratio, ν_M, can help lower the error associated with ν_M.

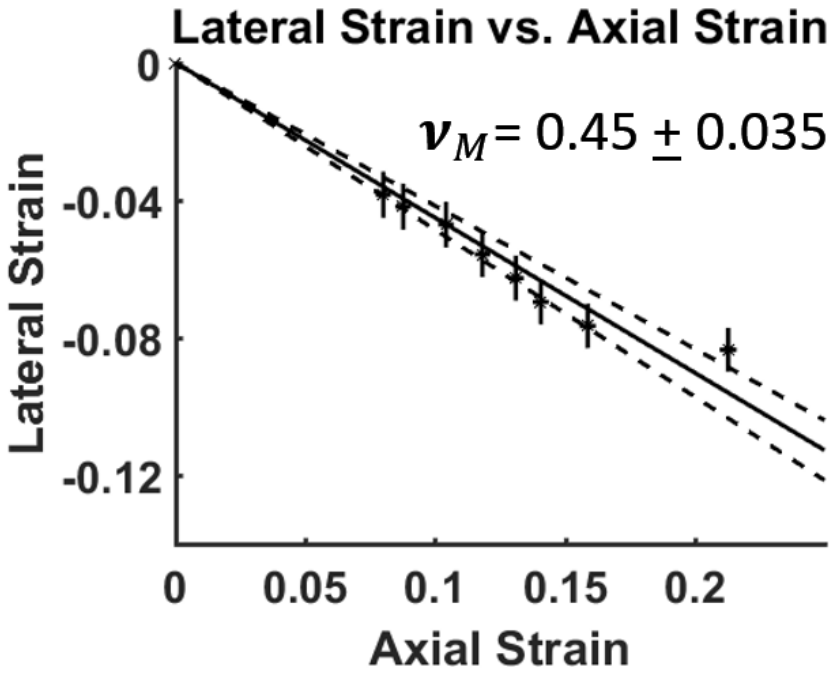

Figure 25. Axially stretched macroscopic 5%PEGDA hydrogel samples show weak compressibility with a Poisson's ratio of 0.45 ± 0.035. The error bounds shown are one standard deviation around the mean value of the fitted parameter, ν_M.

V. Experimental Methods and Cellular Studies

In these studies, NIH-3T3 mouse fibroblasts were used to investigate mammalian cell adhesion, spreading, and force transmission on our microsphere surfaces. NIH-3T3 fibroblasts were chosen because of their frequent use in TFM studies [6], [8], [36], [37]. Their integrin expression pattern, focal adhesion assembly, and spreading have been previously well-characterized [38]–[41]. Additionally, they have been used in studies of cell functions such as cell shape change, adhesion, movement, and to demonstrate key roles of cytoskeletal components in cell adhesion, division, and growth [42]–[44].

Briefly, we mixed RGD-functionalized microspheres into dense solutions of cells that were seeded into custom microwells treated to promote cell attachments. Using this method, we were able to obtain microspheres encapsulated within several layers of cells and fixed in position. We employed the use of high-resolution confocal microscopy to image optical sections that were then reconstructed to give three-dimensional information with high spatial resolution. By imaging both the deformed and the undeformed, load-free states of the microspheres, we were able to track the displacement of the microsphere surface and compute the nominal values for the normal component of the total active traction forces exerted by cells on the microspheres. We also labeled the living cells for actin and consistently observed that bundled actin cables in the cell cortex have a high spatio-temporal correlation with local microsphere deformations.

A. Experimental Methods

1. Fabrication of custom PDMS-coverslip microwells for cell experiments

To image multiple cell-microsphere interactions under different experimental conditions over several hours, custom microwells were constructed. Cured polydimethylsiloxane (PDMS) (Dow Corning; Sylgard 184) slabs of ~3 mm thickness were cut with 6-mm-diameter holes, sterilized with 70% ethanol, and plasma bonded to glass coverslip substrates to form glass-bottomed, PDMS microwells. Microwells were then treated with either a 10 μg/mL solution of fibronectin (Sigma; F2006) or 0.01% poly-L-ysine solution (Sigma; P4707) to promote cell adhesion and spreading and were subsequently stored in airtight sterile containers at 4º C for up to one week until used.

2. Cell culture and staining:

Mouse fibroblast (NIH 3T3) cells were obtained from the American Type Culture Collection (ATCC; CRL-1658) and maintained in high-glucose DMEM containing phenol red and supplemented with 10% calf bovine serum (ATCC; 30-2030) and 1% penicillin-streptomycin (Life Technologies; 10378016). Cells were grown in 25 cm^2 rectangular canted-neck cell culture flasks with vent-caps (Corning Life Sciences; 430639) at 37° C in the presence of 5% carbon dioxide, and were either passaged or used for experiments at 60-80% confluency. Prior to experiments, cells were stained with Hoechst 33342 (Life Technologies; H3570) to label cell nuclei and a commercially-available live actin stain called SiR-actin to label filamentous actin throughout the cells (Cytoskeleton Inc.; CY-SC001) and imaged immediately.

3. Cell microsphere experiments

Mouse 3T3 fibroblasts at 60-80% confluency were detached from cell-culture flasks by addition of 0.05% trypsin containing 0.2 g/L EDTA (ThermoFisher; SH3023602), rinsed to remove trypsin-EDTA solution, and stained with 10 μg/mL Hoechst-dye 33342 and 1 μM SiR-actin label. RGD-functionalized microspheres were added to solutions of suspended 3T3 cells at a 1:30 ratio (microspheres:cells) and the cell-microsphere solution was then diluted to a final cell concentration of ~1.5-2 million/mL. Approximately 50K-100K cells with microspheres were immediately seeded into the custom microwells and imaged.

50-100 μm^2 fields of view were imaged on a Leica SP8-TCS confocal microscope[2] using a 40X water-immersion objective with numerical aperture of 1.1, at a 1000 Hz acquisition rate, and pinhole diameter of 1 Airy Unit. Imaging took place in a humidity-controlled environmental chamber with a temperature setting of 37ºC and 5% CO_2. To minimize fluorescent bleed-through between imaging detectors, line-sequential scans were taken. The first sequence comprised a 405 nm excitation with 430-500 nm detection to image nuclei staining, as well as a 555 nm excitation with 600-680 nm detection to image diffuse rhodamine-B labeling of microspheres. The second sequence consisted of a 652 nm excitation with 665-730 nm detection to image the stained filamentous actin. Stacks ranged in height from 20-75 μm and took approximately 1-2 minutes to collect depending on stack-height.

[2] NSF Award DBI-1625770, through the Major Research Instrumentation Program.

To observe initial cell interactions with microspheres and obtain microsphere loading information over small time increments, we conducted time-lapse experiments. Cells and microspheres were seeded into PDMS microwells and immediately imaged as described above. By using a motorized stage, multiple separate locations containing cells and microspheres were selected to be imaged overnight. Image stacks were collected every 30 minutes at each location, generating time-series data for all selected locations.

For the experiments to measure cell tractions, cells were allowed to settle on the surface in the presence of microspheres and allowed to establish attachments with and deform the microspheres for several hours. During this time, image stacks were collected as described; measurements were performed using a heated incubation chamber that maintained the appropriate temperature and CO_2-concentration (37°C, 5%) to ensure cell health. After imaging, cells were released by either lysis using a low concentration sodium dodecyl sulfate solution (<0.1% w/v) (Sigma; 151-21-3), or through the disruption of cell attachments by proteases and chelating agents (in the form of trypsin-EDTA), inhibition of actin polymerization by 4 μM cytochalasin D (Sigma; C8273), or through inhibition of the contractile actin-binding motor protein myosin II by 50 blebbistatin μM (abcam; ab120425) as previously employed [8], [9]. Inhibiting the active force generation mechanisms of the cells and cleaving cell-hydrogel attachments, or lysing the cells removes the actively-generated cellular loading on the microspheres and spheres go back to their load-free spherical configuration.

B. Experimental Results in Cellular Systems

In this work we mainly used NIH 3T3 mouse fibroblasts as they are widely used and accepted models for validation and proof of concept for traction force microscopy studies, as discussed previously. The early experiments we conducted with 3T3s showed that the RGD-functionalized microspheres were able to promote cellular contacts, resulting in substantial deformation under cellular loading. Figure 26 shows examples of natural cell-microsphere interactions where cells (shown in red, by SiR actin labeling) are able to form stable attachments with microspheres, while maintaining their natural contacts with the neighboring cells. In cases where the microspheres are small enough for the cells to fully wrap around, we occasionally observed complete engulfment of the synthetic hydrogels by the 3T3s.

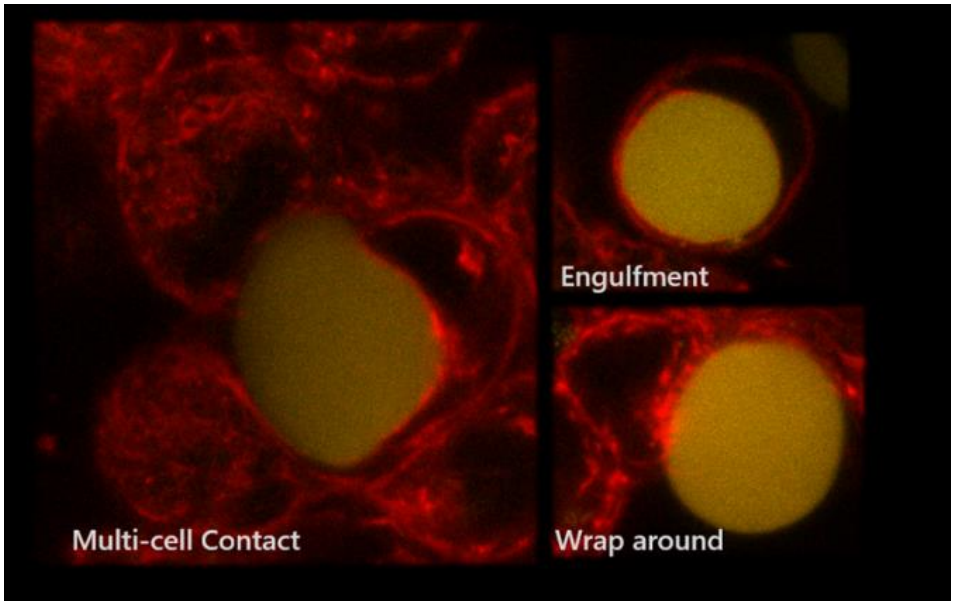

Figure 26. Representative examples of various natural cell-gel interaction modalities that are typical in cellular experiments. 3T3 mouse fibroblasts which are labeled with SiR actin

(red) are strongly interacting with the RGD-functionalized rhodamine PEGDA microspheres (yellow). Note the high levels of actin fluorescence around the regions of maximal hydrogel deformations.

As we discussed in Chapter III, single-color solid microspheres can provide information about the normal component of the total traction field that is applied on the spherical gel boundary. However, in order to determine the *nominal* values of the boundary tractions rather than the anisotropic tractions around a mean value, we would additionally need to know the load-free configuration of the hydrogels. Since we know in the absence of external loads the gels assume a spherical shape, the only parameter needed to determine the nominal values of the normal tractions is the hydrogel radius in the rest configuration. This can be achieved either enzymatic or surfactant treatment of cells and/or cell-gel interactions. However, when the microspheres are imaged in their deformed configuration and no prior information is available, by invoking constant volume (not-incompressibility) between the rest and deformed states, we can measure local deviations around the hydrostatic component of the normal force, similar to [9]. An example of this is given in Figure 27. The left panel shows a 3D rendering (Leica Suite) of the rhodamine labeled and highly-deformed and 5% PEGDA microsphere (red) as well as the actin (pink) meshwork and actin cables going around the body. It is remarkable that the location and the orientation of the actin cables line up with the regions of maximal deformations on the hydrogel body. As described previously, upon 3D rendering of the deformed hydrogel surface, we are able to quantify the normal boundary forces by assuming different initial volumes, V_o, as the volume is the only

quantity needed in order to fully characterize the rest configurations of the microspheres. Clearly, different choices of the initial volume lead to predicting different loading profiles on the body. However, the main difference between the right and middle panels is the inward hydrostatic traction that is required to match the initial and final volumes in the right panel. Furthermore, what is common between the two calculated traction profiles is the deviatoric part of the boundary loading, which does not cause uniform volume changes across the body, but rather generates shape changes at constant volume.

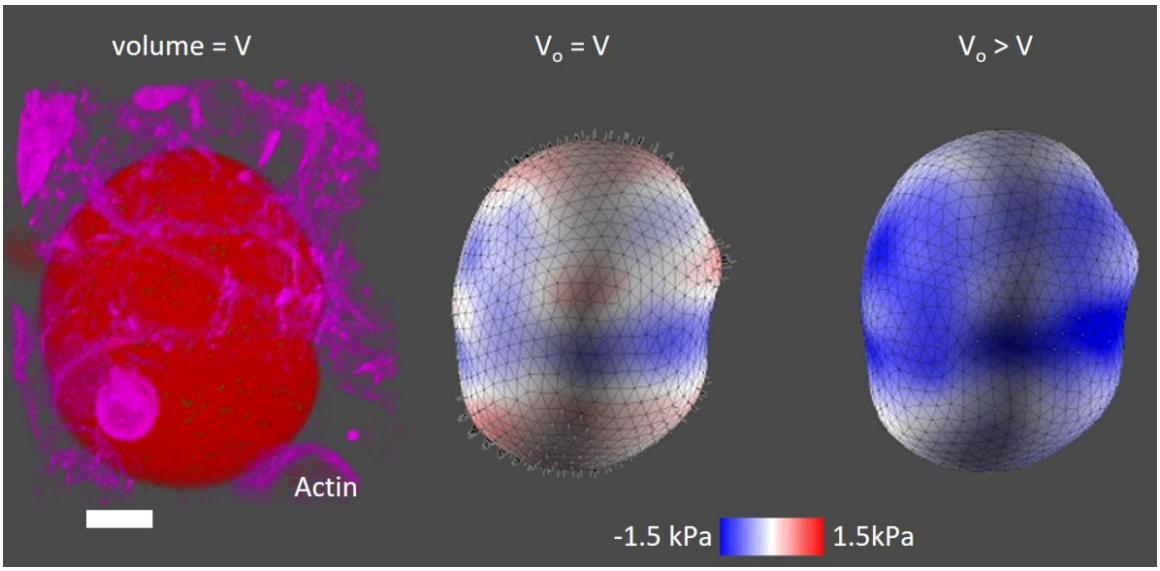

Figure 27. Left: A rhodamine labeled PEGDA microsphere (red) is deforming under the traction forces applied by the surrounding 3T3 mouse fibroblasts via actin cables that are labeled with SiR actin (pink). Middle: Anisotropic normal tractions relative to the mean (hydrostatic) traction show relative compressive stresses around the sites of actin cables. Right: Comparison of the volumetric changes before and after release experiments show that the microspheres are under overall compression. Heat map on the middle and right panels

indicate the estimated values of the normal tractions on the deformed body. Scale bar is 5μm.

Under these circumstances, the natural question of which initial volume to pick arises. In the absence of any additional information about the initial or the current state of the body, it is rather intuitive to set the initial volume to be equal to the final configuration and quantify the anisotropic deviations around the mean hydrostatic tractions, as in [9]. However, as demonstrated with the osmotic compression tests, PEG microspheres are compressible and they would undergo volumetric changes if the active tissue stresses are relieved by cytoskeletal inhibitors or surfactants until the gels assume sphericity. In this case, hydrogel microspheres would predict the *nominal values* (with respect to 0 kPa) of the active forces that were originally applied on them, at the deformed configuration, which is an improvement over the microdroplet based methods.

F. Conclusion

Although the single boundary MTFM method only sets a lower bound on the arbitrary loading that might be applied by cellular systems to create the observed final shape of the microspheres and predicts mostly normal loading, it is very robust to tissue dependent imaging artefact which increases its potential utility in complex geometries and highly scattering tissues. Also, another major advantage of this method is the fact that because it is purely based on *shape matching*, it doesn't require information about the starting

configuration of the system since the force transducers have fully spherical geometry at their rest configuration. Experimentally, this property removes the condition to release the cell-gel attachments in order to get the load-free state of the microgels - which greatly simplifies the experimental procedure. This can be desirable for certain experiments, where the microspheres are placed inside a living organism or a tissue that needs to be kept functional following the experimental procedure. Furthermore, this method does not rely on particle tracking as material tracers, which eliminates the requirement to perform bead detection and tracking/point cloud matching of the bead coordinates between the deformed and undeformed configurations. This greatly reduces the computational challenges that are associated with particle tracking, especially in the case where the total displacements of the beads are larger than the average inter-bead spacing in the point clouds, ~1μm for microspheres, which is typical for the deformations that microspheres experience under cellular loading.

Single-colored microspheres present cells with a geometry and surface with which they can mechanically interact more naturally than the current existing methods, in being able to apply both shear and normal forces on the solid microspheres, as well as maintaining contacts with the neighboring cells. Even though the shear loading applied by the cells on the microspheres mostly goes undetected with this technique, the total interactions between the cell and the microsphere mechanically mimic that of cell-cell interactions much more closely than the existing methods. In addition, under these more natural mechanical interactions we can still get a good *estimate* of the normal tractions applied on the body with minimal additional experimental and computational effort.

VI. Microsphere Traction Force Microscopy Future Work

A. Particle Tracking-based MTFM

1. Experimental and Computational Methods

Determining the unique force field that cells apply on the solid microspheres requires having information about the displacements of the material points between the rest and deformed configurations. To achieve this and track the displacements of the material points inside the hydrogel bodies, we included 200 nm fluorescent particles that are trapped in the microstructure of the hydrogels. In our hydrogel preparation, we keep the fluorescent particle number density, ρ, constant, which means the number of particles inside the body scales with the volume. We define the number of beads, N, as:

$$N = \rho r^3 \tag{30}$$

where we have optimized the bead density in our hydrogels such that the point spread functions have minimal overlap in *z*, giving $\rho \approx 1$ beads/μm^3. Figure 28 below shows an representative example of a hydrogel microsphere ~25μm in diameter, which is of the typical size used in our experiments.

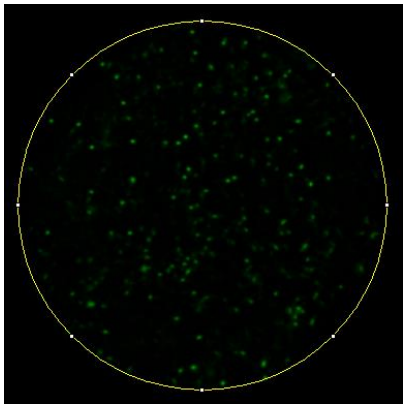

Figure 28. Example of a hydrogel cross section which shows the internal fluorescent bead distribution used in experiments. (The yellow circle outlines the microsphere boundary, with a diameter ~25μm.)

Upon imaging the microspheres under cellular loading, we perform bead detection with the Kilfoil implementation of the Crocker-Grier particle tracking algorithm[45][46] in MATLAB. To quantify the measurement uncertainty in bead detection and tracking, we selected an undeformed microsphere that is located in between cells and we took five consecutive scans of the same image volume. Since the microsphere was known to be initially undeformed and is not expected to deform between such rapid consecutive image volume recordings, it served as a control. Upon performing fluorescent bead detection on the individual image volumes of the same physical microsphere, we obtained five particle clouds which only exhibit slight translations and rotations around the center of the hydrogel in which they are embedded. Therefore, we match the position and the orientation of these detected point clouds to each other using the Iterative Closest Point (ICP) cloud matching algorithm as explained in [18] and [48], and subtract out the rigid body translations and rotations of the point cloud from every point in the cloud. Upon matching the orientation and the position of the consecutive point clouds, we track the particles using the Crocker-Grier algorithm, and establish one-to-one matching of the beads in all 5 time points. As seen in Figure 29, the resulting distributions for the bead displacements show that the measurement noise that is associated with bead detection and tracking is σ_{bead} = (0.039μm, 0.045μm, 0.144μm) in *x*-*y*-*z* directions, respectively.

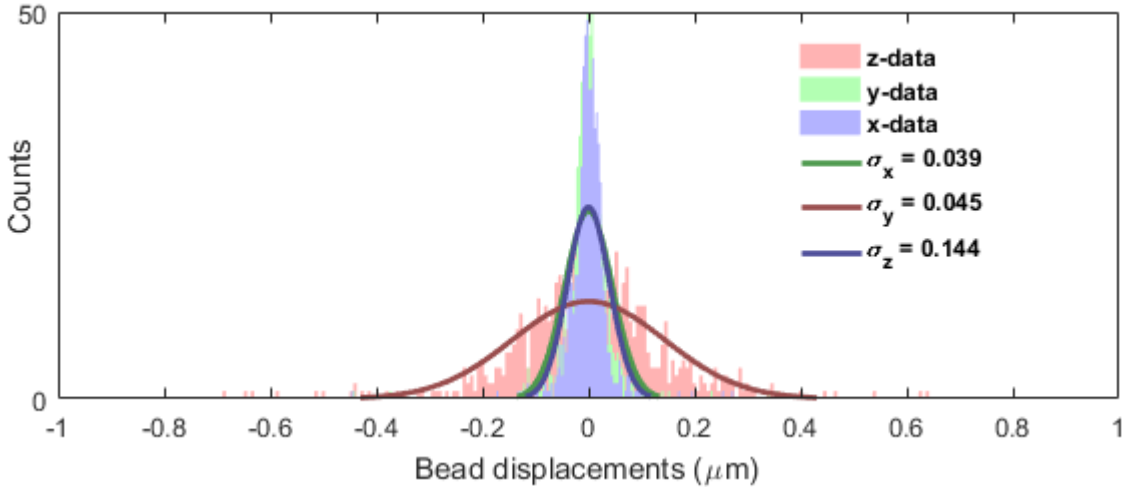

Figure 29. Bead displacement tracking error over five consecutive stacks of the same field of view.

2. Deformation Simulations under Noisy Data

In the previous section we characterized the errors associated with detecting and matching fluorescent particles between time-lapse volumetric imaging of particle clouds that are seeded in hydrogel microspheres. This is a typical experimental setting in which the microspheres are free to interact with the cells while being imaged at the same time. This means that the particle tracking errors that are characterized in the previous section can be modeled, and these models can be used as realistic predictors of the measurement noise that is inherent to the imaging, detection and tracking of the fluorescent particles in the experiments. However, it is typically experimentally challenging to apply controlled, known force fields to the microspheres and characterize effect of measurement noise on the ultimate fidelity and versatility of the traction reconstruction. Thus, we simulate known force fields and calculate the corresponding displacements, u_s, for the given loading. Once the

simulated displacements are computed, we add the Gaussian noise, δ, which fits the experimentally observed tracking errors as shown in Figure 29 and previously discussed in [8]. We denote this *noisy* displacement field as $u_s + \delta$. By accounting for this experimentally-consistent system noise and by solving (15) and minimizing the residual, we recover a displacement field, u_r, that closely matches the simulated displacement field, u_s. In Figure 30 the corresponding displacement values for randomly picked surface points on the hydrogel boundary are plotted against the simulated displacements. The broken line is a guide for the eye that indicates one-to-one correlation between the simulated displacement field, u_s, and itself. Therefore, the amount of deviation from the diagonal is indicative of a deformation field that is not representative of the simulated, known displacement field, u_s. As seen in Figure 30 the recovered displacements, u_r, match the simulated displacements more closely than the noise added displacement field. This good agreement is due in part to the fact that we are using a spherical harmonics formulation where the basis functions are described over the whole boundary, thus, are robust to the deleterious effects of the local noise, as opposed to point load-based Green's function formulations in finite element models of boundary loaded elastic deformations [8], [37].

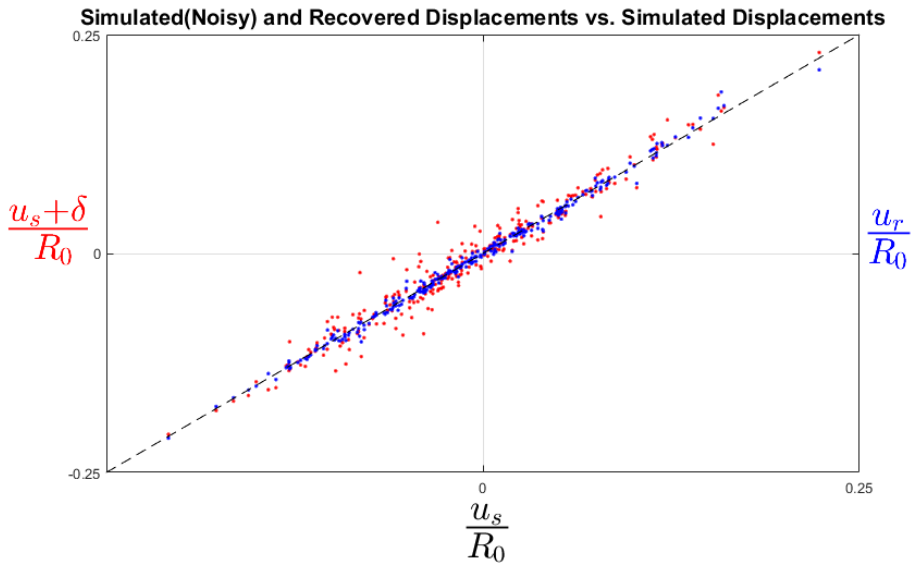

Figure 30. Simulated and recovered displacement fields show that solving the minimization problem suppresses the high frequency noise in the displacement field inside the body and predicts a more *regular* solution, u_r.

3. Comparison of Simulated and Recovered Traction Fields

To test the fidelity of our method and quantify the effects of measurement noise in the calculated boundary traction field, we carried out simulations by starting with a randomly chosen, known value of the modal contribution vector, a, and we forward simulate a traction field and the corresponding displacements. The left panel in Figure 31 shows the total simulated traction field, and the shear and normal decompositions. Then, based on our tracer tracking error measurements, we introduce a Gaussian noise on top of the simulated displacement field and solve the minimization problem posed in (17). Looking at the

agreement between the simulated and recovered displacements and tractions, we conclude that, our method is robust to the realistic experimental noise and can be used to succesfully reconstruct traction force profiles from experimental data. The resulting recovered traction field is displayed on the panel of Figure 31. It is clear that our method can capture the total traction field, and moreover allows the individual normal and shear components to be determined. In the middle panel, we display the local deviation from the simulated traction field by using the relative local error metric:

$$\text{Relative local error} = \frac{|T'_{simulated} - T'_{recoevred}|}{|T'_{simulated}|} \tag{31}$$

For the experimentally relevant noise levels, we find that the recovered tractions are in ~ $\pm$ 20% agreement with the simulated tractions, which is on the upper end of the predictive capabilities of most traction force microscopy methods at these short length scales, ~10-20μm [8]. The middle panel in figure 19 displays the relative local error in the total traction field on the deformed boundary.

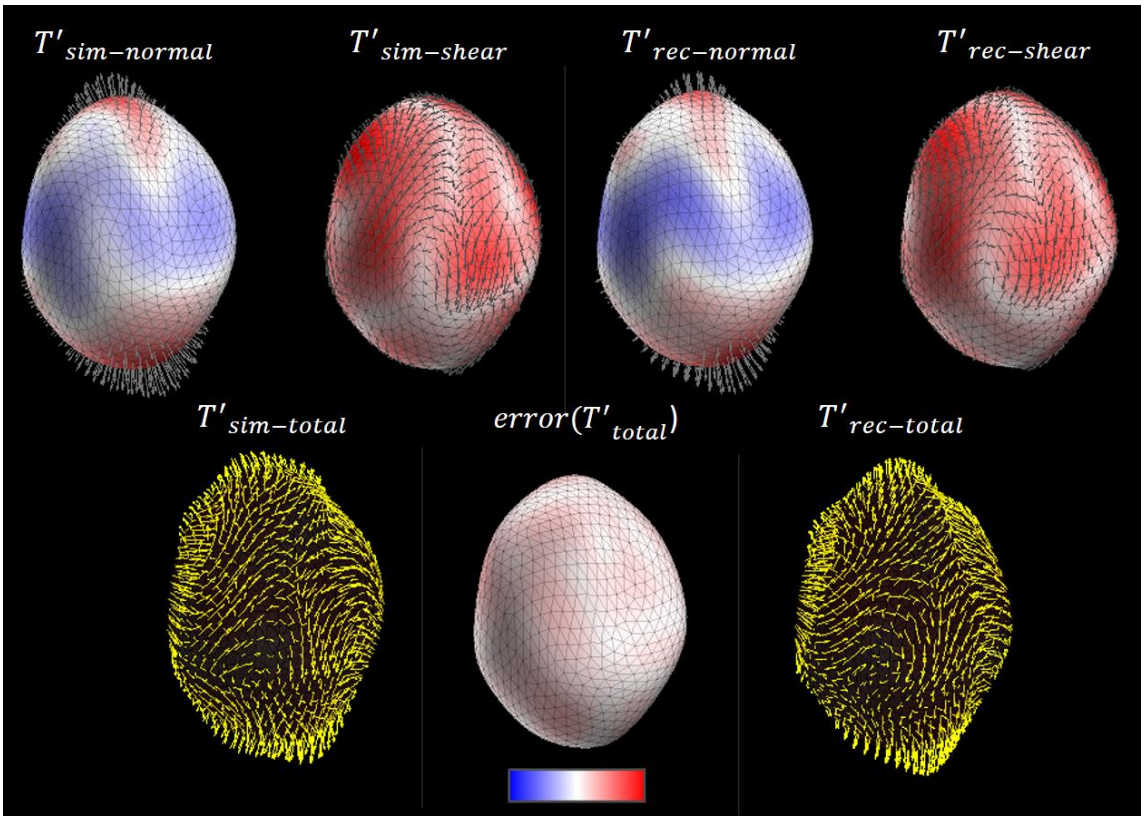

Figure 31. Simulated and recovered tractions show that the tractions calculated by our method agree well with the simulated values, with maximal local deviations of ~20%. Heat map intensity is normalized to the maximal value of the magnitude of the traction field.

4. Preliminary Experiments in Cellular Systems

We recently started cell experiments using microspheres seeded with 200 nm fluorescent (excitation 505nm/emission 515nm) polystyrene particles and had great success in terms of optimizing the bead density inside the microspheres, setting up the experiments and establishing cell-gel attachments, as some of our pre-established expertise carried over from the previously described studies on developing and performing MTFM. In Figure 32, a 3D rendering of a preliminary study of particle based-MTFM is shown. The volume image is recorded while cells are establishing contacts with the fluorescent particle seeded microsphere and extending bundled actin cables on the microsphere surface.

Even though we had some preliminary success with jump-starting this technique, particle-based MTFM has inherent experimental and computational challenges to itself. This is in part due to the fact that in the context of MTFM, the microspheres are free-floating sensors that are designed to be embedded in 3D cell aggregates and/or thick tissues; and depending on the cellular tissue that lies in the optical path, the point spread functions of the polystyrene particles can severely and anisotropically deteriorate. This directly impacts the accuracy of the bead detection and tracking, thus reducing the reliability and the utility of the method. We have attempted to minimize these optical aberrations by plating only a few layers of cells with microspheres with some preliminary success. Minimizing the number of cell layers that lie between the microspheres and the objective helps reduce the cell induced anisotropic absorbance, scattering and refraction; however, if microsphere based traction force microscopy methods are to be furthered, these challenges will have to be more systematically addressed.

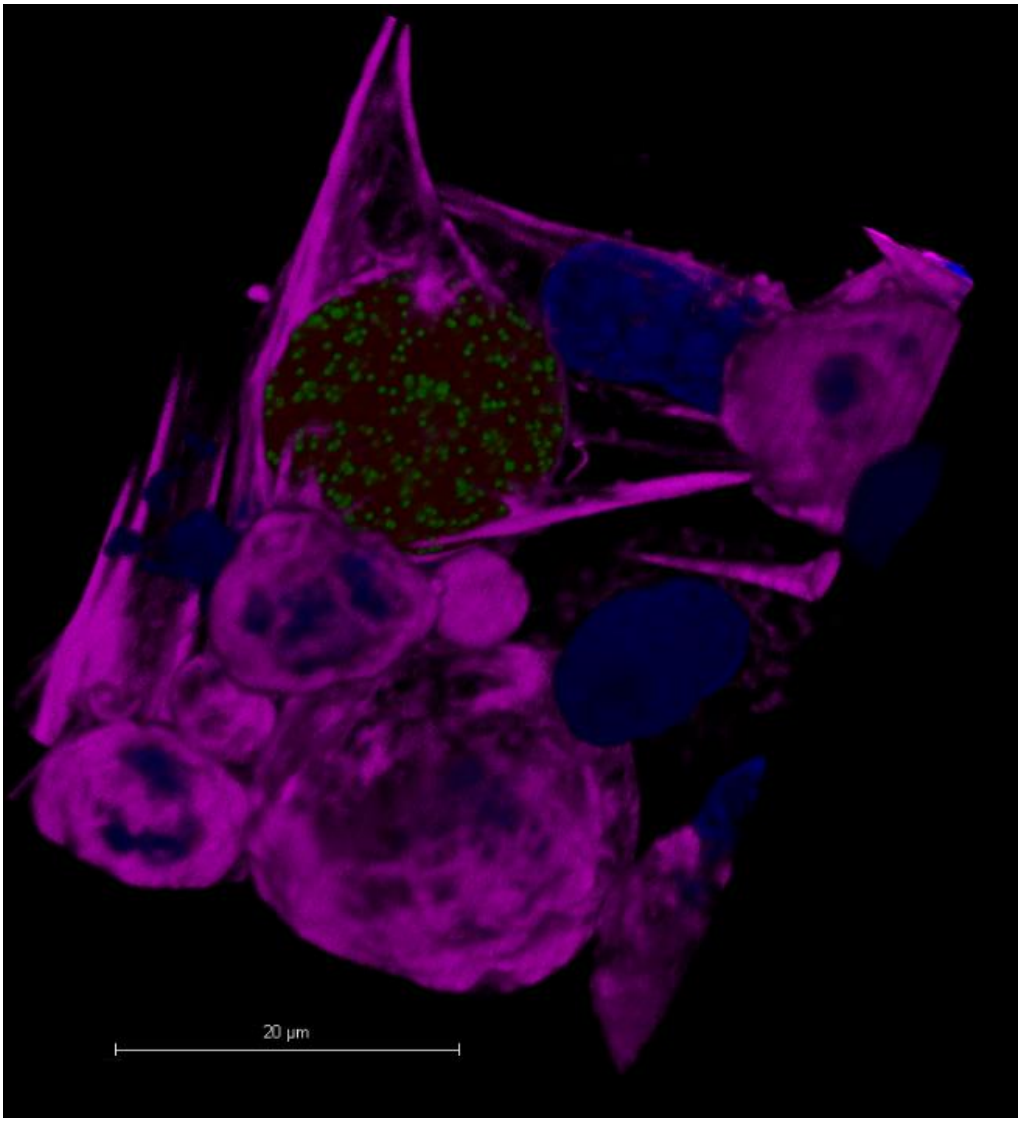

Figure 32. Multiple mouse fibroblasts making contact with poly-l-lysine functionalized microsphere. Stable actin cable formation with PLL microsphere surface is apparent. Green=FITC particles, red=rhodamine-labeled PEGDA, magenta=SiR actin, blue=Hoechst.

Although under the current experimental condition, imaging limitations prevent the use of microspheres seeded with fluorescent particles for probing the mechanics of the interior of large cellular aggregates, further development of MTFM methods that are robust to imaging artefacts could help elucidate the full features of cellular traction forces in the natural context of cellular systems. In the next section, we propose and discuss methods that can provide future directions in achieving robust MTFM techniques.

B. Current Challenges and Future Directions on MTFM

In our work, we developed the mathematical, computational and experimental tools necessary to perform traction force measurements on "cell-like" free bodies and demonstrated the feasibility of using elastic *solid bodies* in performing TFM on live cellular aggregates. Recent developments in droplet-based force measurement techniques, pioneered by Campas et. al. paved the way toward measuring forces in the cells' natural environment [9]. With the experimental advantages like the ease of droplet delivery to tissues through microinjections, their robustness inside living organisms and the technique's versatility to be integrated to other technologies for measurements of cell mechanics [49], oil micro-droplets are continuing to provide biophysical techniques to quantify cellular forces in natural geometries. On the other hand, possible improvements over these techniques could involve developing local force sensors that can detect shear, and/or nominal values of the normal tractions applied on the sensor, rather than the anisotropic component of the normal traction field that droplets report when fully enclosed within tissues [9]. Also, microdroplet techniques fall short on capturing fully the natural cell-cell contact surface interactions.

Since the liquid surface cannot sustain shear, these methods not only cannot measure the shear loading, but more importantly they do not promote cells to interact with them through shear coupling, which is unnatural for cell-surface interactions. In the case of droplet-cell contacts, the cells do not experience shear resistance from the droplet surface; therefore, they cannot interact with droplet surfaces as they would with other cells, extra-cellular matrix, or solids that they establish contacts with. Our method is powerful in that, to the best of our knowledge, it is the first technique that provides a natural cell-like interaction surface and geometry for the cell-gel attachment in which the cell can apply both shear and normal forces at the same time, thus, more closely mimicking cell-cell interactions. However, as in all current hydrogel-based traction force microscopy techniques [50][51], calculating a unique boundary loading using elastic solids as force transducers requires knowledge about the pointwise displacement field *inside* the material. In terms of hydrogel microspheres, this requirement necessitates the use of fluorescent markers as material point tracers in otherwise transparent hydrogel bodies. However, the point spread functions of these sub-diffraction fluorescent emitters deteriorate rapidly inside thick specimens or large cellular aggregates due to the highly inhomogeneous scattering and absorption of fluorescence emission through the specimen. This, therefore, limits the use of the fluorescent particle-seeded microspheres in a variety of settings including tissues, tumors, and whole animals.

Since the fluorescent particles are diffraction limited, thus practically zero-dimensional emitters, the centroid detection of their point spread functions which are sub-micron in x-y and on the order of a micron in z is highly prone to distortions from the local optical aberrations. We believe that moving to a surface based shape tracking method could side-

step the deleterious optical effects of the cell layers that lie between the microspheres and the objective, thus greatly improving the technique's overall performance and versatility. For this, first, it would be desirable to average the surface signal over a length scale that is greater than the point spread function dimensions. This means, in order to provide more reliable information, the internal surfaces would need to be larger than ~1-2 microns. In addition, the sample dependent length scale of the local anisotropy imposed by the cells also needs to be considered in choosing the size of the internal surfaces, which can be comparable to the cell size. Therefore, moving to microspheres that are ~2-3 cell diameters (~40μm) which contain smaller microspheres with ~5-10μm diameter can help provide more information about the internal deformation field of the bounding microsphere while tolerating the sample dependent anisotropic distortions in the image space. However, and unfortunately, the elastic deformation field that can give rise to a given *surface shape* is degenerate, thus preventing us from finding a unique loading that generates the observed *boundary surface deformation*, given the initial and final shapes of the elastic body. In order to uniquely determine the internal displacement field inside a deformed body, it is therefore necessary to gather information from additionally created *internal* surfaces. Ideally, one would have multi-colored microspheres that are embedded within and mechanically matched to the bounding multi-inclusion microsphere, as illustrated in Figure 30. This would enable the use of the closed form solution of the spherical harmonics formulation of the problem as given in (6), as the solution assumes homogenous, isotropic elasticity within the enclosing body. Inspection of equation (6) shows that the internal deformation field associated with each degree of surface harmonics decays with an exponent that is

proportional to the degree of the applied surface harmonic; meaning, the deformation from higher degree surface harmonics would decay on shorter length scales than the deformations that correspond to lower degree deformations. This feature of the deformation field effectively weights each degree of deformation field differently, thereby acting as an effective low-pass filter. The internal surfaces closer to the microsphere core would provide information about the slowly decaying modes, whereas for the surfaces that are closer to the bounding outer surface, contribution of all degrees of harmonics to the observed deformation would be similar.

While analytically straightforward, there are significant experimental challenges in constructing a complex multi-inclusion microsphere with embedded multicolor microspherical hydrogels that have the same mechanical properties as the bounding material. The biggest challenge arises from the fact that the hydrogels have a highly porous microstructure on length scales less than approximately 10 nm, which would allow diffusion of free monomers in the gel precursor solution into the existing solid (inclusion) phases. Once present in the solid phase, these monomers could be incorporated into the existing gel through photo-initiated addition polymerization, thereby increasing the overall amount of material polymerized to the hydrogel backbone, and stiffening the inclusions beyond their original post-cure mechanical properties. The inclusions would therefore have different mechanical properties as compared to the enclosing microsphere and the analysis of the internal deformations inside the no-longer-homogenous domain would require knowledge of the mechanical mismatches and finite element modeling approaches to describe the deformations of the composite bodies.

Finite element analysis of the deformed body offers the further possibility of using immiscible liquid droplets as internal deformation reporters, as illustrated in Figure 30, rather than nanoscopic fluorescent particles distributed within the solid phase. In this approach, one would impose incompressibility and slip boundary conditions on the internal boundaries between the liquid inclusions and bounding material and numerically solve for the boundary loading on the enclosing microsphere. This is potentially complicated by the fact that the interfacial energy between two immiscible phases can impact the deformations observed in soft solids [52], [53] and they can be comparable to tissue elasticity [9] or higher. Therefore, if liquid droplets are used as *interfaces*, the interfacial tension must be quantified and accounted for. Alternatively, the immiscible phase can be chosen such that it could be replaced by a solvent exchange. (*e.g*. liquid inclusions of toluene in an aqueous hydrogel phase, that are later exchanged with a solvent such as THF, or acetone, and swollen in water.) Exchanging the immiscible phase with water would further simplify the problem and create mechanically free internal boundaries that are computationally easier to handle. Due to the porosity of the hydrogel, the water that is trapped inside the inclusions would be free to escape the hydrogel under deformations from cellular loading whose timescale can range from minutes up to several hours – thus, creating a mechanically free internal boundary. Such solvent exchange approaches would have to be tested thoroughly to ensure that all cytotoxic reagents (such a toluene) are fully removed prior to introduction to cells or tissues.

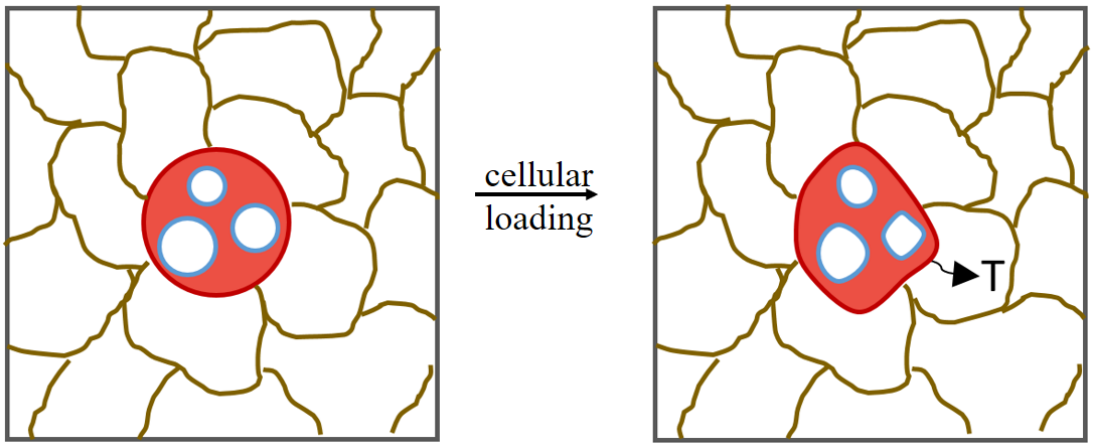

Figure 33. Illustration of multi-inclusion, multi-surfaced microspheres. Internally created surfaces can provide additional deformation information, while being robust to sample dependent optical aberrations. The internal surfaces can be created by solid inclusions, immiscible liquid phases, or aqueous inclusions.

C. Other Relevant Work and the Structure of the Appendices

Development of microsphere traction force microscopy methods has been the focus of the main body of this report. However, during my time in the Valentine Lab, I have worked on other projects and been involved in various collaborations that aimed to study different cellular biophysical phenomena, that naturally led me to pursue an interest in development of MTFM methods. The appendices of this thesis serve as current reports of our efforts in studying these biophysical systems. Some of the work mentioned in the appendices is finalized and some are still in progress, which is indicated in the corresponding sections.

Appendix A is a reprint of our work on *in vitro* rheology studies in chemically-stabilized, entangled and sparsely-crosslinked microtubule networks, in collaboration with Dr. Yali Yang and Dr. Jun Lin, which appeared in Soft Matter in 2012 [54].

Appendix B is a summary of our current progress on the mechanics of non-stabilized microtubule networks, and can be regarded as a continuation of [54] in the sense that we aimed to investigate the effects of microtubule polymerization/depolymerization dynamics on the overall architecture and mechanics of the microtubule networks. This work is still in progress and it is a collaboration with Charlotta Lorenz.

Appendix C is a summary of our studies on investigating the effects of different degrees of mechanical confinement on cell division and cortical dynamics.

Appendix D is a reprint of our work on development of elliptical feature detection algorithms on microscopy images, which appeared on the Journal of Microscopy in 2013 [55].

References

[1] A. J. Engler, S. Sen, H. L. Sweeney, and D. E. Discher, "Matrix Elasticity Directs Stem Cell Lineage Specification," *Cell*, vol. 126, no. 4, pp. 677–689, 2006.

[2] A. Elosegui-Artola, R. Oria, Y. Chen, A. Kosmalska, C. Pérez-González, N. Castro, C. Zhu, X. Trepat, and P. Roca-Cusachs, "Mechanical regulation of a molecular clutch defines force transmission and transduction in response to matrix rigidity.," *Nat. Cell Biol.*, vol. 18, no. 5, pp. 540–548, 2016.

[3] H. E. Balcioglu, H. van Hoorn, D. M. Donato, T. Schmidt, and E. H. J. Danen, "The integrin expression profile modulates orientation and dynamics of force transmission at cell-matrix adhesions.," *J. Cell Sci.*, vol. 128, no. 7, pp. 1316–26, 2015.

[4] W. J. Polacheck and C. S. Chen, "Measuring cell-generated forces: a guide to the available tools," *Nat. Methods*, vol. 13, no. 5, pp. 415–423, 2016.

[5] E. Bazellières, V. Conte, A. Elosegui-Artola, X. Serra-Picamal, M. Bintanel-Morcillo, P. Roca-Cusachs, J. J. Muñoz, M. Sales-Pardo, R. Guimerà, and X. Trepat, "Control of cell-cell forces and collective cell dynamics by the intercellular adhesome.," *Nat. Cell Biol.*, vol. 17, no. 4, pp. 409–420, 2015.

[6] J. L. Tan, J. Tien, D. M. Pirone, D. S. Gray, K. Bhadriraju, and C. S. Chen, "Cells lying on a bed of microneedles: an approach to isolate mechanical force.," *Proc. Natl. Acad. Sci. U. S. A.*, vol. 100, no. 4, pp. 1484–9, 2003.

[7] I. Schoen, W. Hu, E. Klotzsch, and V. Vogel, “Probing cellular traction forces by micropillar arrays: Contribution of substrate warping to pillar deflection,” *Nano Lett.*, vol. 10, no. 5, pp. 1823–1830, 2010.

[8] W. R. Legant, J. S. Miller, B. L. Blakely, D. M. Cohen, G. M. Genin, and C. S. Chen, “Measurement of mechanical tractions exerted by cells in three-dimensional matrices.,” *Nat. Methods*, vol. 7, no. 12, pp. 969–971, 2010.

[9] O. Campàs, T. Mammoto, S. Hasso, R. a Sperling, D. O’Connell, A. G. Bischof, R. Maas, D. a Weitz, L. Mahadevan, and D. E. Ingber, “Quantifying cell-generated mechanical forces within living embryonic tissues. SI,” *Nat. Methods*, vol. 11, no. 2, pp. 183–9, 2014.

[10] M. E. Dolega, M. Delarue, F. Ingremeau, J. Prost, A. Delon, and G. Cappello, “Cell-like pressure sensors reveal increase of mechanical stress towards the core of multicellular spheroids under compression,” *Nat. Commun.*, vol. 8, no. May 2016, p. 14056, 2017.

[11] A. I. Lur’e, *Three-dimensional problems of the theory of elasticity*. London: Interscience Publishers, 1964.

[12] H. R. Sadraie, S. L. Crouch, and S. G. Mogilevskaya, “A boundary spectral method for elastostatic problems with multiple spherical cavities and inclusions,” *Eng. Anal. Bound. Elem.*, vol. 31, no. 5, pp. 425–442, 2007.

[13] A. Constaninescu and A. Korsunsky, *Elasticity with Mathematica*, 1st ed. New York: Cambridge University Press, 2007.

[14] P. C. Hansen, “The L-curve and its use in the numerical treatment of inverse problems,” in *Computational Inverse Problems in Electrocardiology*, vol. 2, 2001, pp. 119–142.

[15] P. C. Hansen, “Regularization Tools version 4.0 for Matlab 7.3,” *Numer. Algorithms*, vol. 46, no. 2, pp. 189–194, 2007.

[16] G. Taubin, “Curve and surface smoothing without shrinkage,” *Proceedings of IEEE International Conference on Computer Vision*. pp. 852–857.

[17] A. Jennings, J. Black, C. Allen, T. H. Pace, and A. T. Trinh, “Empirically Based Modeling of Tape Spring Hinge Deployment for Space Structures,” no. September, pp. 1–17, 2011.

[18] J. L. Hill-West, S. M. Chowdhury, A. S. Sawhney, C. P. Pathak, R. C. Dunn, and J. A. Hubbell, “Prevention of postoperative adhesions in the rat by in situ photopolymerization of bioresorbable hydrogel barriers.,” *Obstetrics and gynecology*, vol. 83, no. 1. pp. 59–64, 1994.

[19] J. L. West and J. A. Hubbell, “Polymeric biomaterials with degradation sites for proteases involved in cell migration,” *Macromolecules*, vol. 32, no. 1, pp. 241–244, 1999.

[20] M. P. Lutolf, J. L. Lauer-Fields, H. G. Schmoekel, A. T. Metters, F. E. Weber, G. B. Fields, and J. A. Hubbell, "Synthetic matrix metalloproteinase-sensitive hydrogels for the conduction of tissue regeneration: Engineering cell-invasion characteristics," *Proc. Natl. Acad. Sci.*, vol. 100, no. 9, pp. 5413–5418, 2003.

[21] D. S. W. Benoit, M. P. Schwartz, A. R. Durney, and K. S. Anseth, "Small functional groups for controlled differentiation of hydrogel-encapsulated human mesenchymal stem cells," *Nat. Mater.*, vol. 7, no. 10, pp. 816–823, 2008.

[22] C. A. Durst, M. P. Cuchiara, E. G. Mansfield, J. L. West, and K. J. Grande-Allen, "Flexural characterization of cell encapsulated PEGDA hydrogels with applications for tissue engineered heart valves," *Acta Biomater.*, vol. 7, no. 6, pp. 2467–2476, 2011.

[23] M. P. Cuchiara, A. C. B. Allen, T. M. Chen, J. S. Miller, and J. L. West, "Multilayer microfluidic PEGDA hydrogels," *Biomaterials*, vol. 31, no. 21, pp. 5491–5497, 2010.

[24] J. S. Temenoff, K. A. Athanasiou, R. G. Lebaron, and A. G. Mikos, "Effect of poly (ethylene glycol) molecular weight on tensile and swelling properties of oligo (poly (ethylene glycol) fumarate) hydrogels for cartilage tissue engineering," 2001.

[25] C. A. DeForest and D. A. Tirrell, "A photoreversible protein-patterning approach for guiding stem cell fate in three-dimensional gels," *Nat. Mater.*, vol. 14, no. 5, pp. 523–531, 2015.

[26] C. A. DeForest and K. S. Anseth, “Photoreversible patterning of biomolecules within click-based hydrogels,” *Angew. Chemie - Int. Ed.*, vol. 51, no. 8, pp. 1816–1819, 2012.

[27] J. S. Miller, C. J. Shen, W. R. Legant, J. D. Baranski, B. L. Blakely, and C. S. Chen, “Bioactive hydrogels made from step-growth derived PEG-peptide macromers,” *Biomaterials*, vol. 31, no. 13, pp. 3736–3743, 2010.

[28] S. Xu, Z. Nie, M. Seo, P. Lewis, E. Kumacheva, H. A. Stone, P. Garstecki, D. B. Weibel, I. Gitlin, and G. M. Whitesides, “Generation of monodisperse particles by using microfluidics: Control over size, shape, and composition,” *Angew. Chemie - Int. Ed.*, vol. 44, no. 5, pp. 724–728, 2005.

[29] R. M. Olabisi, Z. W. Lazard, C. L. Franco, M. A. Hall, S. K. Kwon, E. M. Sevick-Muraca, J. A. Hipp, A. R. Davis, E. A. Olmsted-Davis, and J. L. West, “Hydrogel Microsphere Encapsulation of a Cell-Based Gene Therapy System Increases Cell Survival of Injected Cells, Transgene Expression, and Bone Volume in a Model of Heterotopic Ossification,” *Tissue Eng. Part A*, vol. 16, no. 12, pp. 3727–3736, 2010.

[30] B. D. Fairbanks, M. P. Schwartz, C. N. Bowman, and K. S. Anseth, “Biomaterials Photoinitiated polymerization of PEG-diacrylate with lithium phenyl-2 , 4 , 6-trimethylbenzoylphosphinate : polymerization rate and cytocompatibility,” *Biomaterials*, vol. 30, no. 35, pp. 6702–6707, 2009.

[31] S. Monnier, M. Delarue, B. Brunel, M. E. Dolega, A. Delon, and G. Cappello, “Effect of an osmotic stress on multicellular aggregates,” *Methods*, vol. 94, pp. 114–119, 2016.

[32] C. Bonnet-Gonnet, L. Belloni, and B. Cabane, “Osmotic Pressure of Latex Dispersions,” *Langmuir*, vol. 10, no. 11, pp. 4012–4021, 1994.

[33] M. B. Mellott, K. Searcy, and M. V. Pishko, “Release of protein from highly cross-linked hydrogels of poly(ethylene glycol) diacrylate fabricated by UV polymerization,” *Biomaterials*, vol. 22, no. 9, pp. 929–941, 2001.

[34] A. G. Lee, C. P. Arena, D. J. Beebe, and S. P. Palecek, “Development of macroporous poly(ethylene glycol) hydrogel arrays within microfluidic channels,” *Biomacromolecules*, vol. 11, no. 12, pp. 3316–3324, 2010.

[35] J. K. Armstrong, R. B. Wenby, H. J. Meiselman, and T. C. Fisher, “The Hydrodynamic Radii of Macromolecules and Their Effect on Red Blood Cell Aggregation,” *Biophys. J.*, vol. 87, no. 6, pp. 4259–4270, 2004.

[36] B. Sabass, M. L. Gardel, C. M. Waterman, and U. S. Schwarz, “High Resolution Traction Force Microscopy Based on Experimental and Computational Advances,” *Biophys. J.*, vol. 94, no. 1, pp. 207–220, 2008.

[37] J. Toyjanova, E. Bar-Kochba, C. López-Fagundo, J. Reichner, D. Hoffman-Kim, and C. Franck, “High resolution, large deformation 3D traction force microscopy,” *PLoS*

One, vol. 9, no. 4, pp. 1–12, 2014.

[38] N. D. Gallant, J. R. Capadona, A. B. Frazier, D. M. Collard, and A. J. García, "Micropatterned surfaces to engineer focal adhesions for analysis of cell adhesion strengthening," *Langmuir*, vol. 18, no. 14, pp. 5579–5584, 2002.

[39] C. A. Lemmon, C. S. Chen, and L. H. Romer, "Cell traction forces direct fibronectin matrix assembly," *Biophys. J.*, vol. 96, no. 2, pp. 729–738, 2009.

[40] J. D. Humphries, P. Wang, C. Streuli, B. Geiger, M. J. Humphries, and C. Ballestrem, "Vinculin controls focal adhesion formation by direct interactions with talin and actin," *J. Cell Biol.*, vol. 179, no. 5, pp. 1043–1057, 2007.

[41] G. C. Nanotubes, S. Ryoo, Y. Kim, M. Kim, and D. Min, "Behaviors of NIH-3T3 Fibroblasts on," vol. 4, no. 11, pp. 6587–6598, 2010.

[42] S. R. Coyer, A. Singh, D. W. Dumbauld, D. A. Calderwood, S. W. Craig, E. Delamarche, and A. J. García, "Nanopatterning reveals an ECM area threshold for focal adhesion assembly and force transmission that is regulated by integrin activation and cytoskeleton tension.," *J. Cell Sci.*, vol. 125, no. Pt 21, pp. 5110–23, 2012.

[43] D. W. Dumbauld, H. Shin, N. D. Gallant, K. E. Michael, H. Radhakrishna, and A. J. García, "Contractility modulates cell adhesion strengthening through focal adhesion kinase and assembly of vinculin-containing focal adhesions," *J. Cell. Physiol.*, vol. 223, no. 3, pp. 746–756, 2010.

[44] E. B. Malarkey, K. A. Fisher, E. Bekyarova, W. Liu, R. C. Haddon, and V. Parpura, "Conductive single-walled carbon nanotube substrates modulate neuronal growth," *Nano Lett.*, vol. 9, no. 1, pp. 264–268, 2009.

[45] Y. Gao and M. L. Kilfoil, "Accurate detection and complete tracking of large populations of features in three dimensions," *Opt. Express*, vol. 17, pp. 4685–4704, 2009.

[46] J. C. Crocker and D. G. Grier, "Methods of Digital Video Microscopy for Colloidal Studies," *J. Colloid Interface Sci.*, vol. 179, no. 179, pp. 298–310, 1996.

[47] P. Besl and N. McKay, "A Method for Registration of 3-D Shapes," *IEEE Transactions on Pattern Analysis and Machine Intelligence*, vol. 14, no. 2. pp. 239–256, 1992.

[48] K. S. Arun, T. S. Huang, and S. D. Blostein, "Least-Squares Fitting of Two 3-D Point Sets.," *IEEE Trans. Pattern Anal. Mach. Intell.*, vol. 9, no. 5, pp. 698–700, 1987.

[49] F. Serwane, A. Mongera, P. Rowghanian, D. A. Kealhofer, A. A. Lucio, Z. M. Hockenbery, and O. Campàs, "In vivo quantification of spatially varying mechanical properties in developing tissues," *Nat. Methods*, vol. 14, no. 2, pp. 181–186, 2016.

[50] R. W. Style, R. Boltyanskiy, G. K. German, C. Hyland, C. W. MacMinn, A. F. Mertz, L. A. Wilen, Y. Xu, and E. R. Dufresne, "Traction force microscopy in physics and biology," *Soft Matter*, vol. 10, no. 23, p. 4047, 2014.

[51] U. S. Schwarz and J. R. D. Soin??, “Traction force microscopy on soft elastic substrates: A guide to recent computational advances,” *Biochim. Biophys. Acta - Mol. Cell Res.*, vol. 1853, no. 11, pp. 3095–3104, 2015.

[52] R. W. Style, R. Boltyanskiy, B. Allen, K. E. Jensen, H. P. Foote, J. S. Wettlaufer, and E. R. Dufresne, “Stiffening solids with liquid inclusions,” no. December 2014, 2014.

[53] R. W. Style, C. Hyland, R. Boltyanskiy, J. S. Wettlaufer, and E. R. Dufresne, “Surface tension and contact with soft elastic solids,” *Nat. Commun.*, vol. 4, pp. 1–6, 2013.

[54] Y. Yang, J. Lin, B. Kaytanli, O. a. Saleh, and M. T. Valentine, “Direct correlation between creep compliance and deformation in entangled and sparsely crosslinked microtubule networks,” *Soft Matter*, vol. 8, no. 6, p. 1776, 2012.

[55] B. Kaytanli and M. T. Valentine, “Evolute-based Hough transform method for characterization of ellipsoids.,” *J. Microsc.*, vol. 249, no. 3, pp. 159–164, 2013.

Appendix A: In vitro Microtubule Rheology Studies in Stabilized Entangled Networks (in Collaboration with Y. Yang and J. Lin)

Journal Article:

Direct correlation between creep compliance and deformation in entangled and sparsely crosslinked microtubule networks[3]

Authors: Yali Yang, Jun Lin, Bugra Kaytanli, Omar A. Saleh, and Megan T. Valentine

DOI: 10.1039/b000000x

The microtubule cytoskeleton is essential in maintaining the shape, strength and organization of cells and its misregulation has been implicated in neurological disorders and cancers. To better understand the structure-mechanics relationships in microtubule networks, we measure the time- and force-dependent viscoelastic responses of entangled and sparsely crosslinked microtubule networks to precise microscale manipulation. We use magnetic tweezers devices to apply calibrated step stresses and measure the resultant strain as a function of time. At short times the material behaves as an elastic solid. The linear regime is large, with gentle stiffening observed in entangled networks above ~70% strains. Crosslinked networks are stiffer, and show an extended linear regime. At longer times, we find a creeping regime, suggesting that structural rearrangements of the network dominate the mechanical response. To understand the molecular origins of this behaviour, we use a newly-developed portable magnetic tweezers device to observe the network morphology

[3] Reprinted with Permission from Royal Society of Chemistry.

using a confocal microscope while simultaneously applying point-like stresses to embedded magnetic particles. We observe substantial network compression in front of the bead with no evidence of long-length scale filament flow, and find that the spatial extent of the deformation field depends sensitively on network architecture and connectivity. Our results are important to understanding the role of the cytoskeleton in regulating cargo transport in vivo, as well as the basic physics of non-affine deformations in rigid rod polymer networks.

Introduction

The microtubule (MT) cytoskeleton is a complex biopolymer network found ubiquitously in eukaryotes. MTs play important roles in cell division, where they move chromosomes and localize the cleavage furrow, and in intracellular transport where they form the tracks upon which the transport of secretory/synaptic vesicles, organelles, and other cargo occurs [1]. There is increasing evidence that the spatiotemporal organization of the MT cytoskeleton is essential for numerous other biological processes, ranging from axonal branching and neural pathfinding [2, 3], to the flow of actin in motile and developing cells [4, 5], to the regulation of protein synthesis6. For many of these processes, mechanical stress within the MT cytoskeleton is an important signaling mechanism: for example, tension promotes MT outgrowth at focal adhesion sites [7], regulates MT turnover and organization8, and silences spindle assembly checkpoints to enable cell cycle control9.

In contrast to many biological polymers, mechanical measurements of isolated MTs have shown them to be extremely stiff. MTs are long hollow cylinders with an average contour length of order ~10 μm, large outer diameter of ~25 nm, and persistence length of ~1000μm [10, 11]. Because of this, MT networks lack the entropic contributions of elasticity that

dominate the mechanical response of most polymer gels, and are ideal model systems for athermal, rigid rod polymer materials. A limited number of prior studies have investigated the rheological properties of entangled or crosslinked networks of MTs [12-15]. The most comprehensive study investigated networks of fairly short MTs (characteristic length < 3 μm) under uniform shear conditions. These were found to be soft elastic solids that softened above strains of ~10% and showed evidence of transient attractive filament-filament interactions that enhanced elasticity and suppressed reptation-induced terminal relaxation [13].

In the current work, we explore the microscale mechanical response of networks of longer MTs (average length ~23 μm) subjected to highly localized forces applied using a magnetic tweezers device. This generates a non-uniform deformation field, with a characteristic bending radius dictated by the size of the embedded magnetic particles (~5 μm) [16]. In this regime, filament bending dominates over stretching or compression, thus the physical origins of elasticity, dissipation, and nonlinearity differ from that of networks in which all deformations are affine. Thus, mean-field models that require uniform stretching or bending of filaments no longer apply, limiting the use of traditional continuum mechanics approaches for modeling [17]. This motivates the development and use of new characterization tools that enable direct measurement of structure-property relationships. Here, we show that upon sudden application of force, entangled MT networks are predominantly solids, with modest time-dependent network reorganization occurring at longer times. To understand the molecular origins of this behaviour, we observe the three-dimensional MT network morphology using a confocal microscope, while simultaneously

applying localized stresses to embedded magnetic particles. We find that the network is substantially compressed in front of the bead, and observe no obvious long-length scale flow of material, suggesting that subtle reorganization of entanglements dominate the creep response. These results have important implications for understanding the mechanical properties of the cytoskeleton, in which rigid networks of MTs and actin bundles are locally deformed by transport of intracellular cargos, as well as large-scale structural changes in cell division, motility and morphogenesis. Importantly, we find that the spatial extent of the deformation field can be modulated by inclusion of a small number of rigid crosslinkers. This suggests that even sparse connections between filaments can play an essential role in regulating cell mechanics.

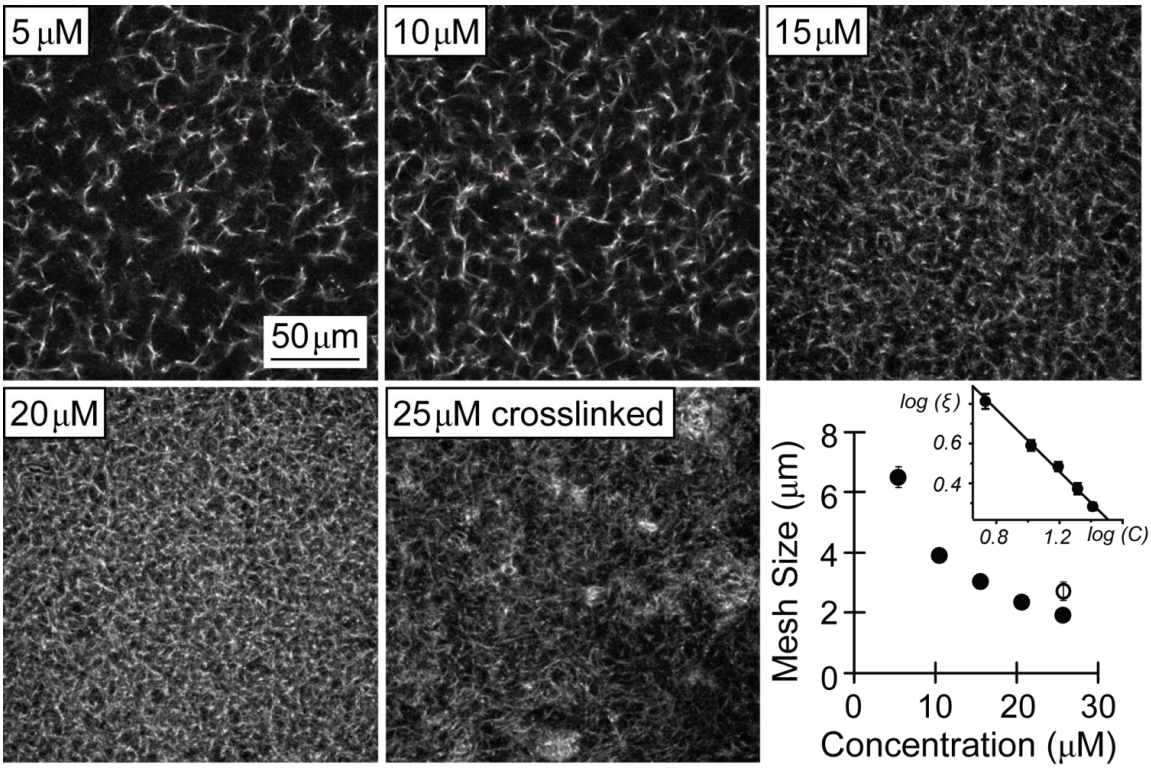

Figure 1: Representative images of entangled and crosslinked MT networks obtained using fluorescence confocal microscopy. Under our polymerization conditions, the entangled MT networks are isotropic and homogeneous. Mesh size is found to decrease monotonically with increasing tubulin concentration (solid symbols). Upon addition of crosslinkers, networks appear to be more structurally heterogeneous, and the average mesh size increases slightly (open symbol). Inset: Data plotted on a log-log plot, and fit to a power law $\xi \sim c^{\alpha}$ fit shown in solid line) where α is found to be 0.76 ± 0.02.

Results

Microstructural properties of entangled and crosslinked microtubule networks

One challenge in determining structure-mechanics relationships in soft biopolymer materials is the difficulty in generating homogeneous materials that can be imaged and mechanically manipulated without damage. To address this, we have developed a robust polymerization method that allows small volumes of MT networks to be generated in a chamber amenable to both fluorescence confocal imaging and manipulation by magnetic tweezers. We load ice-cold solutions of globular tubulin dimers into small capillary tubes in the presence of GTP (required for the enzymatic addition of tubulin) and taxol (a small molecule that promotes MT assembly), then seal and incubate the tubes at ~35℃ for ~1 hour to induce polymerization. For mechanical measurements, magnetic and latex beads are added to the solutions prior to loading and samples are rotated to prevent bead settling during the polymerization reaction. This protocol reliably produces MTs with mean filament length of ~23 μm. Although the MT length distribution is fairly broad, it is nearly independent of tubulin density, with good agreement observed even for the tails of the

distribution that represent the longest filaments (Fig S1). This reproducibility is critical, since even a small number of long filaments can have a disproportionately strong effect, particularly in the non-affine deformation regime18. By developing a protocol that results in a robust and concentration-independent length distribution, we can easily isolate effects due to MT density from effects due to changes in polymer length. Moreover, the long average length ensures that filaments are able to form multiple connections with neighbouring filaments, and thus generate fully entangled gels.

Representative images of entangled MT networks, with concentrations ranging from 5 μM to 20 μM are shown in Figure 1. For each condition, images are thresholded to generate a binary map of 'bright' pixels on a dark background. The spatial distribution of distances between nearest neighbour bright pixels is determined. The decay length of this exponential distribution gives the characteristic network mesh size, ξ [19, 20]. We find to decrease monotonically with increasing tubulin concentration, with $\xi \sim c^{3/4}$ (Fig. 1). This scaling relationship is surprising, as it is generally expected that mesh size will scale with the square root of concentration, due to geometric arguments for filament crossing [21]. Although we do not understand the physical origins of this difference, our results are very reproducible, and we have not found any other experimental demonstration of mesh size scaling for MT networks that contradict this result. Upon crosslinking (using streptavidin and biotinylated tubulin), networks appear more heterogeneous, with the formation of tubulin-dense and tubulin-poor regions throughout the sample, and the characteristic mesh size increases slightly.

Local mechanical perturbations are used to probe microscale viscoelastic properties of MT networks

To determine the microscale viscoelastic properties of entangled MT gels, we polymerize the networks in the presence of small magnetic particles, then apply controlled loads varying from 0–35 pN using a magnetic tweezers device (representative data trace is shown in Fig. S2) [22]. The magnetic field is supplied by a pair of permanent magnets whose position is varied to control the magnetic force at the sample plane. We choose to examine three tubulin concentrations: 18 μM, 26 μM, and 51 μM. We use magnetic particles with diameter of 4.5 μm, which is larger than the mesh size in each case to ensure that the particles are fully engaged with the meshwork and their displacement can be interpreted in terms of local network mechanical response. It is difficult to measure the mechanical properties of gels formed with lower tubulin concentrations because 4.5-μm beads tend to slip through the mesh, and the fragile networks do not easily support the weight of larger beads. Gels are observed via fluorescence confocal microscopy prior to each mechanical measurement to ensure that network quality is maintained from day to day. We measure particle displacement as a function of applied force, as previously described [22, 23].

A typical creep response is shown schematically in Figure 2. When the force F is stepped up by the rapid motion of the magnets toward the sample, the bead position instantaneously jumps a distance d_1, indicating a short-time elastic response. The bead displacement then slowly increases, indicating a long-time creep regime with average velocity v. The crossover time from the elastic regime to the creep regime is given by the time constant τ. After a time T, which is typically 50-75 seconds, the force is abruptly

stepped down to zero by rapid retraction of the magnets, and the bead position rapidly jumps back a distance d_2 to a final position given by Δx_f. After waiting a time that is typically comparable to T, another force pulse is applied. In order to maintain network quality, we complete all mechanical measurements within a few hours of forming the gels, and thus use the minimum waiting time that gives us reproducible results in order to maximize the throughput of our data collection. We have doubled both T and the waiting time between pulses and found no obvious effect on measured mechanical parameters.

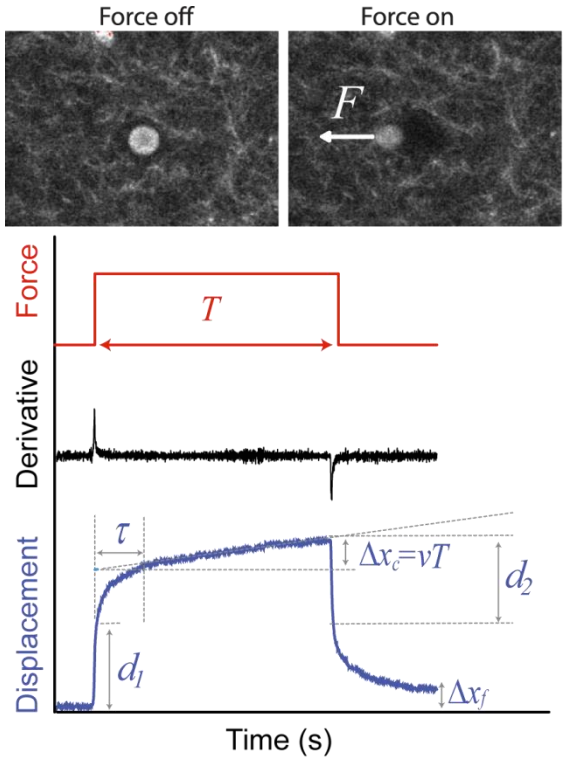

Figure 2: Schematic of typical creep response curve. The upper panel shows two representative images of a 4.5 μm diameter magnetic bead embedded in an entangled MT network at zero force (left) and $F \approx 10$ pN obtained with our newly-developed portable magnetic tweezers device. The lower panel shows a typical creep response curve. Bead

displacement x (blue line) and the force pulse F (red line) are plotted as a function of time t. At short times, the bead responds elastically, followed by a relaxation into a creeping regime. To identify the onset of relaxation, we calculate the derivative of x(t)-vt (black line), which exhibits a maximum at the transition from elastic to creep regime. The typical range of applied forces is 1-30 pN, which induces micron-scale bead displacements.

To understand the molecular origins of network viscoelasticity and gain insight into the structure-mechanics relationships of these gels, we use a newly-developed portable magnetic tweezers device [24], which allows imaging of fluorescently-labelled MT networks using confocal microscopy while simultaneously applying controlled loads. As shown in the upper panel of Figure 2 and discussed in detail below, we find substantial compression of the MT network in front of the bead, and a rarefied network behind. We do not observe flow of polymeric material nor do we find any evidence of shear alignment of filaments near the particle, even under fairly high forces (>20 pN). We tested for effects of loading history by repeatedly applying the same force or by ramping the force up and then back down as a function of time, and in both cases we find a negligible effect on measured mechanical properties.

Additionally, we do not find evidence of nonspecific binding of microtubules to the magnetic beads: the network density at the bead surface is not enhanced before the force is applied, as we would expect if the bead was acting as a local nucleator or crosslinking site, and no filaments appear to remain attached at the rear of the bead when force is applied. We do occasionally observe abrupt motions of beads as they escape from the local cage of MTs that form the meshwork at the sphere surface, particularly at low polymer density or high

force. When identified, these abrupt slip events are excluded from analysis in order to isolate predominantly mechanical interactions from those dominated by local microstructure.

Figure 3: Entangled MT stiffness, given by F/d_1 as a function of (A) force and (B) strain, d_1/ξ. At low forces or strains network stiffness is roughly constant, while mild stiffening is observed for F above ~ 15 pN or strains greater than ~ 70% (dotted line).

Entangled MT networks are mechanically elastic on short time scales

Network stiffness can be estimated by dividing the applied force F by instantaneous bead displacement d_1, as shown in Figure 3. We choose to present the localized elastic response in terms of gel stiffness, to distinguish the microscale mechanical response, which likely depends on the geometry of the network-probe interface, from the scale-invariant continuum elastic modulus. At small forces, the stiffness is nearly constant indicating an approximately linear elastic response (Fig. 3A). For forces greater than ~15 pN, gentle stress stiffening is observed for each tubulin concentration. This gentle transition is clearer when stiffness is plotted as a function of strain, which we approximate by dividing the jump distance d_1 by the network mesh size ξ that we determined via confocal microscopy. In this case, we see stiffening above strains of ~ 70% (as indicated by the dotted line in Fig. 3B). We find that the maximal force we can reliably apply to the network increases monotonically with tubulin concentration. At larger forces, beads tend to escape from the local cage of MTs that form the meshwork at the sphere surface, preventing measurement of gel properties.

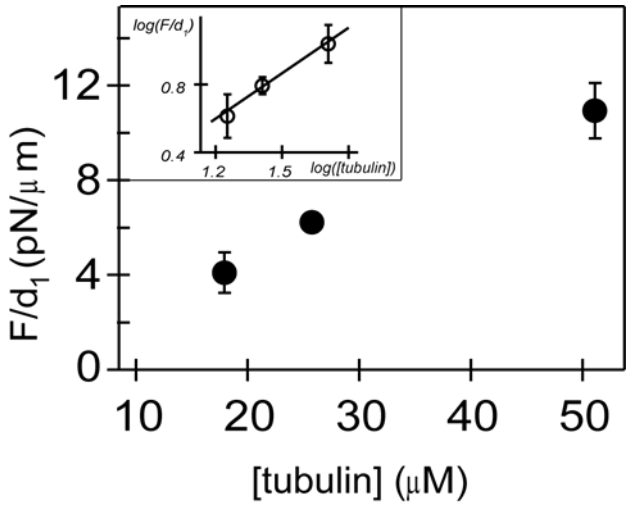

Figure 4: MT stiffness depends linearly on tubulin concentration. This indicates that the elastic response is dominated by mechanical, rather than entropic, stretching of polymer filaments. Inset: Data plotted on a log-log plot, and fit to a power law $F/d_1 \sim [\text{tubulin}]^{\alpha}$ (fit shown in solid line). α is found to be 1.0 ± 0.3.

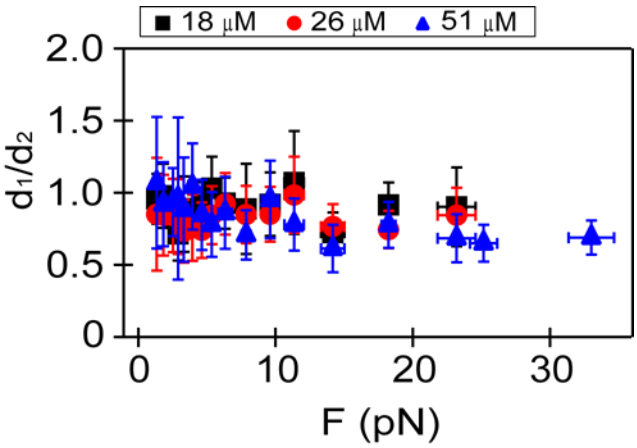

Figure 5: Particle position before and after force step. (A) The ratio of d_1/d_2 is plotted as a function of force for each entangled MT network. At the lowest forces, this ratio is approximately equal to 1, consistent with a linear elastic regime. For force above the critical

force for stress stiffening (~15 pN), we find $d_2 > d_1$ with the strongest decrease observed for the densest MT network.

At low forces (and strains) the network shows a force (and strain) independent plateau. In this regime, stiffness increases linearly with tubulin concentration, as shown in Figure 4. This behaviour is consistent with networks of rigid rods, in which each new filament contributes equally to network elasticity, and contrasts that of entropic networks such as those formed from semiflexible entangled actin filaments, where stiffness tends to arise due to the stress-induced straightening of thermally-undulating filaments [25]. This suggests that entangled MT networks are primarily mechanical (enthalpic) networks. Similar trends are observed for the elastic transition in which force is abruptly stepped down to zero, as shown in Figure S3.

Interestingly, we find that for large forces F > 15 pN, the bead jump distances upon application and removal of the force (d_1 and d_2, respectively) are not equal; rather $d_2 > d_1$, with the strongest decrease observed for the densest MT network. This suggests that at large forces, the network is permanently deformed upon application of force, and that the network the bead returns to when force is stepped down to zero is mechanically and structurally different than the original network that enclosed the bead. It is likely that $d_2 > d_1$ because the application of force leads to an asymmetry in polymer concentration at the bead surface. When the force is turned on, the bead engages with and compresses the network in front, whereas when the force is turned off, the bead returns to the original position through a large void.

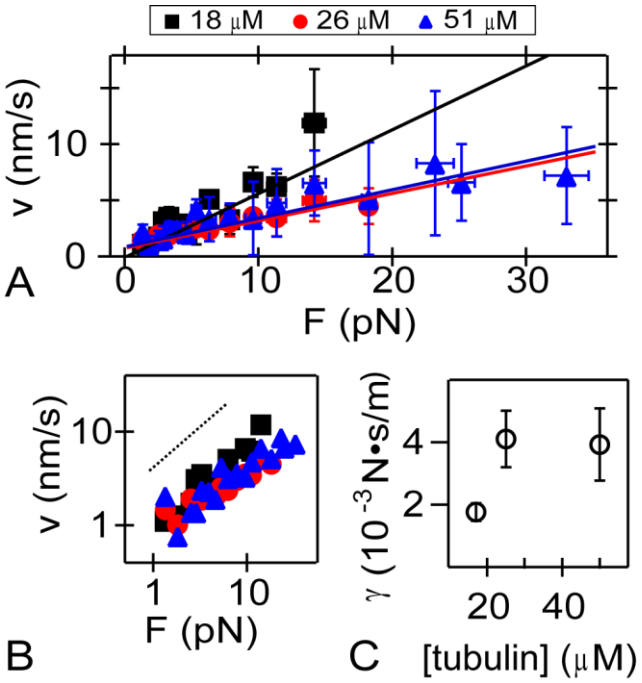

Figure 6: Analysis of creep regime. (A) Creep velocity is plotted as a function of force for three different tubulin concentrations. (B) In each case, velocity increases linearly with force, as demonstrated by plotting the force-velocity data on a log-log plot. Dotted black line shows slope = 1. (C) Through a linear fit of the force-velocity data (panel A, solid line), an effective drag coefficient can be calculated at each tubulin concentration.

On long time scales, entangled MT networks are restructured

After the initial elastic regime, there is a crossover, on a time scale τ of ~ 10 seconds for all conditions studied, to a regime in which bead position increases linearly with time. This creep regime indicates a modest time-dependent rearrangement of the sample that might arise due to filament reorganization, bond breakage, or mechanical slippage of the bead through the network. Creep velocity v increases linearly as a function of force for each tubulin concentration (Fig. 6). Using Stokes' Law $F=\gamma v$, we can determine an effective drag

coefficient γ as a function of tubulin concentration. We find γ to nearly double when the tubulin concentration is increased from 18 μM to 26 μM, but no significant change in γ when the concentration is further increased to 51 μM.

To further investigate the origins of this creep regime, we compare the total distance the bead moves during the creeping phase $\Delta x_c = vT$ to the unrecovered displacement Δx_f (see Fig S4). As expected from our analysis of the creep velocity, Δx_c increases monotonically with applied force. For small forces, $\Delta x_f \approx \Delta x_c$, and both are on the order of ~ 100 nm, much smaller than the bead diameter or ξ, but larger than our estimated tracking error. We suspect this distance is determined by the time-averaged thermal fluctuations of the bead. At larger forces, $\Delta x_f >> \Delta x_c$ due to force-induced slippage of the bead through the porous network. This allows some beads to become trapped in new "pores" when the force is turned off, with higher forces required to induce bead entrapment in denser networks.

Sparse crosslinking enhances elasticity, suppresses strain stiffening, and increases deformation field penetration depth

To examine the effect of crosslinking on MT networks, we generated sparsely crosslinked gels using biotinylated tubulin and streptavidin. For this work, the total tubulin concentration is fixed at 25 μM, 1 in 7 tubulin dimers is biotinylated, and the ratio of biotin moieties to streptavidin is fixed at 10 to 1. This leads to an average distance between crosslinkers of ~ 200 nm. We find the gels are roughly twice as stiff as entangled networks at the same tubulin concentration (Fig. 7A), and find no evidence of stress-stiffening for forces up to ~ 33 pN.

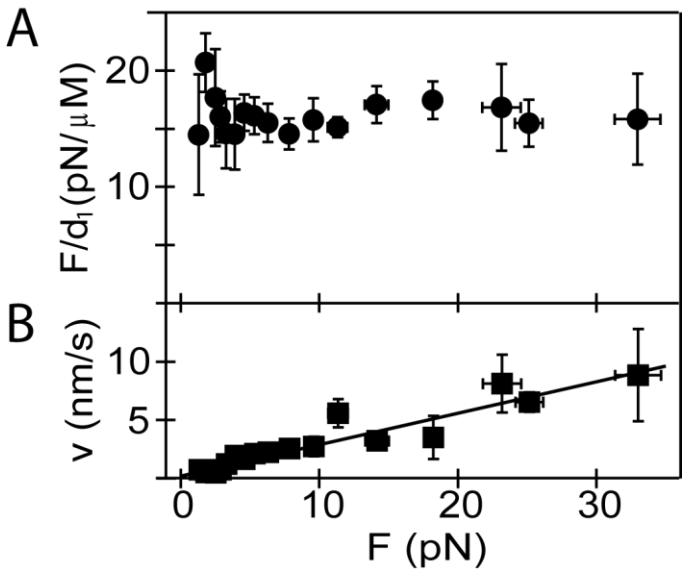

Figure 7: Mechanical response of sparsely crosslinked 25 μM MT networks. (A) MT stiffness is plotted as a function of force. At low force, the stiffness values are roughly twice those measured for a purely entangled network at the same tubulin concentration. In contrast to entangled networks, the linear regime is large, with no evidence of stress-induced stiffening (or softening) for forces as high as ~33 pN. (B) Creep velocity increases as a function of force, and is very similar in magnitude to that measured using purely entangled networks. The effective drag coefficient is $(3.7 \pm 0.4) \times 10^{-3}$ N·s/m.

At this modest crosslinker density, we still observe a creep regime, and find the transition time τ and average flow velocity v to be very similar to the values obtained for the 25 μM entangled gels (Fig. 7B). Consistent with our measurements of entangled networks, we find $d_1 < d_2$, although the ratio of d_1/d_2 is roughly constant as a function of force with a mean value of 0.7 ± 0.1.

At these modest crosslinking densities, the strongest mechanical difference between crosslinked and entangled networks is observed when measuring the extent of penetration of

the deformation field into the MT network. The spatial extent of deformation is measured in two ways: using small non-magnetic latex beads as fiducial markers that can be visualized using transmitted light microscopy or by directly imaging the MT network using fluorescence confocal microscope. In both cases, we employ a portable magnetic tweezers device to enable the precision application of force while collecting high-resolution images. As shown in Figures 8 and S5, the depth of penetration is substantially increased upon crosslinking. The typical penetration distance for an entangled network is a few microns, similar to the size of the magnetic particle that is applying the force. By contrast, in crosslinked networks, the deformation field penetrates for tens of microns. This demonstrates that even subtle changes in network architecture and connectivity can have important consequences on stress transmission in MT gels. Moreover, the deformation field is more uniform in the case of the crosslinked gels, indicating that even modest crosslinking can lead to a non-affine to affine network transition.

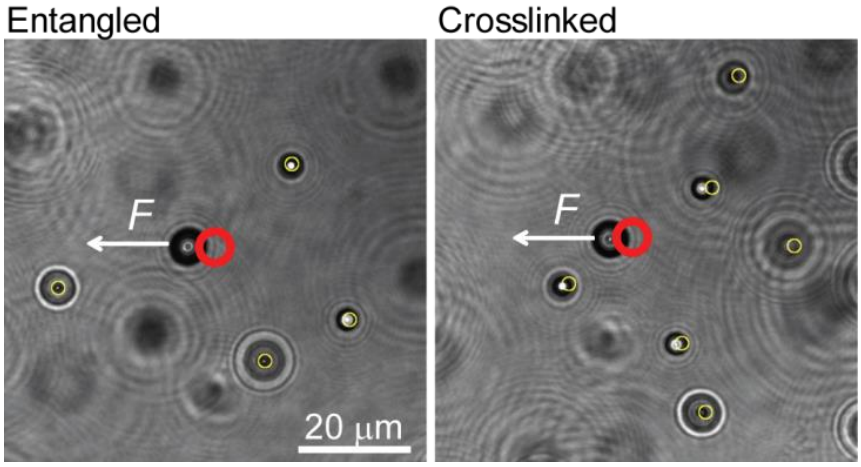

Figure 8: Network crosslinking substantially increases the ability of deformation fields to penetrate deeply into MT networks. Images show the position of magnetic and latex beads

after application of applied force. The original magnetic bead position (with force turned off) is represented by a bold red circle, and original latex bead positions are represented by thin yellow circles for both entangled (left, F = 25 pN) and crosslinked (right, F =30 pN) MT gels. The direction of the force is indicated by the white arrow. The entangled gel shows very little deformation away from the magnetic sphere surface, whereas the crosslinked gel demonstrates long-length scale deformation. In the crosslinked case, latex beads separated by >3 magnetic bead particle diameters move substantially, indicating that long wavelength stress transmission is much more efficient in crosslinked networks.

Discussion

Unlike most biological polymers, we find that MTs form mechanical (enthalpic) networks, whose elasticity arises from bending and stretching of nearly rigid rods. This contrasts the entropic elasticity that dominates the mechanics of individual actin and DNA filaments, and which arises due to the straightening of thermally fluctuating polymers. At low forces, MT networks exhibit a linear elastic response, where network stiffness increases linearly with polymer concentration. At strains > 70%, we observe the onset of stiffening for all entangled gels. Although strain stiffening has been observed for many biopolymer networks, it is usually attributed to an entropic-to-enthalpic transition that occurs when the excess length of the flexible or semi-flexible filaments has been fully extended [26]. In the case of MT networks, this stiffening transition must have a different physical origin. Under our loading conditions, we find that a dense accumulation of filaments builds in front of the particle, and a void volume appears behind. We hypothesize that for large localized forces, this accumulation increases the effective polymer concentration near the bead, leading to a

nonlinear increase in stiffness. The threshold force associated with the onset of stiffening is ~15 pN, a modest force that could easily be applied by a small number (~3-4) of kinesin motors in vivo during cargo transport or mitosis, suggesting this effect may have physiological relevance.

An accumulation of filaments under load was previously reported in magnetic-bead based microrheometry measurements of entangled actin networks [27]. However, in that case there was no evidence of strain stiffening, instead strain softening and force-induced fluidization of the network were observed, suggesting that unlike MT gels, entangled actin networks cannot support large stresses without some form of crosslinking. A number of actin-binding proteins (ABPs) promote the formation of bundles, which can in turn form networks of bundles in vitro and in cells. Although these bundles share some similarities with MTs, ABP-actin networks are extremely complex, and it is difficult to compare their rheology to that of entangled MT gels. For example: ABPs are typically dynamic and compliant and thus can contribute substantially to the network response; composite network rheology depends both on actin concentration and the ratio of actin:ABP; ABPs typically crosslink filaments in addition to bundling them giving rise to complex network architecture and topology; bundle formation can occur through aggregation-controlled growth, which can lead to the formation of frustrated out-of-equilibrium structures; and bundle diameter and length is typically polydisperse (and often unknown) leading to numerous length and time scales for stress relaxation [28-32].

Previous measurements of the rheology of a suspension of very short MTs, with a characteristic length approximately equal to the mesh size, also reported strain softening for

strains above ~10% [13]. This suggests that the stiffening behaviour we observe may require either long MTs that can form truly entangled gels or the application of localized stresses that can lead to the microscale reorganization and densification of the network. Polymer length may be particularly important for rigid rod networks, since the distance between entanglements is much less than the persistence length, allowing a single filament to retain its identity in the network along its entire contour. For each entangled network, we find a transition after ~10 seconds to a creep regime, in which bead position increases slowly, but linearly with time. This transition time is much too long to describe the drainage time for fluid moving through the porous network, and much too short to describe the time for a thermally-driven filament to reptate along its contour [33]. When we image the network directly under load, we do not find any evidence of shear alignment of filaments or bulk flow of polymers on this (or any other) timescale. We therefore suspect that this time-dependent rearrangement arises from the breakage of weak attractive bonds between neighbouring filaments. Our tubulin proteins are purified by multiple cycles of assembly and disassembly, followed by several rounds of phosphocellulose chromatography to remove any non-functional tubulin dimers and microtubule associating proteins (MAPs). Moreover, we find no evidence of MAP contamination using high-resolution gel electrophoresis or Western blotting, and therefore rule out any MAP-based crosslinking. Instead, we suspect that these attractive interactions may arise from salt bridging or divalent crosslinking mediated by the Mg^{2+} ions that are required for coordination of the GTPase activity of tubulin. Attractive interactions have been reported for other rigid rod suspensions, not only of MTs but also of surfactant-stabilized single walled carbon nanotubes, as well as networks

of actin or neurofilaments, two semiflexible polymers [13, 34-38 13, 39]. Identifying the molecular origins of these interactions is a clear future direction for this work.

When a modest number of crosslinks are introduced, we find an increase in gel stiffness and suppression of strain-stiffening, but still observe long-time rearrangement of the sample that is indistinguishable from that of an entangled network at the same polymer density. That suggests that the distance between rigid crosslinks is larger than the distance between physical entanglements. We estimate the average distance between streptavidin proteins to be ~200 nm, and thus conclude that only a fraction of these proteins is actually engaged in crosslinking at any time. Yet, even in this limit of sparse connectivity, we find that crosslinking has a substantial effect on the ability of the deformation field to penetrate the sample. This suggests that long range stress transmission can be controlled by subtle changes in network architecture and connectivity. Moreover, the transition from non-affine to affine network deformation can be controlled by varying crosslinker concentration even under the application of very localized force fields.

Experimental

Proteins: Unlabeled and rhodamine-labeled tubulin proteins are generously provided by Professor Leslie Wilson at University of California, Santa Barbara. Unlabeled tubulin is purified from bovine brain by cycles of assembly and disassembly and followed by phosphocellulose chromatography 40. Rhodamine-labeled tubulin is prepared by reaction with succinimidyl esters of carboxyrhodamine-6G (C-6157; Invitrogen). Commercial biotinylated porcine brain tubulin (T333P; Cytoskeleton, Inc.) with ~1:1 labeling ratio of

biotin to tubulin heterodimer is reconstituted to 10 mg/ml in G-PEM80 buffer (80 mM PIPES, 4 mM MgCl2, 1 mM EGTA and 1 mM GTP; pH = 6.9).

Preparation of MT networks embedded with magnetic beads. Entangled MT networks are formed by combining the following reagents on ice: unlabeled tubulin, rhodamine-labeled tubulin, 1 mM GTP, 1 mM DTT, 10% (v/v) DMSO, taxol and PEM80 (80 mM PIPES, 4 mM $MgCl_2$, 1 mM EGTA; pH = 6.9). Although the total tubulin concentration is varied in this study, in all cases, the molar ratios of rhodamine-labeled tubulin to total tubulin was 1:6, and taxol to total tubulin was 1:2. When making crosslinked MT networks, biotin-labeled tubulin is also included into the ice-cold tubulin mixture with the molar ratio of biotin-labeled to total tubulin of 1:7. In each case, tosyl-activated magnetic beads with diameter of 4.5 μm (Dynabeads, Invitrogen) are added to the ice-cold mixture at final concentration of ~106 beads/mL. To facilitate visualization of the deformation field induced by the motion of the magnetic bead, 2.5-μm latex beads (PS05N; Bangs Laboratories Inc) are sometimes embedded as probing beads at a final concentration of ~$5x10^7$ beads/mL.

The ice-cold tubulin solution is then loaded into small rectangular tubes (0.1 x 1 x 50 mm^3; Friedrich & Dimmock, Inc) by capillary action. Prior to loading, the capillary tubes are cleaned by rinsing with 1M sodium hydroxide, then pre-coated with reference beads to enable the subtraction of artefactual mechanical or thermal drift, or vibration of the sample and/or the stage from the real motion of the embedded magnetic particles. To achieve this, 5.43 μm latex beads (PS06N; Bangs Laboratories, Inc) are diluted in isopropanol to 5×10^5

beads/mL and loaded into the capillary tubes. The tubes are placed at a flat benchtop for 10 minutes to promote sedimentation. The tube is gently dried and the tube is baked at 150℃ for 2 minutes to partially melt the beads onto one side of the capillary tubes. After introduction to the capillary tube, entangled networks are immediately sealed with high vacuum grease, placed in a dry incubator at ~35℃, and incubated for ~1 hour under constant rotation to prevent the magnetic beads (and latex beads, if included) from settling. For crosslinked networks, the tubulin solution is first incubated at 35℃for 3 minutes in a small microcentrifuge tube, then streptavidin is added such that the molar ratio of streptavidin:biotin-labeled tubulin is fixed at 1:10. The solution is well mixed by gently pipetting using a cut-off P20 pipette tip, then immediately loaded into the capillary tube, which is sealed with vacuum grease and incubated at 35℃for ~1 hour under constant rotation, as described above.

Confocal imaging for structure determination. Confocal microscopy images are obtained using an inverted Fluoview 500 laser scanning system (Olympus). Two-dimensional slices of rhodamine-labeled MT networks are imaged using 561 nm laser excitation and a 60× N.A. 1.4 oil-immersion objective, with scan size of 1024 × 1024 pixels^2, scan rate of 9.59 seconds/scan, and magnification of 207.16 nm/pixel.

Image analysis. To quantify the mesh size of the MT networks, image analysis is performed on two-dimensional confocal images [19, 20]. The images are first processed by thresholding. The threshold is chosen to remove as much noise as possible while retaining

the pixels that correspond to the MTs. This is done by comparing intensities of the brightest background pixels to those of the dimmest MT pixels, with the background and MT pixels being differentiated by visual examination. After thresholding, the distance between nearest neighbour MT pixels within each row and column is determined. Our analysis is similar to the radial distribution of distances between filament intersections, but is implemented in Cartesian coordinates to take advantage of the natural axes of the microscope images. The distribution of distances is plotted and fitted to an exponential $P(\xi) = P_0 e^{-r/\xi}$, where r is the distance in microns and ξ is the characteristic mesh size (see Fig S6). Each measurement is averaged over 28-57 images. Based on our pinhole and oil-immersion objective lens, we estimate our z-resolution to be ~1 μm. Using 2D images provides a good approximation of the average 3D mesh size, but underestimates the maximum pore diameter [13].

Conventional magnetic tweezers: Mechanical measurements are performed using a custom-built magnetic tweezers system that enables precise manipulation of magnetic beads along the optical axis (the z-axis) and simultaneous three-dimensional tracking of bead position [23]. Briefly, a simple inverted microscope is constructed using an oil-immersion objective (100×, 1.25 N.A.) that is mounted onto a piezoelectric stage (P-725; Physik Instrumente) to enable nanopositioning of the focal plane. A 650 nm light emitting diode (Roithner Lasertechnik) provides illumination, and a CCD camera (CV-A10 CL; JAI) captures brightfield images at a frame rate of 60 Hz.

The applied magnetic field is generated by a pair of permanent rare-earth Neodymium Iron Boron (NdFeB) magnets (NS-505050; DuraMag) located above the

sample stage, and oriented such that the alignment of their magnetic moments is antiparallel. Variation of the magnetic field (and thus magnetic force) at the sample plane is achieved by vertically translating the magnets with a DC-servo motor (M-126.PD1; Physik Instrumente). Separation distances between the sample plane and magnet may range from 0–24 mm from the sample plane. Forces are calibrated by measuring the Brownian motion of a magnetic bead that is tethered to the coverslip by a single DNA molecule, and thus acts as a simple inverted pendulum41. The lateral spring constant is given by the ratio of the vertical force to the DNA length. This spring constant can be found by modeling the measured bead trajectory with an overdamped Langevin equation of motion for a particle in a harmonic potential, and fitting the measured power spectrum in position to that predicted from the Langevin model after accounting for issues of finite data sampling rate and instrumental low-pass filtering [42]. The best-fit spring constant, along with the measured length, gives an estimate of the force; this calibration is then repeated at each desired magnet position. In this study, the minimum separation used was ~7 mm (corresponding to a force of ~33 pN on a typical 4.5-μm magnetic bead). Real-time tracking of the three-dimensional bead position is achieved using custom image analysis routines written in LABVIEW (National Instruments) 43. In the presence of the MT gels, we achieve a resolution of ~ 10 nm in the x and y directions and ~15–20 nm in the z direction.

Analysis of Magnetic Tweezers Data. Analysis of data traces (as shown schematically in Fig. 2) is performed as follows. We dissect the bead motion into three distinct regimes—a short-time elastic jump, a relaxation transition, and a long-time creep regime. Creep velocity

v is determined from the slope of a linear fit to bead displacement x versus time t for several (typically <10) seconds prior to the retraction of the magnet pair. We then determine the first order derivative of $x(t)$-vt. We define the elastic regime to start when the force is turned on and to end when the first order derivative reaches its maximum. This maximum also defines the beginning of the relaxation regime, which ends when the derivative drops to zero. For practical purposes, we define the end point by the time at which the moving average of the derivative drops below a threshold equal to 0.05% of the maximum value. The moving average is implemented using a Savitzky-Golay smoothing filter (polynomial order 2, 20 point window). The flow regime follows and ends when the force is reduced at time $t = T$. After identifying these regimes, the following parameters are calculated: d1 is the distance the bead travels in the elastic regime and τ is the total time of the relaxation regime. When the magnets are retracted, we identify an elastic recovery regime that starts when the force is turned off and ends when the first order derivative reaches its minimum; d_2 is the distance the bead travels in this second elastic regime. All uncertainties are reported as SEM values.

Portable magnetic tweezers to determine structure-mechanics relationships. A newly-designed, custom-built portable magnetic tweezers device is used to apply calibrated stresses to microtubule networks, while their microscale deformation is simultaneously measured using confocal microscopy [24]. Briefly, two NdFeB rare earth magnets (N45, $0.25\times0.25\times1$ inch^3; Applied Magnets) are mounted onto a two-axis translation stage and positioned near the focus of the objective lens in a manner that protects the imaging quality of the microscope. The distance between the magnets and sample is controllably varied,

leading to application of controlled forces to small magnetic particles at the sample plane. For a typical measurement, the magnets are moved toward the sample until they just touch the coverslip edge, to ensure application of the maximum force (which we call the 'force-on' condition). To reduce this force level, the magnets are moved away from the coverslip surface until the separation distance exceeds ~ 10 mm (which we call the 'force-off' condition). The rate of magnet retreat (and therefore of the rate of force reduction) can be varied through manual control of the translation stage. Forces are calibrated by measuring the velocity at which a free bead moved through a liquid of known viscosity using Stokes Law. At each force condition, the deformation of the microtubule networks and detailed interaction between the magnetic bead and the surrounding microtubule mesh are recorded using confocal microscopy. In this 'sideways-pulling' geometry, beads move perpendicular to the optical axis (the 'x' axis) when the force is on. Images are obtained using both the fluorescence (561 nm laser excitation) and the transmitted light channels using either a 60×, 1.4 N.A. oil-immersion objective lens or a 60×, 1.2 N.A. water-immersion objective lens with coverslip thickness correction collar. A time series of two-dimensional image stacks is collected using a scan size of 512 × 512 pixels^2 at a rate of 1.12 seconds/scan (4× digital zoom, magnification 103.6 nm/pixel).

Conclusions

We use a new experimental approach to measure structure-mechanics relationships in reconstituted MT cytoskeletons. We apply localized forces directly to MT gels in a physiologically-relevant manner using magnetic tweezers devices while observing network deformation using confocal microscopy. At short times, entangled gels are elastic, with

gentle stiffening observed above ~70% strains, which we attribute to a densification of the network in front of the bead. For entangled gels, network deformation is nonaffine, resulting primarily in bending of MTs near the particle surface. Crosslinking leads to a much more uniform deformation field that penetrates over distances of several particle diameters. This indicates that the spatial extent of the deformation field depends sensitively on network architecture and connectivity, and that even sparse crosslinking of networks can have a significant effect on long-range stress transmission.

Acknowledgements

Authors thank A. Levine and R. Shlomovitz for many helpful discussions, and are grateful for the support of a Burroughs Wellcome Fund Career Award at the Scientific Interface (to MTV), a Special Research Award from Santa Barbara Cottage Hospital (to MTV), a Young Investigators Grant from the Human Science Frontiers Program (RGY0078/2007-C to OAS), and a National Institutes of Health/National Center for Research Resources (NIH/NCRR) Shared Instrumentation Grant (1S10RR017753-01).

References

1. N. Hirokawa, Y. Noda, Y. Tanaka and S. Niwa, Nature Review Molecular Cell Biology, 2009, 10, 682-696.

2. K. Kalil and E. W. Dent, Current Opinion in Neurobiology, 2005, 15, 521-526.

3. E. W. Dent and K. Kalil, Journal of Neuroscience, 2001, 21, 9759-9769.

4. O. C. Rodriguez, A. W. Schaefer, C. A. Mandato, P. Forscher, W. M. Bement and C. M. Waterman-Storer, Nature Cell Biology, 2003, 5, 599-609.

5. C. Waterman-Storer, D. Y. Duey, K. L. Weber, J. Keech, R. E. Cheney, E. D. Salmon and W. M. Bement, Journal of Cell Biology, 2000, 150, 361-376.

6. S. Kim and P. A. Coulombe, Nature Reviews Molecular Cell Biology, 2010, 11, 75-81.

7. I. Kaverina, O. Krylyshkina, K. Beningo, K. Anderson, Y.-L. Wang and J. V. Small, Journal of Cell Science, 2002, 115, 2283-2291.

8. A.-M. C. Yvon, D. J. Gross and P. Wadsworth, Proceedings of the National Academy of Sciences of the United States of America, 2001, 98, 8656-8661.

9. A. Musacchio and E. D. Salmon, Nature Reviews Molecular Cell Biology, 2007, 8, 379-393.

10. C. P. Brangwynne, F. C. MacKintosh and D. A. Weitz, Proceedings of the National Academy of Sciences, 2007, 104, 16128-16133.

11. F. Gittes, B. Mickey, J. Nettleton and J. Howard, Journal of Cell Biology, 1993, 120, 923-934.

12. P. A. Janmey, U. Euteneuer, P. Traub and M. Schliwa, The Journal of Cell Biology, 1991, 113, 155-160.

13. Y.-C. Lin, G. H. Koenderink, F. C. MacKintosh and D. A. Weitz, Macromolecules, 2007, 40, 7714-7720.

14. V. Pelletier, N. Gal, P. Fournier and M. L. Kilfoil, Physical Review Letters, 2009, 102, 188303.

15. M. Sato, W. H. Schwartz, S. C. Selden and T. D. Pollard, The Journal of Cell Biology, 1988, 106, 1205-1211.

16. A. C. Maggs, Physical Review E, 1998, 57, 2091.

17. D. A. Head, A. J. Levine and F. C. MacKintosh, Physical Review E, 2005, 72, 061914.

18. M. Bai, A. R. Missel, A. J. Levine and W. S. Klug, Acta Biomaterialia, 2011, 7, 2109-2118.

19. L. J. Kaufman, C. P. Brangwynne, K. E. Kasza, E. Filippidi, V. D. Gordon, T. S. Deisboeck and D. A. Weitz, Biophys. J., 2005, 89, 635-650.

20. Y.-l. Yang and L. J. Kaufman, Biophysical Journal, 2009, 96, 1566-1585.

21. P. G. deGennes, P. Pincus, R. M. Velasco and F. Brochard, Journal of Physics, 1976, 37, 1461-1473.

22. M. Manosas, A. Meglio, M. M. Spiering, F. Ding, S. J. Benkovic, F. X. Barre, O. A. Saleh, J. F. Allemand, D. Bensimon and V. Croquette, Methods of Enzymology, 2010, 475, 297-320.

23. N. Ribeck and O. A. Saleh, Review of Scientific Instruments, 2008, 79, 6.

24. Y. Yang, J. Lin, R. Meschewski, E. Watson and M. T. Valentine, BioTechniques, 2011, 51, 29-34.

25. M. Doi and S. F. Edwards, The theory of polymer dynamics, Oxford University Press, Oxford, 1986.

26. C. Storm, J. J. Pastore, F. C. MacKintosh, T. C. Lubensky and P. A. Janmey, Nature, 2005, 435, 191-194.

27. J. Uhde, W. Feneberg, N. Ter-Oganessian, E. Sackmann and A. Boulbitch, Physical Review Letters, 2005, 94, 198102.

28. M. L. Gardel, J. H. Shin, F. C. MacKintosh, L. Mahadevan, P. Matsudaira and D. A. Weitz, Science, 2004, 304, 1301-1305.

29. K. M. Schmoller, O. Lieleg and A. R. Bausch, Biophysical Journal, 2009, 97, 83-89.

30. K. M. Schmoller, O. Lieleg and A. R. Bausch, Soft Matter, 2008, 4, 2365-2367.

31. O. Lieleg, J. Kayser, G. Brambilla, L. Cipelletti and A. R. Bausch, Nat Mater, 2011, 10, 236-242.

32. K. M. Schmoller, P. Fernandez, R. C. Arevalo, D. L. Blair and A. R. Bausch, Nat Commun, 2010, 1, 134.

33. T. M. Squires and T. G. Mason, Annual Reviews of Fluid Mechanics, 2010, 42, 413-438.

34. N. Y. Yao, C. P. Broedersz, Y. Lin, K. E. Kasza, F. C. MacKintosh and D. A. Weitz, Biophysical Journal, 2010, 98, 2147-2153.

35. G. Z. Sowa, D. S. Cannell, A. J. Liu and E. Reisler, The Journal of Physical Chemistry B, 2006, 110, 22279-22284.

36. J. Tang and P. Janmey, Biol. Bull., 1998, 194, 406-408.

37. C. Semmrich, T. Storz, J. Glaser, R. Merkel, A. R. Bausch and K. Kroy, Proceedings of the National Academy of Sciences, 2007, 104, 20199-20203.

38. Y.-C. Lin, G. H. Koenderink, F. C. MacKintosh and D. A. Weitz, Soft Matter, 2010, 7, 902-906.

39. L. A. Hough, M. F. Islam, P. A. Janmey and A. G. Yodh, Physical Review Letters, 2004, 93, 168102.

40. L. Wilson and J. J. Correia, in Methods in Cell Biology, Vol 95, Elsevier Academic Press Inc, 2010, pp. 2-15.

41. T. R. Strick, J. F. Allemand, D. Bensimon, A. Bensimon and V. Croquette, Science, 1996, 271, 1835-1837.

42. K. Neuman and A. Nagy, Nature Methods, 2008, 5, 491-505.

43. C. Gosse and V. Croquette, Biophys. J., 2002, 82, 3314-3329.

SUPPLEMENTAL MATERIALS

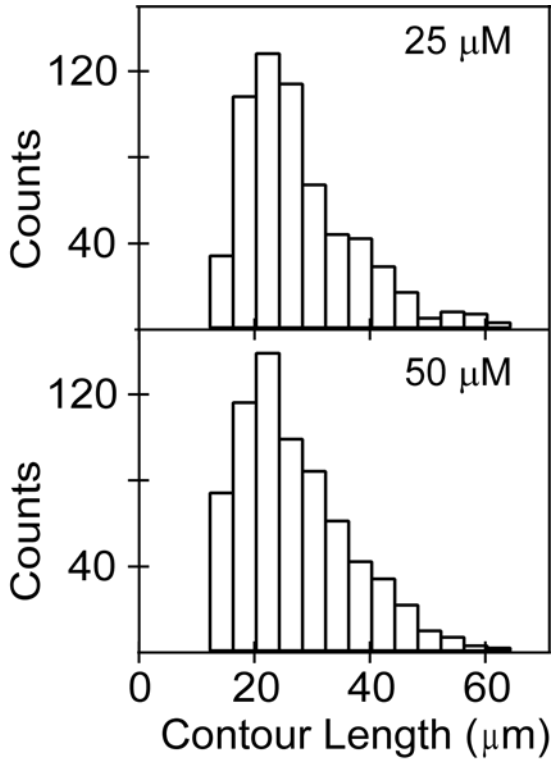

Figure S1: Contour length distribution for MTs is independent of tubulin concentration. The distribution of MT lengths is determined by attaching individual MTs to a coverslip, visualizing them using TIRF microscopy, and measuring their lengths manually using built-in measurement tools in ImageJ. Under the polymerization conditions used for this work, we

find the length distribution to be constant as a function of tubulin concentration. The mean length for 25 µM tubulin is 23.9 ± 0.4 µm (SEM; 623 measurements) and for 50 µM tubulin is 23.3 ± 0.4 µm (SEM; 710 measurements), as shown.

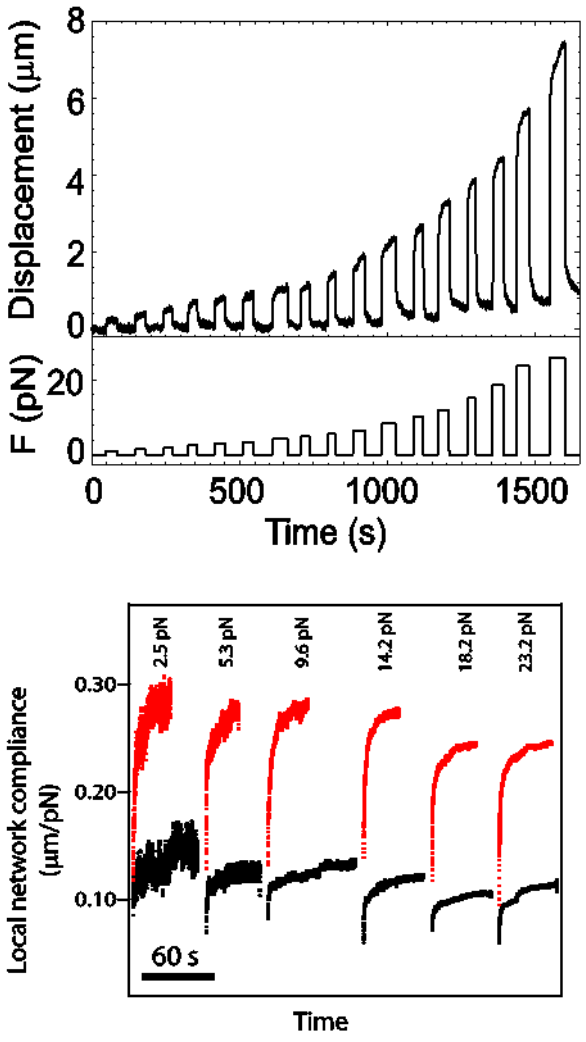

Figure S2: Representative traces showing force-dependent bead displacement as a function of time. (Top) Force is ramped up from ~1–33 pN over the course of the measurement, which typically takes ~20-30 minutes per bead. For small forces the response is typically

elastic: bead position is approximately constant under constant force, and the bead returns to its original position when the force is stepped down to zero. At larger forces, a creep regime is observed, in which the bead position increases linearly with time. When creep is observed, the bead does not fully return to its starting position, due to energy dissipation and interactions with microstructure. (Bottom) The local network compliance can be determined by dividing the bead displacement by the applied force, as shown for a sampling of forces for entangled (red) and crosslinked (black) networks of 26 μM tubulin. Each trace shows the behaviour of a single bead under force. The compliance is roughly constant for the entangled networks for forces below ~ 15 pN, then decreases slightly, as expected for a stress-stiffening gel. The crosslinked networks are less compliant (stiffer) and less force sensitive.

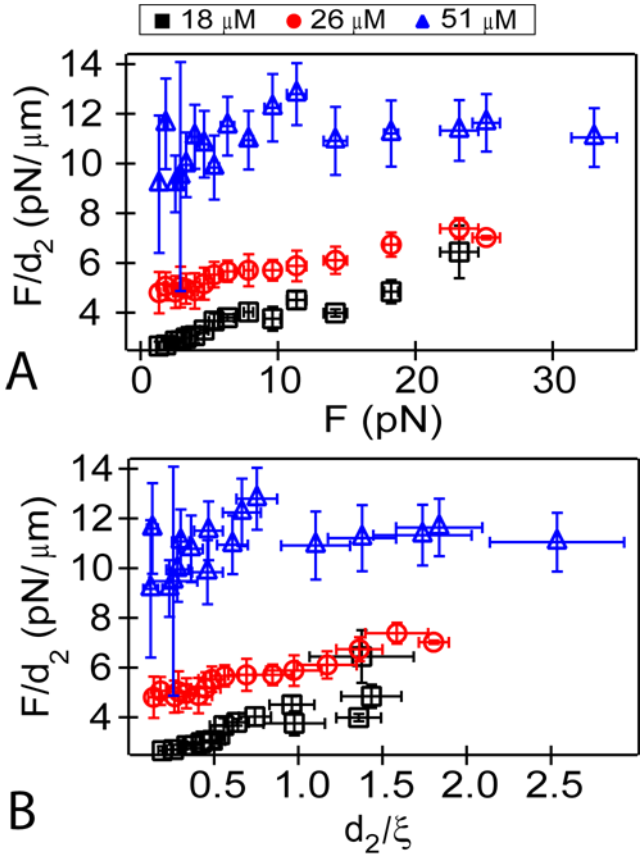

Figure S3: Stiffness of entangled MT networks, given by F/d_2 as a function of (A) force and (B) strain, d_2/ξ Overall, the trends for the force off transition are similar to that of the force on transition (as shown in Figure 3). There is a low force plateau, in which stiffness values increase linearly with tubulin concentration, followed by a stiffening regime at high force (or strain). In detail, the onset of non-linearity differs from that of the force-on transition data, in which all networks stiffen above strains of ~ 70%. For the force-off transition, we find that the 18 μM (□) and 26 μM (○) networks start to stiffen at strains of ~ 30%, whereas the 51 μM (△) network response is linear across the range of forces probed.

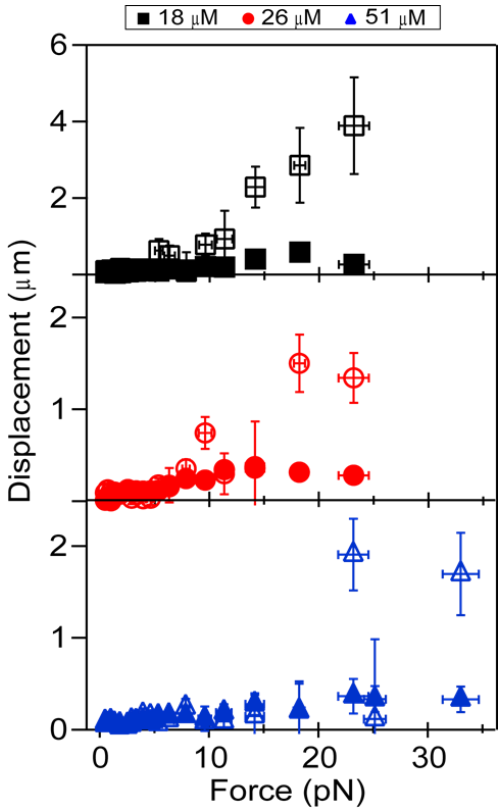

Figure S4: Comparison of the creep displacement Δx_c (solid symbols) to the unrecovered displacement Δx_f (open symbols). As expected from our analysis of the creep velocity, Δx_c increases monotonically with applied force. For small forces, $\Delta x_f \approx \Delta x_c$. At larger forces, $\Delta x_f >> \Delta x_f$ due to force-induced slippage of the bead through the porous network, which allows some beads to become trapped in new "pores" when the force is turned off. This behaviour is observed at all tubulin concentrations; however, higher forces are required to induce bead entrapment in denser networks.

Crosslinked network Entangled network

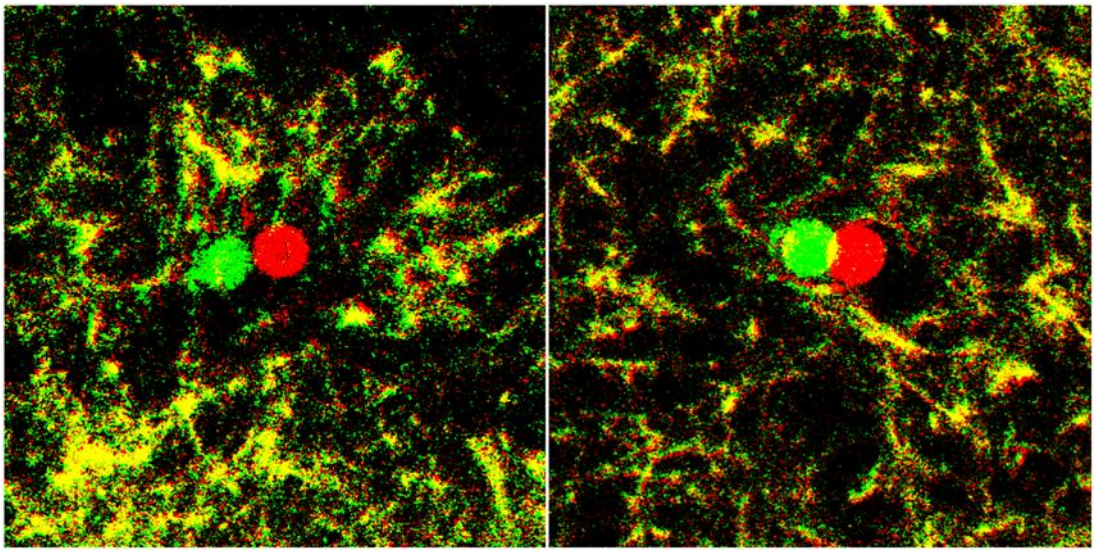

Figure S5: Dual color images of networks showing force-induced network displacement. Here, representative images of weakly crosslinked (right) and entangled (left) 25 mM tubulin networks are shown. Each image is an overlay of an image collected under no force (red) and a second image collected under the application of ~25 pN force, which causes the bead and the entrained network to move toward the left (green). In places where the network is stationary upon application of force, the green and red images overlap and the composite image appears yellow. In the entangled case, the motion of the network is limited to the area just surrounding the bead, and highly bent filaments can be observed. By contrast, in the crosslinked cases, a much larger deformation zone extends for several particle diameters, and the filaments tend to collectively stretch rather than locally bend, indicating a more affine deformation field.

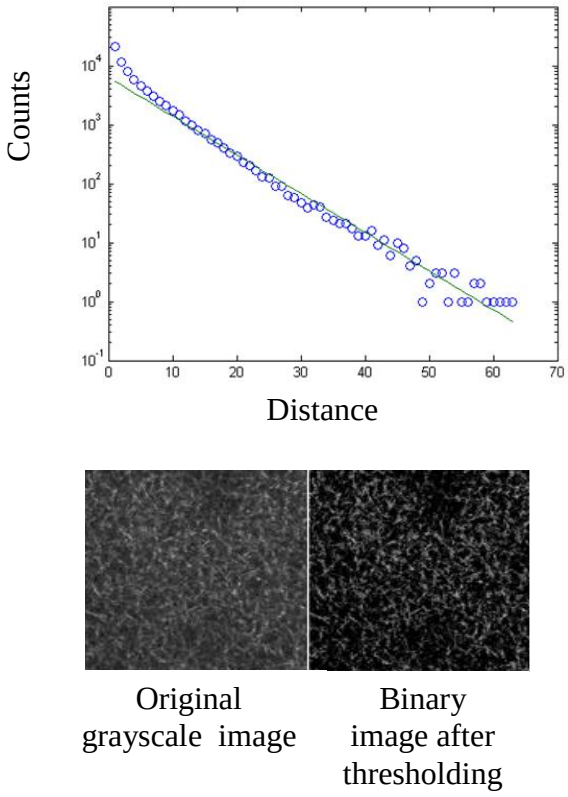

Figure S6: Example of raw data used for mesh size determination. To quantify the mesh size of the MT networks, image analysis is performed on two-dimensional confocal images. After thresholding, the distance between nearest neighbour MT pixels within each row and column of the binary image is determined. Here, two sample images (~ 65 × 65 μm^2 field of view) are shown. This analysis is similar to calculating the radial distribution of distances between filament intersections, but is implemented in Cartesian coordinates to take advantage of the natural axes of the microscope images. The distribution of distances is plotted and fitted to an exponential $P(\xi) = P0e^{-r/\xi}$, where r is the distance between pixels and ξ is the characteristic mesh size. There is a systematic deviation at the smallest displacements due to the limited resolution of the microscope. This method has been used

extensively in characterizing the structural properties of collagen and other extracellular matrix protein networks.

Appendix B: In vitro Microtubule Rheology Studies in Non-stabilized Entangled Networks (in Collaboration with C. Lorenz)

In Appendix A, we discussed the methods we developed to assemble and study the structure-mechanics relationships in microtubule (MT) networks stabilized by taxol (paclitaxel) and DMSO (dimethyl sulfoxide). Here, building on the same experimental protocols and expertise, we aim to study the effects of MT growth and shrinkage dynamics on the overall mechanics of the *in vitro* MT networks. Such dynamics naturally occur in cellular microtubule networks and are essential for chromosome capture and regulation of the lamellar actin cytoskeleton [1-3]. To this end, we developed the methods for performing confocal microscopy imaging and passive microrheology using dynamic MT networks without the addition of chemical stabilizers.

1. Structural Measurements on GMPCPP-stabilized and non-stabilized MT networks

By reducing the filament stability, we increase substantially the concentration of tubulin dimers needed to form a microtubule filament, known as the critical concentration. However, we find that at large concentrations of soluble tubulin dimers it is not only possible to form space-spanning networks of microtubules in the absence of stabilizers, but that the networks have similar overall structural features as compared to chemically stabilized networks, albeit at higher overall tubulin concentration. Figure 1 below shows representative confocal images of networks formed using non-stabilized using 50μM and 60μM free tubulin dimers, and networks stabilized by the non-hydrolyzable GTP analog GMPCPP formed using 17μM and 34μM of free tubulin dimers. Note that all tubulin

concentrations reported here are estimated to have $\pm$ 2μM uncertainty associated with them. The morphology of these two types of networks Figure 1 (a)-(b) and Figure 2 (c)-(d) are similar in terms of average network mesh size, MT length, bundling and polymerized MT number density for the corresponding tubulin concentrations. There is a noticable increase in the fluorescence background of the non-stabilized network, consistent with the increase in free tubulin dimers in this case.

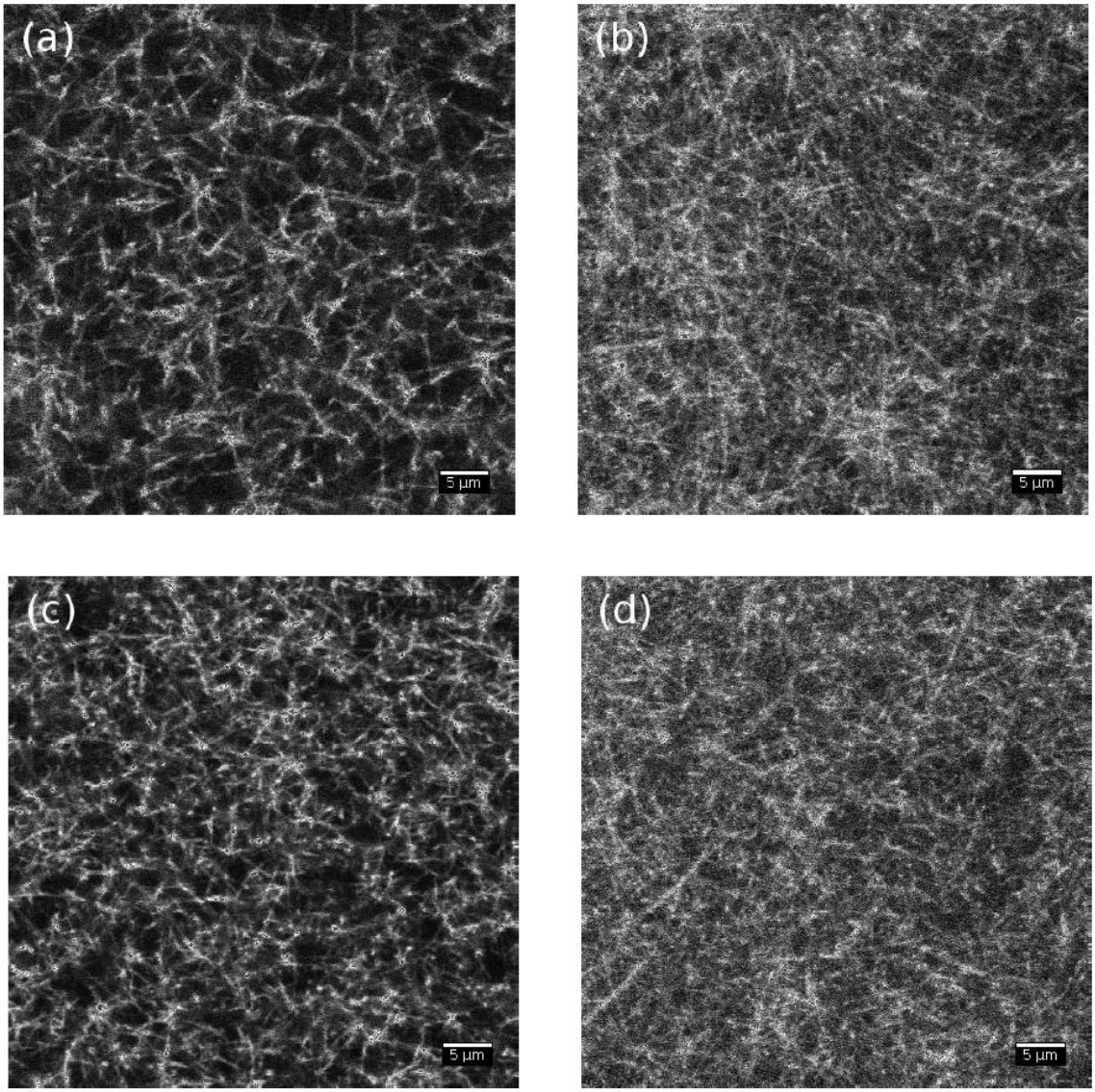

Figure 1. Representative images of (b) 50μM and (d) 60μM non-stabilized networks; and (a) 17.4 μM (c) 33.1 GMPCPP-stabilized networks. The networks (a)-(b) and (c)-(d) show structural similarities in terms the average network mesh size, MT length, bundling and polymerized MT concentration.

Having established the protocols for controllable assembly of non-stabilized MT networks, we next wanted to observe time dependent changes in the network structure so performed time-lapse imaging of the networks on an Olympus Fluoview 1000 spectral confocal microscope, equipped with 60X oil immersion objective, N.A.=1.4. The results of these measurements are rather surprising in that we have not been able to directly observe restructuring events on the time scale of minutes, which suggests a possible stabilization mechanism is acting on these networks to prevent rapid MT dynamics. Also, as shown in Figure 2, it is difficult to distinguish between the inherent drift in the 50μM non-stabilized MT network sample versus possible dynamics of individual MTs. This is partly due to the slow raster scan speeds of the microscope, at ~5sec per *x*-*y* scan, coupled to our desire to acquire *z*-stacks on the order of ~20μm with ~1μm *z*-steps. Over these time scales, the filaments can reptate or diffuse out of the field of view, rendering it impossible determine length changes on individual MTs.

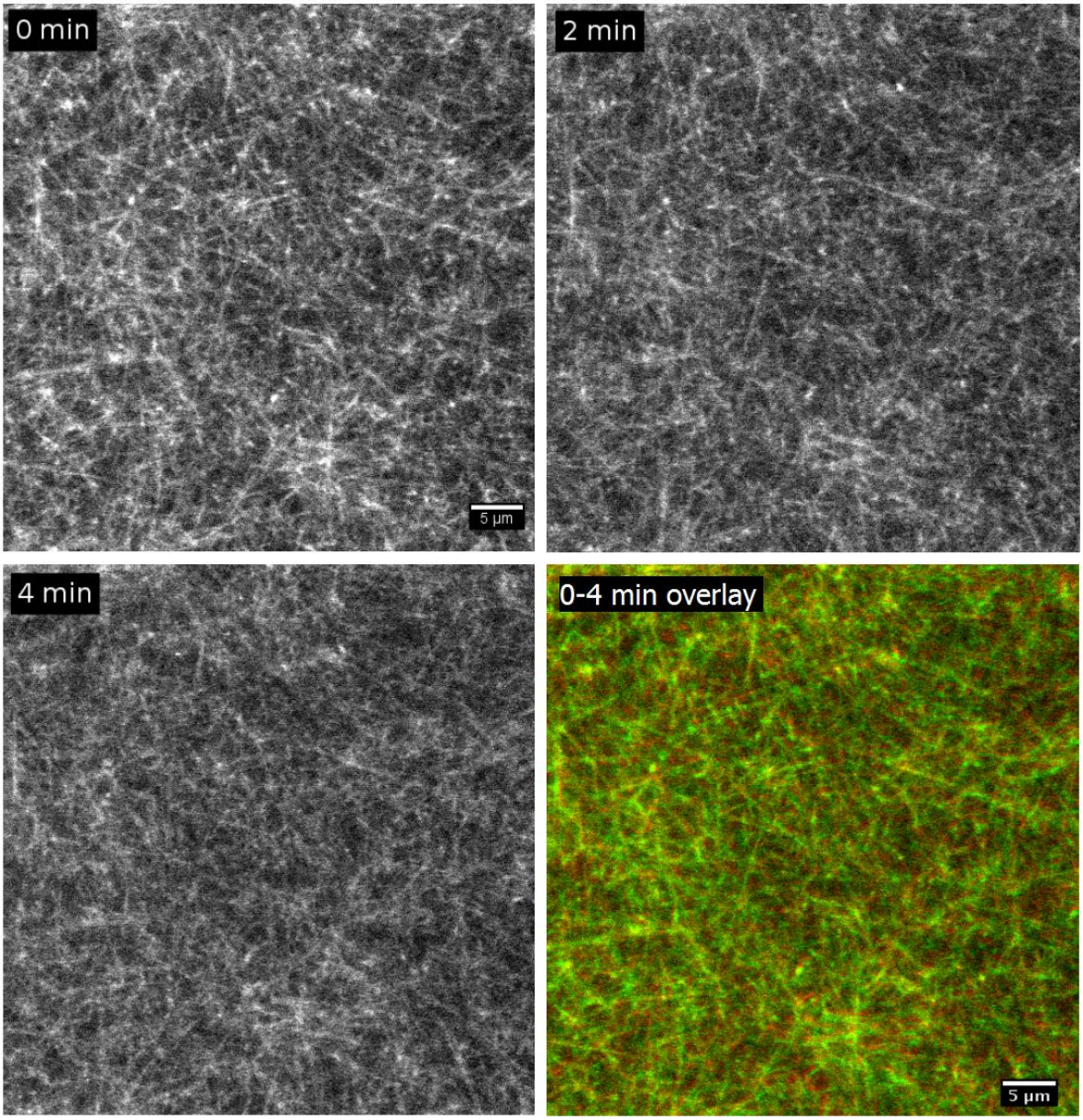

Figure 2. Time-lapse imaging of 50µM non-stabilized MT networks show that the networks do not show long-range restructuring events on the order of minutes. Bottom right panel shows an overlay of the images at 0 and 4 minutes in green and red, respectively; it is hard to distinguish structural changes between the time points.

2. Passive Microrheology Studies on GMPCPP-stabilized and non-stabilized MT networks

After performing rather qualitative studies of structure determination of MTs via confocal imaging and established structural similarities between various concentrations of stabilized and non-stabilized networks, we performed passive microrheology on both types of networks using 2.5μm polystyrene particles and a Pointgrey Chameleon CM3-U3-13Y3M camera with a time resolution of 8.2 ms. In Figure 3, representative trajectories are superimposed for particles moving within (a) 17μM stabilized (blue), 50μM non-stabilized (red), (b) 33μM stabilized (blue) and 60μM non-stabilized (red) MT networks for 60 time points. In all cases, a representative data trace of beads freely diffusing in water (green) are also included for comparison. The trajectories of beads moving in water appear to be qualitatively similar to those of beads moving in the MT networks, particularly for the more dilute suspension (Figure 3a) which suggests that in this case, the MT network forms a loose fairly open meshwork that allows particles to move within and between neighboring pores, thereby providing very little hindrance to long-range particle diffusion.

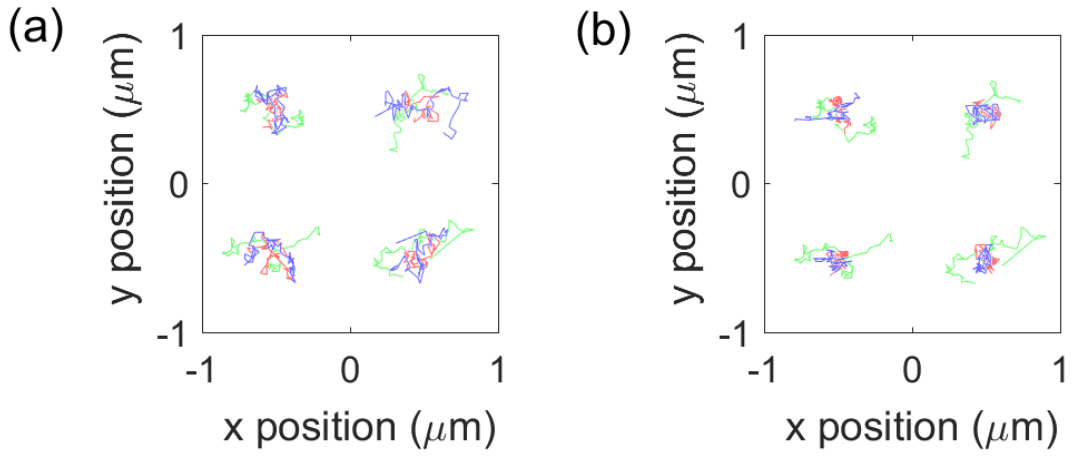

Figure 3. Representative time traces showing particle trajectories for 2.5μm polystyrene beads moving within (a) 17μM stabilized (blue), 50μM non-stabilized (red), (b) 33μM stabilized (blue) and 60μM non-stabilized (red) MT networks; trajectories of identical particles moving in water (green) show similarities between the corresponding stabilized and non-stabilized networks. The traces are plotted for 60 time points with a temporal resolution of 8.2 ms.

To explore this more quantitatively, we calculate the ensemble-averaged mean-squared tracer displacement $\langle \Delta x^2(\tau) \rangle = \langle |x(t+\tau) - x(t)|^2 \rangle$ as a function of lag time τ, angled brackets indicate an average over many starting times *t* and an ensemble of particles. For a viscous fluid, the particle motion is purely diffusive, and $\langle \Delta x^2(\tau) \rangle = 2dD\tau$ where *d* is the space dimension (here we track 2-dimensional particle motion only, so *d*=2), and *D* is the diffusion coefficient. For a simple fluid, *D* is related to the shear viscosity η through the Stokes-Einstein relation:

$$D = \frac{k_B T}{6\pi\eta a}$$

where k_B is the Boltzmann constant, *T* is temperature, and *a* is the particle radius. When particles move in more complex environments, either due to complex, frequency dependent viscoelastic moduli of the surrounding material, or the presence of obstacles or pores (or both), then the mean squared displacement can provide information about the local mechanical and structural properties of the material [4]. In general, in complex passive materials (*i.e.* thermally activated materials lacking any biological or catalytic activity that would provide additional energy inputs beyond $k_B T$) the mean squared displacements will show subdiffusive dynamics, in which $\langle \Delta x^2(\tau) \rangle \sim \tau^\alpha$ where $\alpha < 1$.

As shown in Figure 4, shows that the mean squared displacements (MSDs) of particles moving in non-stabilized 50μM non-stabilized networks show similar behavior as GMPCPP-stabilized 17μM networks. Similarly, the beads in 60μM non-stabilized networks show similar behavior as GMPCPP-stabilized 33μM networks. At short time scales the MSDs are roughly linear in lag time, suggesting a primarily viscous response; however, the value of the local effective viscosity decreases within increasing tubulin concentration (as shown by the *y*-intercept value of the log-log plot). Confinement of the bead by the surrounding network is indicated by deviation from linearity on long timescales. As seen in Figure 4, this is clearly the case for non-stabilized networks with concentrations above 50μM and 17μM for GMPCPP networks. We also do not observe MT network formation below 25μM [tubulin] without stabilization, which sets a lower bound on the concentrations that can be studied in this framework.

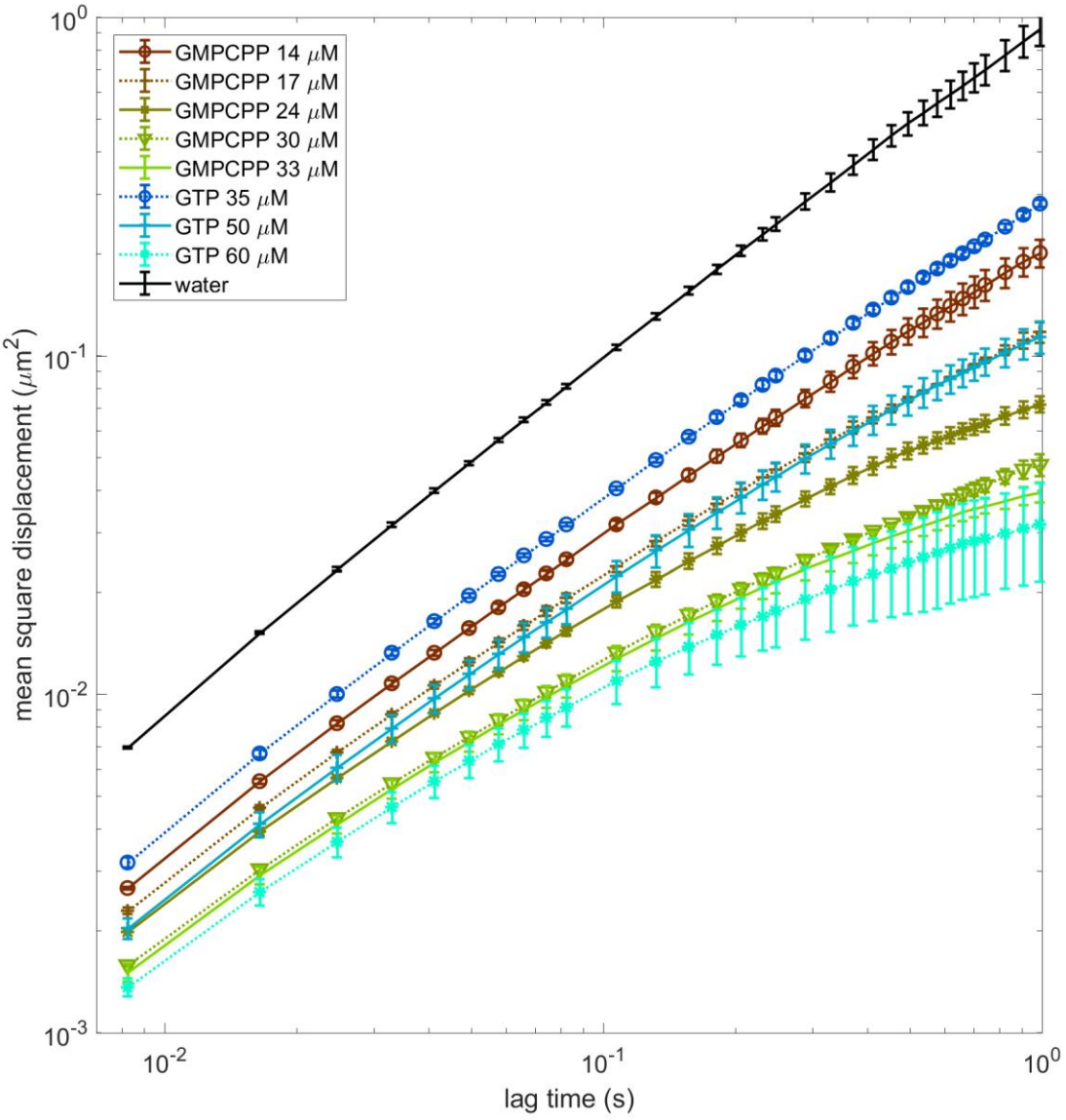

Figure 4. Mean-squared-displacements of 2.5μM beads in stabilized and non-stabilized MT networks show sub-diffusion and network confinement in long timescales. A maximum lag time of 1.0 s is calculated to ensures that there are at least 30 beads per time trace in the recorded movies. Error bars are standard deviations around the mean values for six measurements.

In order to further study the potential effects of network dynamics in our system, we compared the distribution of particle displacements at a fixed lag time τ, $P(\Delta x,\tau)$, known as the van-Hove correlation function for the GMPCPP and non-stabilized networks of matching morphology[4]. As seen in Figure 5, with a lag time of 1/121.25s the van-Hove correlation functions of 2.5μm beads moving in the corresponding stabilized and non-stabilized networks is practically indistinguishable and they show clear deviation from Brownian diffusion which is indicated by the deviation from the Gaussian fits to the observed data for large displacements. The origins of these deviations are not yet clear. It is possible that these arise from the superposition of many Gaussian distributions of single particles moving in slightly different local environments, which tends to broaden the probability distribution of the ensemble, particularly at large displacements. It is also possible that the MTs form a complex, inhomogeneous network with several characteristic structural length scales that influence the trajectories, and therefore displacement distributions, of the particles moving within it. In the future it may be possible to distinguish these possibilities by collecting more statistics on the motions of individual particles and also by simultaneously measuring the motions of the network and the particles using high-speed imaging and two-color visualization schemes.

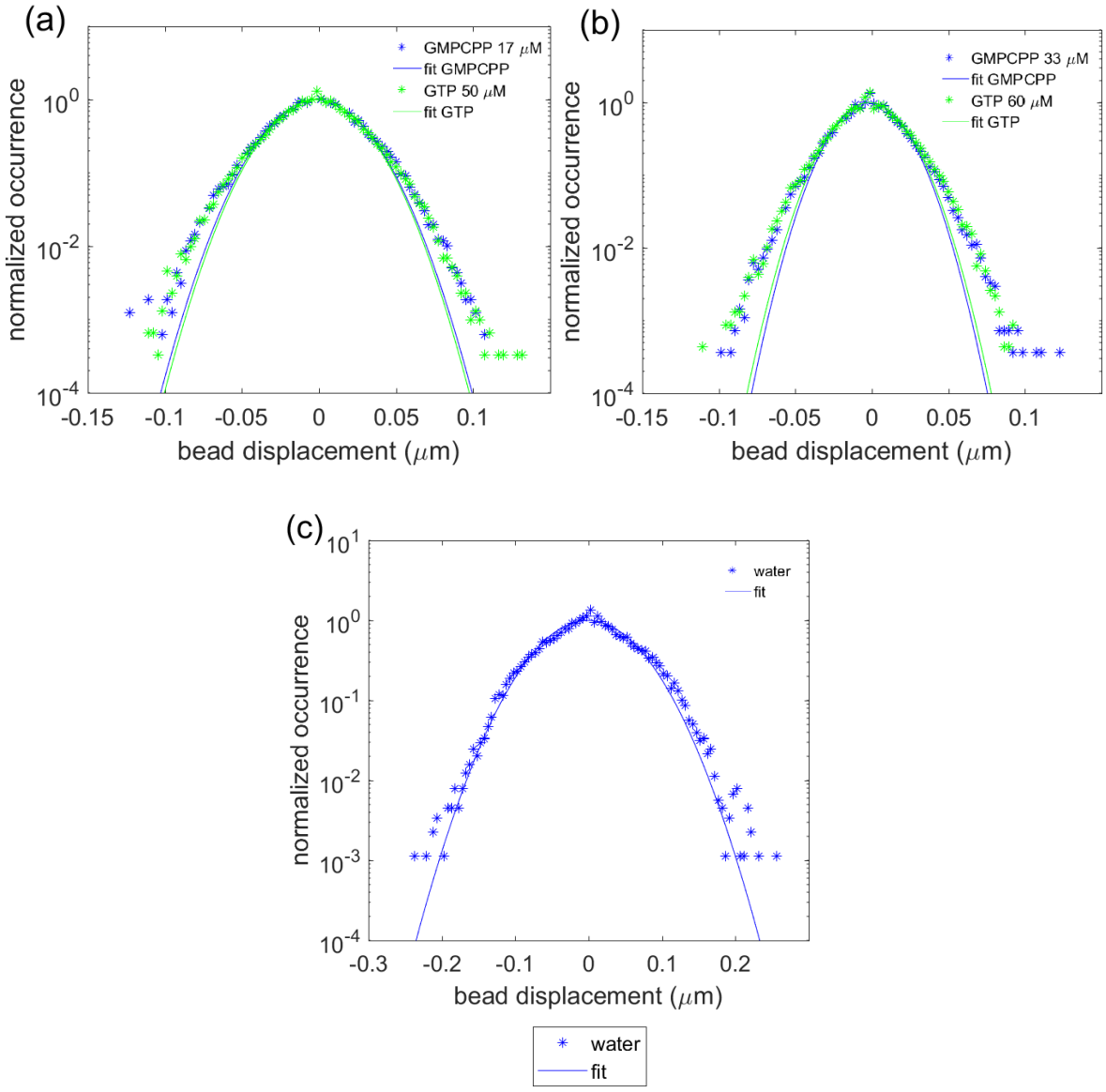

Figure 5. Van-Hove correlation functions for particles moving in microtubule networks. (a) the distributions of bead displacements at 17μM GMPCPP 50μM GTP networks, and (b) 33μM GMPCPP and 60μM GTP networks do not compare well with the Gaussian fit, particularly at large displacements. (c) Control measurements of van-Hove correlation functions of 2.5μM particles moving in water show good match between the expected Gaussian fit.

Conclusion:

In this work aimed to develop a framework where we can study the effects of MT dynamics on the overall mechanics of *in vitro* microtubule networks. We established that we can assemble microtubules without chemical stabilizers such as taxol and DMSO. We have also created structural "control" networks that are stabilized with GMPCPP, which are similar to the non-stabilized networks in terms of their overall morphology. We have investigated both with structural imaging (via confocal microscopy) and microrheological characterization. Taken together, these data suggest that non-stabilized networks might lack dynamics on the time scales of the imaging and microrheology measurements performed here (approximately 1-100 s). This could be due to a few factors including possible steric stabilization of microtubule polymerization/depolymerization events due to interaction of individual microtubules and/or some trace amount of residual GMPCPP (<1.7uM) that is present in all of the experiments discussed here. Even though we have shown that this amount of GMPCPP in the tubulin solution does not assemble stable microtubules at the tubulin concentrations considered here, it is possible that no matter how little of it is present in the solution, once incorporated into the MT lattice, GMPCPP might prevent depolymerization of the microtubules. In the future, Fluorescence Recovery After Photobleaching (FRAP) studies of these networks, and/or super-resolution microscopy may shed light on this issue. At present, although we have made significant progress toward studying the effects of MT polymerization/depolymerization dynamics in microtubule

networks, this remains work in progress and as of today, observing “truly dynamic” behavior in MT networks stands as a challenge.

References:

1- Mitchison, Tim, and Marc Kirschner. "Dynamic instability of microtubule growth." Nature 312.5991 (1984): 237-242.

2- Holy, Timothy E., and Stanislas Leibler. "Dynamic instability of microtubules as an efficient way to search in space." Proceedings of the National Academy of Sciences 91.12 (1994): 5682-5685

3- Waterman-Storer, Clare M., et al. "Microtubule growth activates Rac1 to promote lamellipodial protrusion in fibroblasts." Nature Cell Biology 1.1 (1999): 45-50.

4- Valentine M. T., Kaplan P. D., et. al. “Investigating the microenvironments of inhomogeneous soft materials with multiple particle tracking.” Phys. Rev. E 64, (2001) 061506

Appendix C: Investigation of Extracellular Stresses near Rounded Mitotic Cells under Confinement [4]

Mitotic cell rounding is now accepted as a universal mechanism by which cells that undergo division round up to provide space for dramatic intercellular reorganization events that take place during this period [1-2]. Due to the inherently large shape changes involved in mitosis and cytokinesis, cells that are embedded in tissues might experience substantial extracellular mechanical responses from their immediate microenvironment [3-4]. In order to understand the effects of confinement on the cell behavior we investigated the responses of fertilized white sea urchin (*L.Pictus*) eggs embedded in mechanically-controlled agarose hydrogels which provide a tunable confinement environment.

As seen in Figure 1, fertilized urchin embryos assume a spherical geometry. This highly idealized geometry allows us to treat the cells as model spheres, which greatly simplifies the analysis and modeling. Experimentally, we quantify the circularity of urchin embryos by thresholding a representative bright field image of a freshly fertilized batch, and compare their major, ax_{major}, and minor, ax_{minor}, axes of the ellipses fit to the outlines that are determined from the thresholded images. For the circularity metric, *C*, we use:

$$C = \frac{ax_{major} - ax_{minor}}{(ax_{major} + ax_{minor})/2} \tag{32}$$

where a perfect circle would have $C = 0$.

[4] I would like to thank Dr. Kathy Foltz and Dr. Carl Meinhart for their help and guidance through this project.

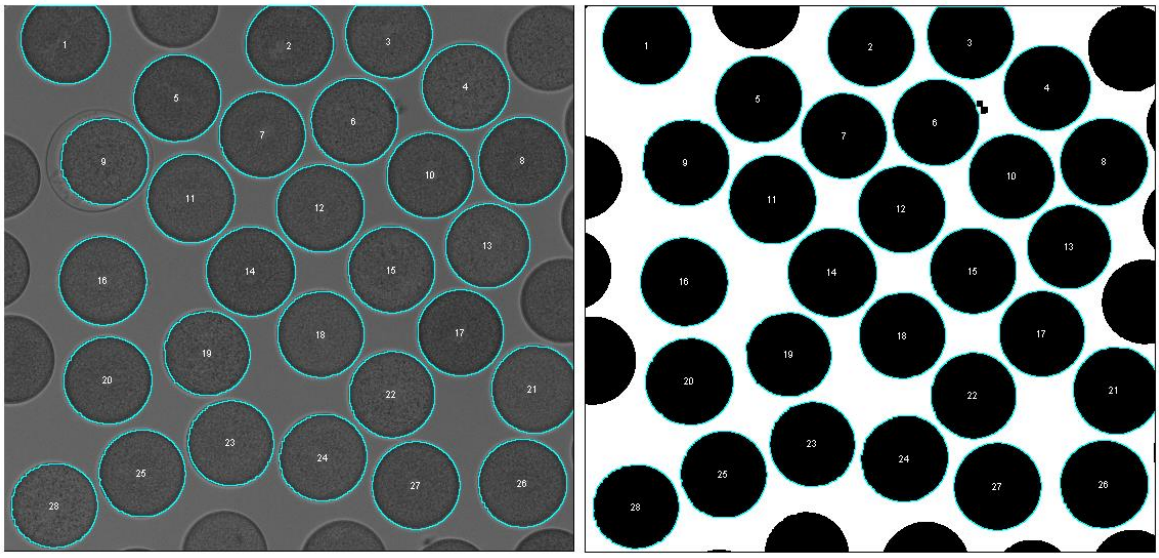

Figure 1. Bright field image of freshly fertilized white sea urchin eggs. The eggs round up upon fertilization. the image is thresholded and ellipses are fit to the detected boundaries on the thresholded image (right panel) and overlaid on the original image (left panel).

For the image displayed above, the average circularity factor that is calculated for all cells that do not intersect with the image boundary is 1.22±0.8%, where 1.22% is the mean and 0.8% is the standard deviation around the mean for the 24 measurements shown above.

In the context of tissues, the external confinement comes from the non-homogenous and highly dynamic cellular environment [4], which presents challenges for controlled tuning of the local physical properties. Upon fertilization, sea urchin embryos develop a protective mesh around the embryo, called the *hyaline layer*, which is crosslinked by divalent ions, especially calcium, that are abundant in sea water. As displayed in Figure 2, we found that by changing the calcium concentration of the medium in which the urchin embryos are suspended, it is possible to tune the stiffness of the hyaline layer, and therefore and induce

direct mechanical confinement of the embryos without the use of an external hydrogel. However, the amount of calcium that can be added to the solution without changing its osmolarity is bounded from above; therefore, tuning the hyaline layer stiffness by changing calcium concentration is not suitable for controlled studies of cell confinement.

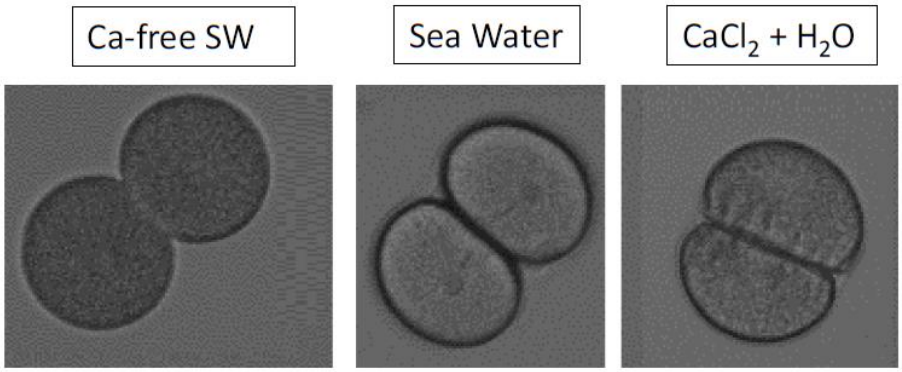

Figure 2. Calcium-dependent tuning of the hyaline stiffness shows that cells are mechanically confined by adjusting the calcium level in the suspension medium. Low levels of calcium dissolve the hyaline layer while higher levels induce more crosslinking, making the hyaline layer stiffer. (The osmolarity of the Calcium chloride solution is matched to that of sea water.)

Through these same studies, we also observed that in the absence of solution calcium ions (*i.e.* in Calcium-free sea water), the daughter cells assume a fully spherical geometry (Figure 2, left panel), which suggests that the hyaline mesh is dissolved to the extent that it does not contribute to the overall mechanics of the embryo when compared with the forces that are associated with the basal acto-myosin activity in the cortex. Therefore, to mimic the

mechanical effects of confinement and have controlled microenvironments we used calcium-free seawater (CFSW) in our encapsulation studies to ensure that the mechanical confinement effects are due to the presence of the external hydrogel only. To achieve this, we encapsulated fertilized embryos in soft gels made of ultra-low melting point agarose and used confocal microscopy and finite element modeling (FEM) to investigate their response. As described below, we observed that the mitotic rounding generates enough space for successful completion of division under all confinement conditions, and that the cells can complete mitosis regardless of the stiffness of the external environment

We encapsulated freshly fertilized, spherical sea urchin embryos in hydrogels of varying stiffnesses and observed their geometry (Figure 3). We find that once the embryos assume their spherical geometry, they are extremely robust to different levels of mechanical confinement and are able to successfully complete cytokinesis and furrowing, even under conditions that allow for little to no compression of the external material.

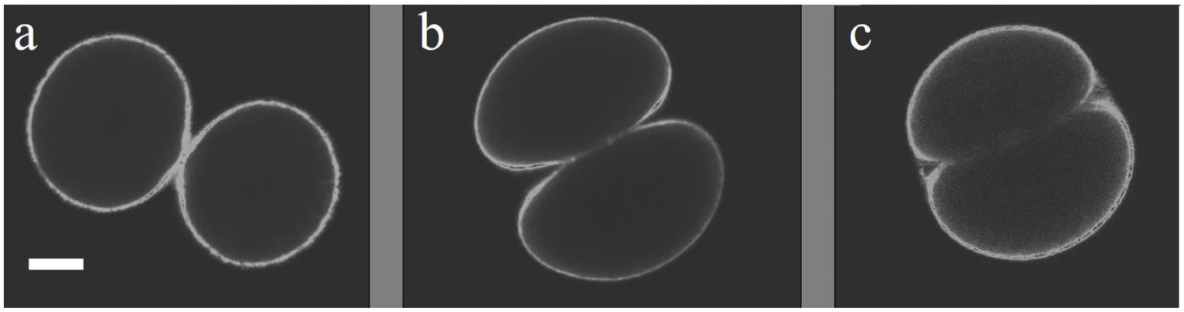

Figure 3. Encapsulation experiments with urchin embryos in gels of increasing stiffness. Division in a) calcium-free sea water, b) 0.75% (w/v) soft agarose gels with moderate confinement, c) 1% (w/v) stiff agarose gels, shows that rounded up mitotic sea urchin embryos are robust to varying levels of mechanical confinement and they successfully complete cytokinesis, independent of the stiffness of the external microenvironment.

To understand the biophysical mechanisms behind the observed behavior of dividing urchins and the stresses that develop inside the external matrix, we implemented a finite element model of the dividing cell using active gel theory, as explained in [5], using COMSOL; this allows for multiphysics simulations of cell-matrix interactions, without the need for manually implementing the force balance on the cell cortex-matrix boundary. We used the description of cortical stress generation and dissipation in [5], assumed axisymmetry, and modeled the overactivity of the myosin phosphorylation along the equator as a Gaussian defined on the curvilinear length from the equator as described [5]. Figure 4 displays the immunostaining of dividing urchin cells, fixed and stained various time points

into division, which supports the assumption of Gaussian distribution of myosin overactivity along the equator.

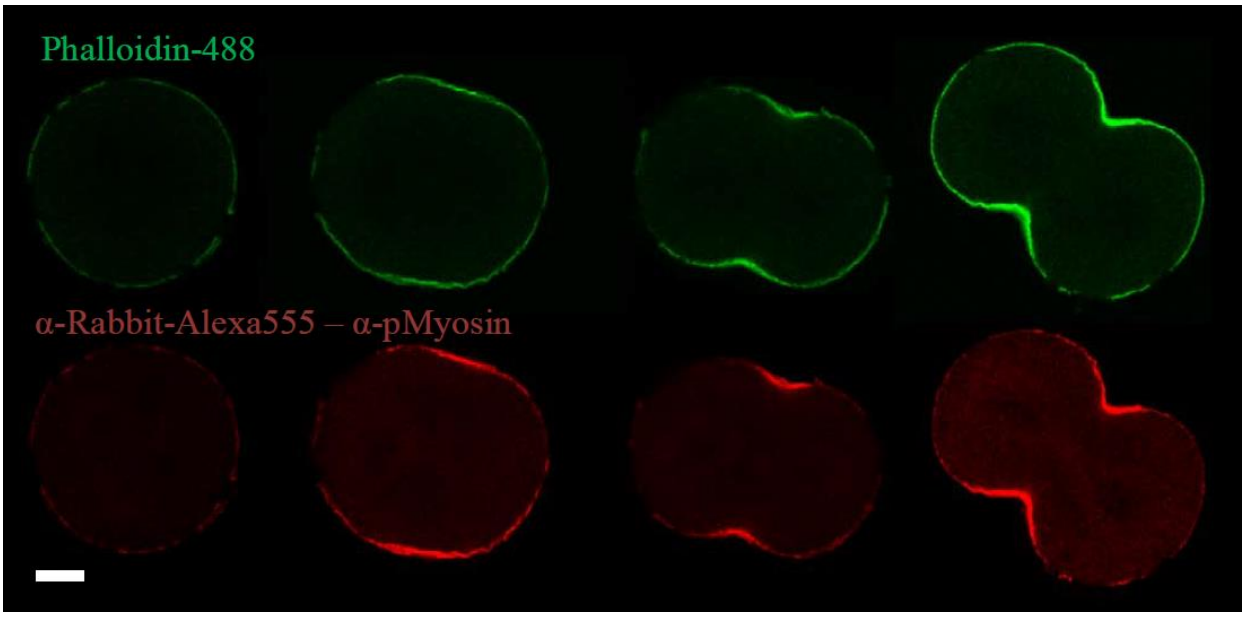

Figure 4. F-actin and phosphorylated myosin immunolabeling shows myosin over-activity along the equator, which is modeled as a Gaussian distribution along the contour of the cell cortex. (Scale bar is 20μm.)

As shown in Figure 5, below, our COMSOL implementation of the active cortex model captures the main shape changes that occur during different stages of cell division, which is consistent with the results of [5] and our experiments with white urchin embryos.

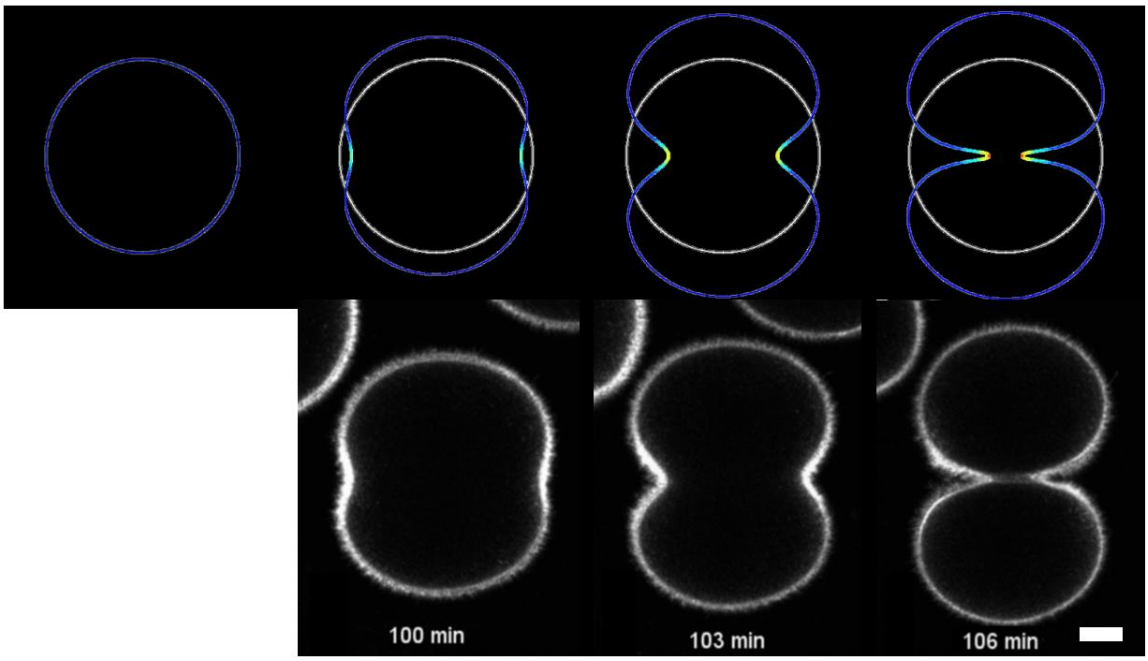

Figure 5. Top panel, COMSOL simulations of a dividing rounded cell. The model successfully captures the main behavior of the dividing cell in terms of total shape changes induced by the acto-myosin contractility. (Scale bar is 20µm)

Next, we used our model discussed above and placed it inside an elastic medium, shown in blue in Figure 5, below. Use of COMSOL allows multiphysics simulations of the cellular and external elastic domains. Figure 5, shows an example of simulated division inside a soft hydrogel, where the colormap represents Von Mises stress both inside the cortex and the elastic matrix. Inside the elastic medium, stresses develop at the poles of cells which are the points of maximal deformations.

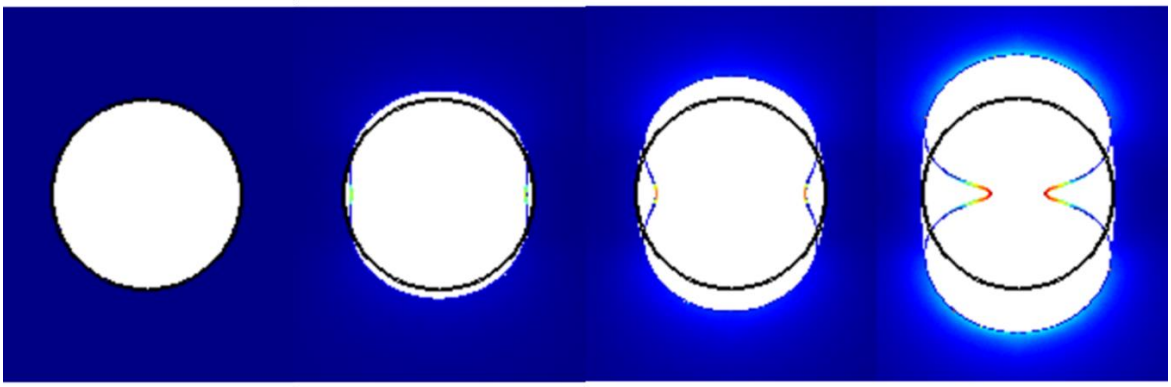

Figure 5. Von Mises stress is plotted as calculated from the elastic stresses inside encapsulating soft material. The values of stress are arbitrary. Blue: no stress, red: high stress.

Future Work and Challenges:

In encapsulation experiments, otherwise transparent agarose hydrogels are seeded with fluorescent particles to track 3D material deformations inside the hydrogel. However, the first division in white urchin embryos is axisymmetric along the polar axis; therefore, in theory, knowing the displacement field everywhere along any plane that contains the polar axis would suffice to describe the entire deformation field. However, in practice it is not practical to image a single plane because the cells are randomly oriented within the hydrogel and the axes are almost never aligned with the *x-y* plane which requires collection of data in the form of *x-y-z* raster scanning, necessitating volume imaging. In addition, even if the fully aligned axis and imaging plane criteria was met, the material tracers are randomly scattered inside the hydrogel; therefore, only a very limited number of material points would fall in the imaging plane, providing scarce details about the displacement field in plane.

Additionally, depending on the orientation of the cell within the hydrogel, there is a significant effect of light scattering and intensity attenuation due to the presence of the gel and cellular structures; this makes quantitative comparisons of intensities from differing locations within the gel very challenging.

Finally, the need for volumetric imaging substantially complicates the experiment. From the start of detectable shape changes to the completion of cytokinesis, the division takes ~10 mins in the urchin embryos. And for a conventional confocal raster scan imaging setup, with reasonable resolution in *z*-direction, the volumetric image stack collection takes ~4 minutes. The lack of separation of timescales for imaging and dynamic structural rearrangements of cell division have stymied progress on this project. Therefore, a faster imaging system, such as SPIM microscopy or a resonant scanning confocal microscope would be better-suited for this experiment. SPIM is particularly attractive, as this method requires that samples be embedded inside agarose hydrogels, which naturally is the case for our experiments. Fortunately, both instruments have recently been acquired and are now in use in the NRI/MCDB confocal microscopy facility. We anticipate that groundwork laid in these initial experiments and modeling efforts will allow for future investigation of cellular division dynamics at fast time scales.

Experimental Methods

Immunofluorescence Protocol for encapsulating and fixing Urchin Embryos in Agarose Gels:

(Optimized for imaging of cortical actin in L.Pictus embryos)

Original author: Ian Townley, Foltz Lab, UCSB

Updated by K. Foltz, June 19, 2015.

Updated by B. Kaytanli, Feb 24, 2017

See these references:

Townley et al. (2009) Dev Biol, 327, 465

Chan et al. (2013) Mol Biol Cell 24, 3472

All washes are done in filtered sea water unless otherwise is stated.

Spawn:

1. Spawn urchin (as described in "Urchin gametes").

• Wash eggs 5x, and once in 2mM 3-Amino-1,2,4-triazole solution in filtered seawater.

2. Fertilize eggs.

• Predilute sperm in 2mM 3-Amino-1,2,4-triazole; add to eggs; mix with spatula.

• The final sperm dilution should be between 1:10,000 and 20,000.

• The total volume should be around 20ml.

• Observe for fertilization envelope rise under scope (should take 30 to 45 sec for 95% of the fertilization envelopes to rise if eggs are healthy).

3. Strip off fertilization envelopes by passing eggs through 210uM Nitex mesh, 8x.

4. Settle, decant and wash 2x.

5. Move to CFSW at 30 mins post-fertilization. Settle, decant and wash in calcium-free sea water 2x.

Encapsulation:

1. Prepare 1% (w/v) Agarose, with calcium-free seawater and ultra-low melting point agarose (Sigma: #A2579 Type IX-A). Cool to room temperature.

2. Suspend fertilized embryos calcium-free seawater 1:4 in the agarose solution to have a final agarose concentration of 0.75% (w/v). (For softer gels, suspend 1:2 for 0.5%(w/v).)

3. Drop cast the agarose + embryo pregel solution on cover glass and immediately place on ice to prevent ebryos from settling, Gel on ice for 30 seconds.

4. Store at 10C room with a drop of calcium-free seawater to cover the gel surface in order to swell and prevent gel evaporation.

5 Take for live imaging.

Methods Used for Fixing and Immunolabeling:

All staining and fixing is carried out by wicking out the excess solution on top of the gels and placing the solution of interest on top.

1. 10 minutes prior to the time point the embryos want to be arrested (fixed), add FMFX-464 (Thermofisher #F34653) membrane dye at 5mg/ml in calcium-free seawater on top of the gel and let it perfuse all the way.

2. For fixing, add 5% glutaraldehyde-FSW on top of the gel and let it perfuse and fix for 10 minutes.

3. Wash with wash buffer 3 x 10 minutes to permeabilize.

4. Block with blocking buffer for 2 hours.

5. Incubate with secondary antibody, (Phalloidin conjugated to Alexa Fluor 488 or Phospho-Myosin Light Chain 2 (Ser19) Antibody (Cell Signaling Technology, #3671)) at 1:200 in blocking buffer for 1 hour.

6. Wash with wash buffer 2 x 10 minutes and keep in wash buffer for an hour at 4C to reduce background.

7. Wash with wash buffer one last time and image using Olympus-1000 confocal using a 20X objective.

Basic Materials:

• 2 detergent free 200 mL glass beakers

• 210 um Nitex filter for stripping the fertilization envelope (FE)

• Cover glass (square and/ or 24 x 50) #1.5, washed.

Reagents:

• Calcium-free Sea Water pH 8.2

• 3-Amino-1,2,4-triazole

• 10x PBS pH 6.8, 7.4 or 8.0 (stock)

• Block Buffer: 2% BSA in 1X PBS or

2% BSA in 1X PBS with 0.03% TX-100, 1 mM Na_3VO_4, 1 mM NaF, donkey serum (1:60) to help with specificity; make fresh.

• Fix Buffer: 5% glutaraldehyde in filtered sea water

• Wash Buffer: 0.1% TX-100 in PBS OR 0.2% Tween-20, 1 mM Na3VO4, 1 mM NaF in PBS.

Recipe for 10X PBS stock: Dissolve the following in 800 mL distilled H_2O:

80g of NaCl, 2.0g of KCl, 14.4g of Na_2HPO_4, 2.4g of KH_2PO_4

Adjust pH to 7.4 and working volume to 1L with additional distilled H_2O.

Note also that the phosphatase inhibitors – vanadate (Na_3VO_4) and sodium fluoride (NaF) – can be prepared as 100X or 1000X stocks, aliquoted and frozen. They should be added to the freshly prepared buffers just before use.

Recipe for calcium-free sea water: Dissolve the following in 1 L distilled H_2O:

26.3g of NaCl, 0.67g of KCl, 6.3g of $MgSO_4.7H_2O$, 4.7g of $MgCl_2.6H_2O$, 0.18g $NaHCO_3.H_2O$

References

[1] O. Lancaster, M. LeBerre, A. Dimitracopoulos, D. Bonazzi, E. Zlotek-Zlotkiewicz, R. Picone, T. Duke, M. Piel, and B. Baum, "Mitotic Rounding Alters Cell Geometry to Ensure Efficient Bipolar Spindle Formation," Dev. Cell, vol. 25, no. 3, pp. 270–283, 2013.

[2] M. P. Stewart, J. Helenius, Y. Toyoda, S. P. Ramanathan, D. J. Muller, and A. a Hyman, "Hydrostatic pressure and the actomyosin cortex drive mitotic cell rounding.," Nature, vol. 469, no. 7329, pp. 226–230, 2011.

[3] B. Sorce, C. Escobedo, Y. Toyoda, M. P. Stewart, C. J. Cattin, R. Newton, I. Banerjee, A. Stettler, B. Roska, S. Eaton, A. A. Hyman, A. Hierlemann, and D. J. Müller, "Mitotic cells contract actomyosin cortex and generate pressure to round against or escape epithelial confinement," Nat. Commun., vol. 6, p. 8872, 2015.

[4] S. P. Ramanathan, J. Helenius, M. P. Stewart, C. J. Cattin, A. A. Hyman, and D. J. Muller, "Cdk1-dependent mitotic enrichment of cortical myosin II promotes cell rounding against confinement," Nat. Cell Biol., vol. 17, no. 2, pp. 148–159, 2015.

[5] B. Audoly, J. Prost, and P. Vi, “Furrow Constriction in Animal Cell Cytokinesis,” vol. 106, no. January, 2014.

Appendix D: Development of a Novel Hough Transform Method for Efficient Detection and Characterization of Elliptical Features in Microscopy Images

Journal Article:

Evolute-based Hough transform method for characterization of ellipsoids[5]

Authors: Bugra Kaytanli and Megan T. Valentine

DOI: 10.1111/jmi.12004

Abstract

We propose a novel and algorithmically simple Hough transform method that exploits the geometric properties of ellipses to enable the robust determination of the ellipse position and properties. We make use of the unique features of the evolute created by Hough voting along the gradient vectors of a two-dimensional image to determine the ellipse centre, orientation and aspect ratio. A second one-dimensional voting is performed on the minor axis to uniquely determine the ellipse size. This reduction of search space substantially simplifies the algorithmic complexity. To demonstrate the accuracy of our method, we present analysis of single and multiple ellipsoidal particles, including polydisperse and imperfect ellipsoids, in both simulated images and electron micrographs. Given its mathematical simplicity, ease of implementation and reasonable algorithmic completion

[5] Reprinted with Permission from Journal of Microscopy.

time, we anticipate that the proposed method will be broadly useful for image processing of ellipsoidal particles, including their detection and tracking for studies of colloidal suspensions, and for applications to drug delivery and microrheology.

Introduction

The detection of ellipses, circles, and lines is an integral part of experimental image analysis for a wide range of biological, chemical, and mechanical engineering applications. Of these three classic object shapes, the most general is the ellipse, as the remaining two objects can be expressed as special cases in which the major and minor axes lengths are equal or the length of the minor axis is zero. Ellipse detection enables the size, shape and orientation of naturally-occurring anisotropic structures (*i.e.* red blood cells and bacteria) to be determined. Further, it allows the characterization of synthetic ellipsoidal particles, which have become increasing important in colloidal studies (Keville *et al.*, 1991, Crassous *et al.*, 2012, Sacanna *et al.*, 2006, Champion *et al.*, 2007, Ho *et al.*, 1993). The shape anisotropy of ellipsoids gives rise to novel interparticle and hydrodynamic interactions, and allows ordered liquid crystalline phases to form at high volume fraction (Madivala *et al.*, 2009, Zheng & Han, 2010, Melle *et al.*, 2002, Güell *et al.*, 2010, Han *et al.*, 2009). Ellipsoidal particles have broad engineering applications, ranging from the self assembly of novel photonic band gap structures to the geometrically-controlled uptake of drug-infused structures through cellular phagocytosis (Ding *et al.*, 2009, Champion & Mitragotri, 2006, Velikov *et al.*, 2002).

Due to the clear technological importance, a number of algorithms to detect and characterize ellipses in digital images have been developed (Fitzgibbon *et al.*, 1999, Hahn *et*

al., 2008, Kawaguchi & Nagata, 1998, Yu *et al.*, 2004). Unlike spherical particle detection, in which a small number of robust centroid tracking algorithms have emerged as standard tools, the computational requirements and algorithm complexity of ellipse detection software has largely limited its practical use in colloid science (Crocker & Grier, 1996, Jenkins & Egelhaaf, 2008). One of the most widely used computer vision tools is the Hough transform (HT) method, in which the features (*i.e.* size, shape, orientation) of a real-space image are transformed into discrete points of a parameter space (Duda & Hart, 1972, Hough, 1962). This multi-dimensional parameter space is then searched to uniquely identify and characterize the original object. In this article, we report a new implementation of the HT that exploits the geometric features of ellipses to reduce algorithm complexity, provides rapid analysis of image quality and accurately determines the shape, size and orientation of even imperfect ellipses. We demonstrate its utility using both simulated and experimental images of ellipsoidal colloids. Our method provides accuracy and speed that is comparable to that of direct fitting by a least squares minimization approach, but additionally allows for rapid assessment of image quality and enables identification and characterization of adjacent or touching objects.

Methodology

Prior HT methods have been used successfully in the detection of spheroidal objects in two-dimensional images (Jenkins & Egelhaaf, 2008, Irmscher *et al.*, 2012). Circles are represented using three independent parameters: the centre coordinates (x_c, y_c) and the radius r. The resulting Hough space is thus three-dimensional, and the classical circular HT algorithm has $O(N^3)$ space requirements and $O(N^4)$ time complexity for an image $I(x,y)$ of

size $N \times N$ pixels. The memory requirements and completion time can be reduced by completing the search in two consecutive steps (Illingworth & Kittler, 1987, Peng *et al.*, 2007, Bennett *et al.*, 1999, Kanatani & Ohta, 2004, Yoo & Sethi, 1993). First, the gradient of the image is determined by calculating the centred differences in intensity. For a circle, the gradient $\left(\frac{\partial I}{\partial x}, \frac{\partial I}{\partial y}\right)$ consists of a radially-symmetric array of vectors that all intersect at the centre. Thus, it is possible to identify the circle centre by identifying the most likely point of intersection. In practice, this is achieved by creating a new accumulation array (typically $N \times N$) in which the gradient vector at each pixel in the original image is represented by a line that emanates in both directions from the same pixel in the accumulation array, at an angle $\varphi = \tan^{-1}\left(\frac{\partial I}{\partial y} / \frac{\partial I}{\partial x}\right)$ (Peng et al., 2007). Each line extends across the entire accumulation array, and each pixel intersected by the line receives one weighted vote, where the weight function is given by the gradient magnitude $w = \left[\left(\frac{\partial I}{\partial x}\right)^2 + \left(\frac{\partial I}{\partial y}\right)^2\right]^{1/2}$. If the expected range of circle radii are known, the length of the gradient vector can be truncated to minimize potential interference from neighbouring objects. The resulting accumulation array can be displayed graphically as an image. Pixels that accumulate the most votes when the contributions of all gradient vectors are summed qualify as candidate centres.

Once the candidates for the centres are detected, the voting for the radius is performed. To accomplish this, each pixel is assigned a value equal to the radial distance r to the detected circle centre, rounded down to the nearest integer. The one-dimensional accumulation array is constructed by summing the image gradient magnitudes of all pixels with a given assigned value of r, then normalizing by the number of pixels in the set. This is

repeated for each possible radius, and the value of *r* that accumulates the most votes (*i.e.* the highest normalized sum) is considered the best candidate as the circle radius.

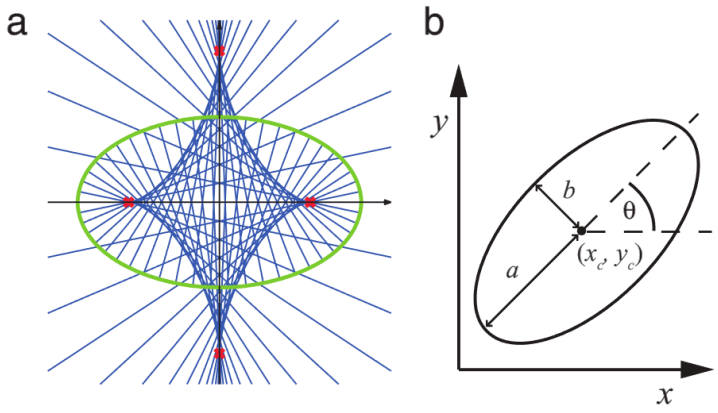

Figure 1: (**a**) The evolute of an ellipse is an astroid with four bright cusps (red dots) that can be used to determine ellipse position, orientation, shape and size. (**b**) Schematic showing the ellipse centre (x_c, y_c), orientation θ and length of the major (a) and minor (b) axes.

Applications of the HT to ellipse detection are substantially more complex, since ellipses are parameterized by five independent parameters: centre position (x_c, y_c), orientation θ, and the lengths of the major and minor axes, a and b, respectively (Aguado *et al.*, 1996, Muammar & Nixon, 1989, Pao *et al.*, 1993, Tsuji & Matsumoto, 1978, Yoo & Sethi, 1993, Xie & Ji, 2002). This typically requires a five dimensional parameter space with $O(N^5)$ space requirements and $O(N^6)$ time complexity. In this work, we reduce algorithmic complexity to $O(N^2)$ in space and $O(N^3)$ in time by using a gradient-based HT as described in (Peng et al., 2007), and by making use of the fixed points and the symmetry of ellipses. We further develop this method by exploiting the properties of the evolute of the ellipse. The evolute describes the envelope of surface normals of a geometrical object. The gradient

vectors along the perimeter of the ellipse create a radiant field in the shape of an astroid, as shown in Figure 1. For purposes of ellipse tracking, the most important points on this astroid evolute are the four cusps (indicated by red dots) where the normal rays of the ellipse are most concentrated. When the evolute is drawn over the original ellipse, two cusps lie along the major axis of the ellipse. These 'major cusps' are always found within the bounding perimeter of the ellipse, making them particularly good targets for identification by image processing. The two minor cusps can be found within or outside of the ellipse perimeter. Cusp positions are given by

$$c_a = \pm \frac{a^2 - b^2}{a},\ c_b = \pm \frac{a^2 - b^2}{b} \qquad (1)$$

where c_a and c_b are the distances from the ellipse centre to the position of the major and minor cusps, respectively. Once a pair of major cusps has been identified, the centre parameters (x_c, y_c) and the orientation θ are immediately determined. Equation 1 provides a unique relationship between the two remaining parameters a and b, which determine the shape of the ellipse. Therefore, for each valid pair, the ellipse detection is finalized by carrying out an additional one dimensional accumulator on an appropriately chosen variable. We choose this parameter to be the length of the minor axis, b, as its range is relatively small as compared to the alternatives, such as the length of the major axis (a), focal distance ($f = \sqrt{a^2 + b^2}$) or the minor cusp distance (c_b).

In practice, ellipses are detected using custom-written algorithms implemented in MATLAB, following the methods described in (Peng et al., 2007). The original image is smoothed using a Gaussian kernel, and the image gradient calculated using centred differences at each nonzero pixel. The two-dimensional accumulation array is obtained by

voting along the gradient direction, with weighting by the gradient magnitudes. This array is convolved with a local maximum (LM) finding filter, such as a Laplacian of Gaussian (LoG) kernel or an equivalent disk filter where $F_{disk} = 1/\pi r_0^2$ when $0 < r < r_0, =$ $-1.35/\pi(r_1^2 - r_0^2)$ when $r_0 < r < r_1,$ and $= 0$ when $r > r_1$. Here, $r_0 = 0.6\ r_1$ and r_1 is a user defined input that scales with the size of the object of interest. In contrast to Gaussian filters, which are commonly used for maxima detection, we find the LoG filter naturally suppresses the background offset in pixel intensity and enhances the signal to noise ratio (Neycenssac, 1993).

Cusp detection is carried out in two stages. As a first step, we multiply pixel-wise the values of the LM-filtered array and the original accumulator array, then threshold the result with a cutoff magnitude of ~10-25% of the maximum value. All pixels with values below this cutoff are set to zero, generating a two dimensional image of bright 'islands' on a dark background. We then determine the eccentricity ε using a built-in MATLAB function[6] that assigns $\varepsilon \approx 0$ to circular objects and $\varepsilon \approx 1$ to lines. To isolate bright features that likely contain cusps, we reject candidates with $\varepsilon > 0.9$. In a second step, we threshold the original two-dimensional accumulation array a cutoff magnitude of 60% of the maximum value. For each region identified in step 1, we calculate the centroid of the equivalent region in the thresholded accumulator array. The resulting positions form a list of candidate cusp coordinates.

[6] regionprops.m

From this list, we seek to identify valid pairs of major cusps, while eliminating minor cusps and image artefacts. Theoretically, any two peaks can be chosen to make a pair; however, if the range of expected ellipse shapes and sizes is known, we impose an upper and a lower bound to the interaction distance between maxima. Incorporating such *a priori* knowledge of the ellipse parameters not only constrains the possible size of the evolute to aid in cusp pairing, but also reduces the computation and storage requirements by reducing the search space.

For each remaining pair, we then perform a one-dimensional vote on the minor axis (b). For each possible value of b, there is a unique value of a, given the observed value of c_a (using Eqn. 1). To generate the accumulation array, we sum the image gradient magnitudes of all pixels that reside on an ellipse with this unique (a,b) pair with a given assigned value of b, then normalize by the number of pixels in the set. The best candidate of b is the value that accumulates the most votes by this normalized sum. In some cases, the detected cusps will not be a valid pair of major cusps, and the one-dimensional accumulation array will fail to produce a strong peak value; such pairs are eliminated.

In the limit that $a \approx b$, the four cusps collapse into a single point at the centre of the circle. Therefore, the gradient based circular HT method can be treated as a special case of the gradient-based evolute HT method proposed here. Although prior descriptions of elliptical HTs have described the evolute, to our knowledge a direct analysis of cusp positions has not been performed (Kanatani & Ohta, 2004, Luo *et al.*, 1995).

Results and Discussion

To demonstrate the utility of our method in detecting and characterizing the properties of multiple and polydisperse ellipses, we test our algorithm using simulated ellipses and experimental images of ellipsoids. First, we generate a simulated image containing four randomly oriented elliptical rings with different sizes and shapes (Fig. 2). All four ellipses are successfully detected by our algorithm; however, we find that the highly asymmetric distribution of the voting lines in the proximity of the cusp leads to a systematic underestimate of c_a. Through careful analysis of a much larger ensemble of ellipses, we determined the measured c_a to be underestimated by ~10% for all ellipse shapes and sizes. Therefore, in the implementation of the method, the detected cusp distances are corrected according to this criterion. With this correction in place, the parameters of the detected ellipses are in excellent agreement with the values used to generate the ellipses (see Table S1, Supplemental Materials). The uncertainty in centre finding is approximately one pixel and the orientation is reliably determined to within one degree.

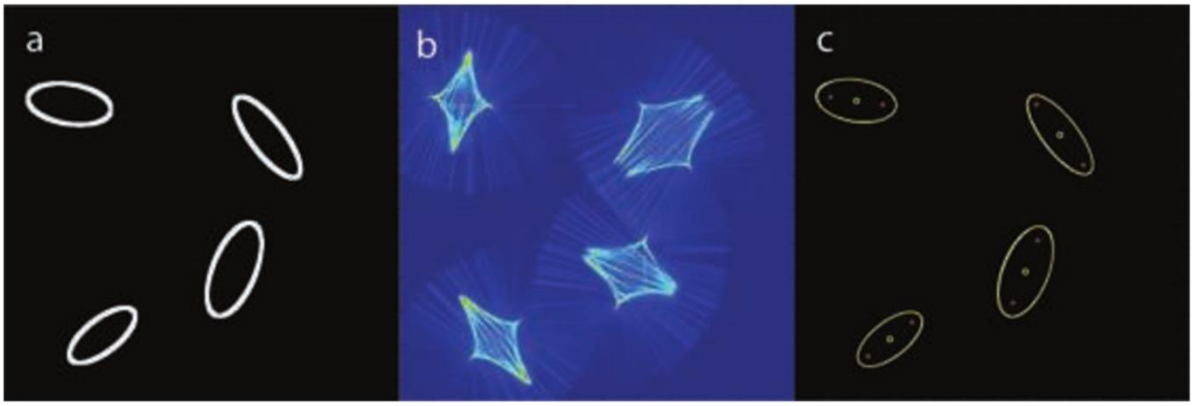

Figure 2: (**a**) Simulated image of 4 ellipses of differing size, shape, orientation and placement. Actual image consists of an ellipse with a boundary width of a single pixel. For display purposes, we have dilated that image with a 3-by-3 rolling ball structuring element.

(**b**) From this image, the two-dimensional accumulation array is constructed. (**c**) The ellipses are detected as described in the text, and displayed on the original image in yellow, with the detected cusps (red crosses) and the corresponding centres (yellow circles) indicated.

based HT method on the original image. The positions and orientations of the two touching ellipsoids are correctly determined, as shown.

To test the performance of our algorithm under more realistic conditions, we detect and characterize the properties of experimental electron micrographs of micron-scale polydisperse ellipsoids, prepared as described in (Champion et al., 2007). Images were obtained using an FEI XL40 Sirion FEG digital scanning electron microscope (SEM; Hillsboro OR, USA). In the case of an almost perfectly ellipsoidal single particle, our evolute-based algorithm accurately determines ellipse position, orientation, shape, and size (Fig. 3). Since the precise shape of the ellipsoid is not known prior to imaging, we verify the accuracy of our characterization method by comparing our results to those obtained using an ellipsoidal fit using a least squared minimization routine. Least squares fitting is performed by eroding the gradient image and removing the isolated and spur pixels (*i.e.* bright pixels that are connected to other bright features by 0 or 1 pixels), as described in detail in (Fitzgibbon et al., 1999). As shown in Figure 3 and Table S2 (Supplemental Materials), the approximation by our method and the least squares fit are practically indistinguishable.

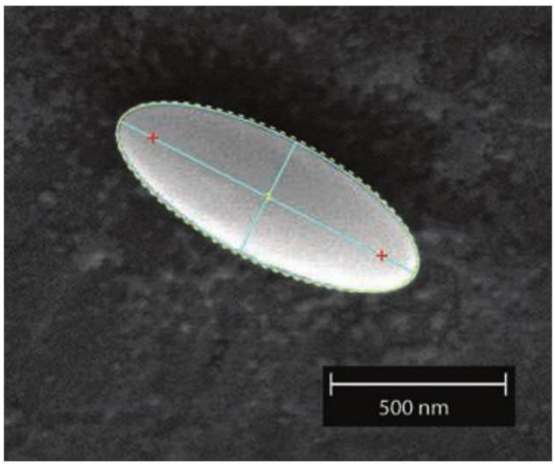

Figure 3: EHT detected (dashed yellow) and least squares (soild cyan) fits to the ellipsoidal particle in an SEM image obtained using a FEI XL40 Sirion FEG digital scanning microscope, at 27500× magnification (Hillsboro OR, USA). The yellow circle is the centre of the detected particle and red crosses are the detected cusp points from the evolute-based HT. The cyan lines locate the ellipse centre determined by the least-squares minimization fitting.

To further test this approach, we analyze an SEM image containing multiple imperfectly ellipsoidal particles on an uneven background. As demonstrated in Figure 4, these particles are also easily detected by our evolute-based HT method. In this example image, nine particles of different sizes and aspect ratios are located within the field of view. For each ellipse, reasonable estimates of particle position, orientation, shape and size are produced, and no false particles are detected. To verify the accuracy of our method, we again compare our results to those obtained with an ellipsoidal fit using a least squares minimization approach. We again find very good agreement between the results obtained with these two methods for (x_c, y_c), b and θ, with errors of less than 1 pixel or 1 degree, respectively (see

Table S3, Supplemental Materials). Since these particles are not perfect ellipses, but are truncated along their major axis to a blunt end, we find larger uncertainties in our determination of *a* than we observed for more perfect ellipses. Through visual inspection, we find that the HT method systematically underestimates the length of the major axis whereas the least squares method overestimates it. Thus, in this case, we independently determine the end-to-end length of the ellipses by a manual measurement of the edge-detected and eroded image, and use this value to determine the error in *a* (Table S3).

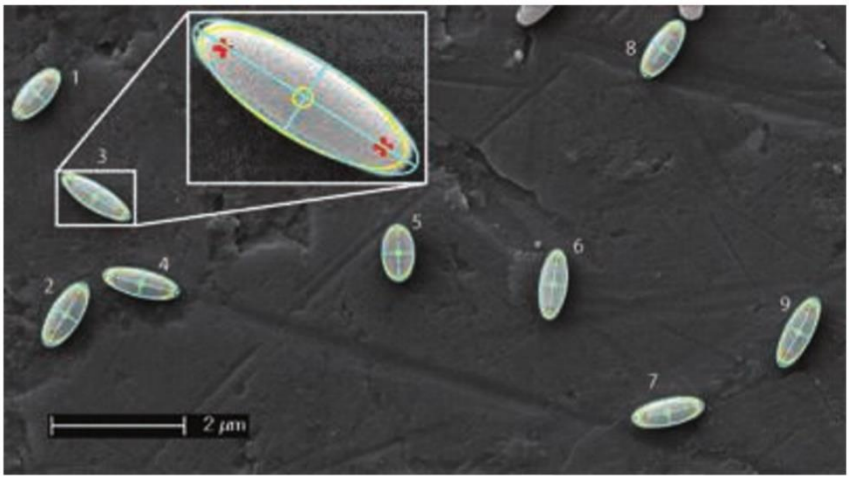

Figure 4: HT detected (yellow) and least squares fits (cyan) to the poly-disperse imperfectly shaped ellipsoids in an SEM image obtained using a FEI XL40 Sirion FEG digital scanning microscope, at 10000× magnification (Hillsboro OR, USA). The red crosses indicate the detected cusp points and yellow circles indicate the centres of the particles detected using the evolute-based HT method. The cyan lines locate the ellipse centres determined by least squares fitting. The white box contains a zoomed view of particle 3.

The overall performance of the evolute-based HT transform method is similar to that of direct fitting of ellipsoids using a least squares minimization approach. Each provides reasonable estimates of ellipse position and features. The detection of these nine particles in the 1303-by-725 pixel image displayed in Figure 4 is completed in less than two seconds by either method using a Windows 7 OS desktop computer with a Pentium Dual Core E5700 3GHz CPU and 3GB RAM. In principle, our method reduces the space complexity of the elliptical HT from $O(N^5)$ to $O(N^2)$. However, in order to achieve execution times of ~ 2 seconds, we have used a vectorized implementation that avoids the use of for loops, which are computationally costly in an interpreted language like MATLAB. This increases the space requirements to $O(N^3)$. If implemented in a compiled language (*i.e.* C++), this issue can be avoided, albeit at the loss of the numerous built-in functions for the easy display and manipulation of images that are available in MATLAB.

There are unique advantages of the evolute-based HT method we present. First, visual inspection of the quality of the evolutes in the accumulation array image provides an immediate and direct readout of our ability to detect ellipsoids with this technique. This allows the effects of various illumination schemes, contrast microscopy methods, etc. to be quickly screened and the best imaging conditions to be determined without full analysis of all data. Additionally, as shown in Figure 5, the evolute-based approach allows for analysis of objects that are physically touching. This is possible since the major cusp positions are always found within the ellipse perimeter, and the parameter space used for feature detection is related to, but distinct from, the real space image. At very high volume fractions, the performance of HT methods tends to degrade, as it does for most particle detection

algorithms, due to interference effects between neighbouring objects during the Hough voting step; however, *a priori* knowledge of ellipse size and shape can substantially limit the search area, improving computational performance and detection accuracy.

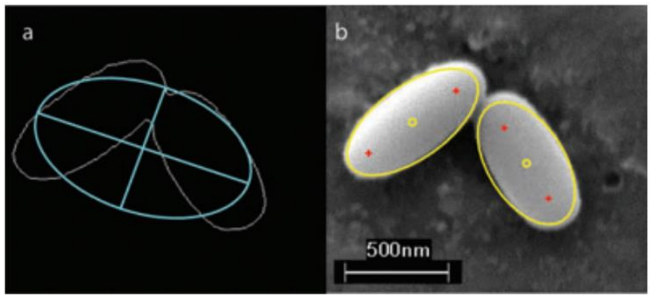

Figure 5: HT detected (yellow) and least squares fits (cyan) to two imperfectly shaped ellipsoids in physical contact, using an SEM image obtained using a FEI XL40 Sirion FEG digital scanning microscope, at 15000× magnification. (**a**) The cyan lines indicate the ellipse centres determined by direct least squares fitting of the edge-detected image (thin white lines on black background). This gives erroneous results since the continuous boundary of the edge-detected object encloses both ellipsoids. (**b**) The red crosses indicate the detected cusp points, and the yellow circles indicate the centers of the particles detected using the evolute-based HT method on the original image. The positions and orientations of the two touching ellipsoids are correctly determined, as shown.

Conclusion

We have presented a new HT method which reduces the complexities of the classical elliptical HT by detecting the cusps on the ellipse evolute that is generated using the gradient information already contained in the image. This method accurately detects and characterizes multiple and polydisperse particles in a reasonable computational time, making

it a useful alternative for a wide range of image processing applications in colloid science, materials science and biomedical engineering.

Acknowledgements

Authors thank Aaron Anselmo and Prof. Samir Mitragotri of UCSB for fabricating the ellipsoidal particles and for assistance in SEM imaging, and Dr. Emre Akbas of UCSB for useful discussions. Authors gratefully acknowledge the support of a Career Award at the Scientific Interface from the Burroughs Wellcome Fund (to M.T.V.). This work made use of MRL Central Facilities supported by the MRSEC Program of the NSF under Award No. DMR-1121053.

Supporting Information

Additional Supporting Information may be found in the online version of this article at the publisher's web site.

Table S1. Parameters of the actual and detected ellipses on the synthetic images shown in Figure 2.

Table S2. HT-detected and least squares (LSQ) fit parameters for the single ellipsoidal particle shown in the electron micrograph in Figure 3.

Table S3. HT detected and least squares (LSQ) fit parameters for the polydisperse, imperfect ellipsoids shown in the electron micrograph in Figure 4.

References

Aguado, A. S., Eugenia Montiel, M. & Nixon, M. S. (1996) On using directional information for parameter space decomposition in ellipse detection. *Pattern Recogn.,* **29,** 369-381.

Bennett, N., Burridge, R. & Salto, N. (1999) A Method to Detect and Characterize Ellipses Using the Hough Transform. *IEEE Trans. Pattern Anal.,* **21,** 652-657.

Champion, J. A., Katare, Y. K. & Mitragotri, S. (2007) Making polymeric micro- and nanoparticles of complex shapes. *P. Natl. Acad. Sci. USA,* **104,** 11901-11904.

Champion, J. A. & Mitragotri, S. (2006) Role of target geometry in phagocytosis. *P. Natl. Acad. Sci. USA,* **103,** 4930-4934.

Crassous, J. J., Dietsch, H., Pfleiderer, P., Malik, V., Diaz, A., Hirshi, L. A., Drechsler, M. & Schurtenberger, P. (2012) Preparation and characterization of ellipsoidal-shaped thermosensitive microgel colloids with tailored aspect ratios. *Soft Matter,* **8,** 3538-3548.

Crocker, J. C. & Grier, D. G. (1996) Methods of Digital Video Microscopy for Colloidal Studies. *J. Colloid Interf. Sci.,* **179,** 298-310.

Ding, T., Song, K., Clays, K. & Tung, C.-H. (2009) Fabrication of 3D Photonic Crystals of Ellipsoids: Convective Self-Assembly in Magnetic Field. *Adv. Mater.,* **21,** 1936-1940.

Duda, R. O. & Hart, P. E. (1972) Use of the Hough transformation to detect lines and curves in pictures. *Commun. ACM,* **15,** 11-15.

Fitzgibbon, A., Pilu, M. & Fisher, R. B. (1999) Direct least square fitting of ellipses. *IEEE Trans. Pattern Anal.,* **21,** 476-480.

Güell, O., Tierno, P. & Sagués, F. (2010) Anisotropic diffusion of a magnetically torqued ellipsoidal microparticle. *Eur. Phys. J.-Spec. Top.,* **187,** 15-20.

Hahn, K., Jung, S., Han, Y. & Hahn, H. (2008) A new algorithm for ellipse detection by curve segments. *Pattern Recogn. Lett.,* **29,** 1836-1841.

Han, Y., Alsayed, A., Nobili, M. & Yodh, A. G. (2009) Quasi-two-dimensional diffusion of single ellipsoids: Aspect ratio and confinement effects. *Phys. Rev. E,* **80,** 011403.

Ho, C. C., Keller, A., Odell, J. A. & Ottewill, R. H. (1993) Preparation of monodisperse ellipsoidal polystyrene particles. *Colloid Polym. Sci.,* **271,** 469-479.

Hough, P. (1962) Method and Means for Recognizing Complex Patterns. United States Patent Office.

Illingworth, J. & Kittler, J. (1987) The Adaptive Hough Transform. *IEEE Trans. Pattern Anal.,* **9,** 690-698.

Irmscher, M., de Jong, Arthur M., Kress, H. & Prins, Menno W. J. (2012) Probing the Cell Membrane by Magnetic Particle Actuation and Euler Angle Tracking. *Biophys. J.,* **102,** 698-708.

Jenkins, M. C. & Egelhaaf, S. U. (2008) Confocal microscopy of colloidal particles: Towards reliable, optimum coordinates. *Adv. Colloid Interfac,* **136,** 65-92.

Kanatani, K.-I. & Ohta, N. (2004) Automatic Detection Of Circular Objects By Ellipse Growing. *Int. J. Image Graph.,* **4,** 35-50.

Kawaguchi, T. & Nagata, R. I. (1998) Ellipse detection using a genetic algorithm. In: *Fourteenth International Conference on Pattern Recognition.* Brisbane, Qld.

Keville, K. M., Franses, E. I. & Caruthers, J. M. (1991) Preparation and characterization of monodisperse polymer microspheroids. *J. Colloid Interf. Sci.,* **144,** 103-126.

Luo, D., Smart, P. & Macleod, J. E. S. (1995) Circular hough transform for roundness measurement of objects. *Pattern Recogn.,* **28,** 1745-1749.

Madivala, B., Fransaer, J. & Vermant, J. (2009) Self-Assembly and Rheology of Ellipsoidal Particles at Interfaces. *Langmuir,* **25,** 2718-2728.

Melle, S., Calderan, O. G., Rubio, M. A. & Fuller, G. G. (2002) Rotational dynamics in dipolar colloidal suspensions: video microscopy experiments and simulations results. *J. Non-Newton. Fluid.,* **102,** 135-148.

Muammar, H. & Nixon, M. (1989) Approaches to extending the Hough transform. In: In *Proceedings of the International Conference on Acoustics, Speech, and Signal Processing,* ICASSP-89. vol. 3, pp. 1556–1559.

Neycenssac, F. (1993) Contrast Enhancement Using the Laplacian-of-a-Gaussian Filter. *CVGIP: Graph. Model Im.,* **55,** 447-463.

Pao, D., Li, H. F. & Jayakumar, R. (1993) A decomposable parameter space for the detection of ellipses. *Pattern Recogn. Lett.,* **14,** 951-958.

Peng, T., Balijepalli, A., Gupta, S. K. & LeBrun, T. (2007) Algorithms for On-Line Monitoring of Micro Spheres in an Optical Tweezers-Based Assembly Cell. *J. Comput. Inf. Sci. Eng.,* **7,** 330-338.

Sacanna, S., Rossi, L., Kuipers, B. W. M. & Philipse, A. P. (2006) Fluorescent Monodisperse Silica Ellipsoids for Optical Rotational Diffusion Studies. *Langmuir,* **22,** 1822-1827.

Tsuji, S. & Matsumoto, F. (1978) Detection of Ellipses by a Modified Hough Transformation. *IEEE Trans. Comput.,* **C-27,** 777-781.

Velikov, K. P., van Dillen, T., Polman, A. & van Blaaderen, A. (2002) Photonic crystals of shape-anisotropic colloidal particles. *Appl. Phys. Lett.,* **81,** 838-840.

Xie, Y. & Ji, Q. (2002) A new efficient ellipse detection method. In: *Proceedings of the 16th International Conference on Pattern Recognition.*

Yoo, J. H. & Sethi, I. K. (1993) An ellipse detection method from the polar and pole definition of conics. *Pattern Recogn.,* **26,** 307-315.

Yu, X., Leong, H. W., Xu, C. & Tian, Q. (2004) A robust and accumulator-free ellipse Hough transform. In: *Proceedings of the 12th annual ACM international conference on Multimedia.* ACM, New York, NY, USA.

Zheng, Z. & Han, Y. (2010) Self-diffusion in two-dimensional hard ellipsoid suspensions. *J. Chem. Phys.,* **133,** 124509-124510.